Imperial College of Science, Technology and Medicine
Department of Aeronautics

# CONCEPTUAL MULTIDISCIPLINARY AIRCRAFT DESIGN USING AERO-STRUCTURAL ADJOINT-BASED METHODS

ANDREA VITI

A thesis submitted for the degree of
Doctor of Philosophy
March 2019

## Declaration of Originality

The content of this document is the result of my own work, except where appropriately referenced.

ANDREA VITI

## Copyright Declaration

## Abstract

Nowadays, on the one hand aircraft design reached very high-fidelity level and aircraft manufacturers obtained such experience that they deeply rely on their design work-flow, models and tests. On the other hand, aircraft architecture struggles to change. Indeed, because of uncertainty and risk management reasons engineers are worried to explore new designs. Moreover, preliminary design models do not enable unconventional aircraft design. By combining the current Overall Aircraft Design models with aero-structural analysis and optimization information, this research work introduces an innovative multidisciplinary approach to be implemented in the preliminary aircraft design phase for novel configurations. The procedure was successfully tested with a forward swept wing-body architecture for which classical preliminary design method was not able to catch physical behaviours due to the wing bending-torsion coupling.

**Keywords**: Multidisciplinary Design, Overall Aircraft Design, Aero-Structural Optimization, Adjoint-method, Preliminary Aircraft Design.

## Acronyms

| | |
|---|---|
| BSW | Backward Swept Wing |
| CAD | Computer Aided Design |
| CFD | Computation Fluid Dynamics |
| CSM | Computational Solid Mechanics |
| DOC | Direct Operative Cost |
| FFD | Far-Field Drag |
| FSW | Forward Swept Wing |
| FVM | Finite Volume Method |
| KS | Kreisselmeier-Steinhauser funciton |
| MDO | Multidisciplinary Design Optimization |
| MTOW | Maximum Take-Off Weight |
| NSW | No-Swept Wing |
| OAD | Overall Aircraft Design |
| OWE | Operator Weight Empty |
| RANS | Reynolds Average Navier-Stokes |
| SeAnDef | Sequential Analytic Deformation |
| SLST | Sea Level Static Trust |
| TLARs | Top Level Aircraft Requirements |
| TLV | Top Level Variable |

## Notation

| | |
|---|---|
| $\alpha$ | Angle of attack |
| $AR$ | Wing aspect ratio |
| $b/2$ | Semi-span of the wing |
| $C_{D_{ff}}$ | Coefficient of drag |
| $C_{dff\_ind}$ | Coefficient of induced drag |
| $C_{dff\_wave}$ | Coefficient of wave drag |
| $C_L$ | Coefficient of lift |
| $C_r$ | Wing root chord |
| $C_t$ | Wing tip chord |
| $d$ | Wing root position |
| $D$ | Far-field drag |
| $D_i$ | Induced drag, Displacement of the $i^{th}$ node of the wing structure |
| $D_f$ | Friction drag |
| $D_p$ | Pressure drag |
| $D_{sp}$ | Spurious drag |
| $D_v$ | Viscous drag |
| $D_w$ | Wave drag |
| $E$ | Volumetric energy |
| $\varphi_{1/4}$ | Sweep angle of the wing at ¼ of the chord |
| $f(\vec{x})$ | Objective function |
| $\vec{F}$ | Flux vector |

| | |
|---|---|
| $F_{ij}$ | Coefficient that transform *j-forces* into *i-displacement* |
| $F_x, F_y, F_z$ | Forces acting on the wing structure |
| $g_i(\vec{x})$ | Inequality constraint |
| $H$ | Total enthalpy |
| $h_k(\vec{x})$ | Equality constraint |
| $J(\vec{x})$ | Objective function |
| $\lambda$ | Wing taper ratio |
| $L$ | Fuselage length |
| $L_j$ | Load at the $j^{th}$ node of the wing structure |
| $M$ | Mach number |
| $M_x, M_y, M_z$ | Moments acting on the wing structure |
| $M_0, \dots, M_{15}$ | Industrial design milestones |
| $\vec{n}$ | Normal vector to the surface |
| $\Omega_{i,j}$ | Control volume associate to the mesh point |
| $\omega_x, \omega_y, \omega_z$ | Linear field wing deflection |
| $p_\infty$ | Free stream static pressure |
| $P_i$ | $i^{th}$ node of the wing structure |
| $P_{i,j}$ | Mesh point |
| $\rho$ | Density |
| $R_{i,j}$ | Residual, balance of fluxes over all the faces of the control volume |
| $\sigma$ | Normal stress |
| $s$ | Entropy |

| | |
|---|---|
| $S$ | Wing surface |
| $S_\infty$ | Lateral and upstream boundary |
| $S_O$ | Closed outer boundary of the flow control volume |
| $S_A$ | Closed aircraft surface |
| $S_D$ | Downstream boundary of the control volume |
| $S_{i,j}$ | Surface of the control volume associate to the mesh point |
| $\theta_x, \theta_y, \theta_z$ | Angular field wing deflection |
| $\tau$ | Shear stress in fluid |
| $t$ | Time |
| $T$ | Temperature |
| $u$ | Velocity along the *x*-axis |
| $u_\infty$ | Free stream velocity along *x*-axis |
| $U$ | Conservative variables |
| $v$ | Velocity along the *y*-axis |
| $w$ | Velocity along the *z*-axis |
| $\vec{x}$ | Design variable vector |
| $x_a$ | Aerodynamic design variable |
| $x_s$ | Structural design variable |
| $\chi_j$ | Position of the aerodynamic mesh $j^{th}$ node of deformed wing |
| $\chi_{rig_j}$ | Position of the aerodynamic mesh $j^{th}$ node of undeformed wing |

# Contents

## List of Tables

## List of Figures

# Chapter 1

# Introduction

*This chapter aims at introducing the subject of the study. The undertaken research originates from the need of aircraft manufacturers to design new aircraft architectures for which no historical data and semi-empirical models were available. The inability of current preliminary design tool to reliably study unconventional configurations is the motivation of this work. During the first design phases the top level requirements are met and the configuration defined and it will be optimise in details during the forthcoming expensive detail design phase. Erroneous choices taken during the preliminary phases and discovered later in the process may become too expensive to solve, potentially impacting on the success of the entire aircraft design.*

## Contents

## Introduction

From the beginning of the 20th century, an extraordinary improvement in aviation is reported in terms of aircraft architecture, physical understanding and safety. Indeed, in the last century several configurations both for military and civil applications have been studied and often the final outcome of these investigations was a unique trade-off between knowledge, manufacturing constraints and reliability of simulation results. The civil aircraft configuration that is still currently adopted by the aircraft manufacturers follows the same principle, and engineers optimize this architecture progressively without introducing major modification. The reason is that modifications introduce uncertainties, which could cost in turn a lot of money; overall it is better to keep adopting old ineffective but well-known techniques. Moreover, large datasets have been created by the adopted technology and semi-empirical models have been developed to better customise the aircraft architecture for specific needs and use. The design phases affected the most by those experience-based models are the conceptual and preliminary design phase. Figure 1.1 summarizes the traditional industrial milestones to complete the aircraft design and manufacturing process, ranging from $M_0$ (conceptual idea of the project) to $M_{15}$ (final stage of the program).


**Figure 1.1: Aircraft design milestones**

Depending on the nature of the project, the experience and the creativity of engineers, the first phase ($M_0$ to $M_5$) converges to a design that represents the input of the second detailed phase. The more advanced is the aircraft program, the more "constrained" the innovation is. Figure 1.2 compares the actual and the target ease of the design evolution and the system knowledge during the aircraft development process. The *conceptual* and *preliminary* design phases are characterized by a high degree of freedom the architecture not being completely defined yet. It is clear that the detailed phase is subjected to preliminary decisions, whereas the first phase has a strong impact on the whole project. Incorrect conceptual and preliminary choices may lead to unfeasible or unprofitable design. This explains the need to have a fast and reliable conceptual and preliminary design processes: fast because a lot of different configurations which satisfy the same requirements

have to be studied, reliable because preliminary results will make the project either successful or not.

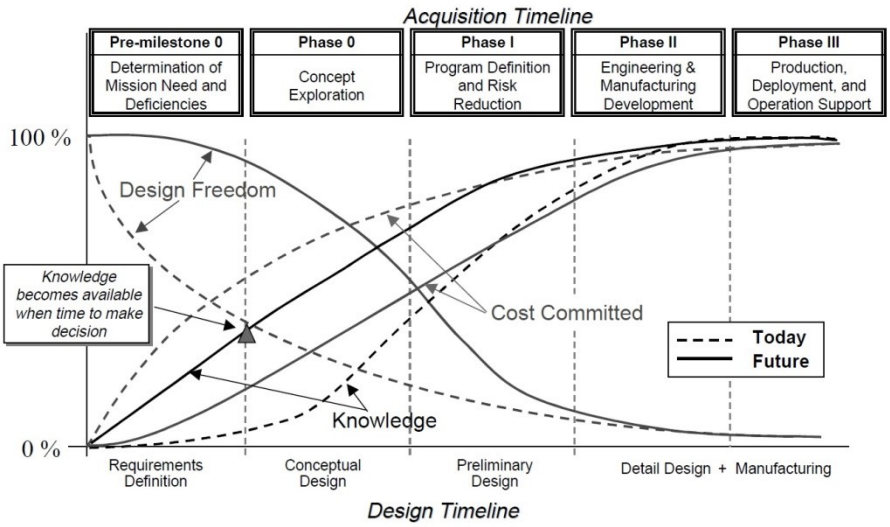


**Figure 1.2: Aircraft design process *(Marvis et al., 2000)***

## 1.1 Context and Challenge

The scope of this Ph.D. research is to develop an innovative and reliable preliminary design process for unconventional aircraft architecture, in order to overtake the aforementioned problem of innovation in the field of civil aviation. The process is based on the concept of Multidisciplinary Design and Optimization, the so-called MDO, and relies on the fact that several disciplines have to be simultaneously taken into consideration to have a meaningful design. To highlight the importance of the multidisciplinary design, *J. R. R. A. Martins* (*2002*) showed the resulting the lift distribution on a wing if it is optimized either for reducing the wing drag or a weighted function that includes wing drag and wing structural weight (Figure 1.3). The blue distribution represents the elliptic distribution, i.e. the lift distribution corresponding to minimum drag. The red line represents a less efficient lift distribution from an aerodynamic point of view. Nevertheless, in terms of overall efficiency, the red condition results to be better than the blue one, since a small increment of wing drag is associated with a significant reduction of the structural weight.

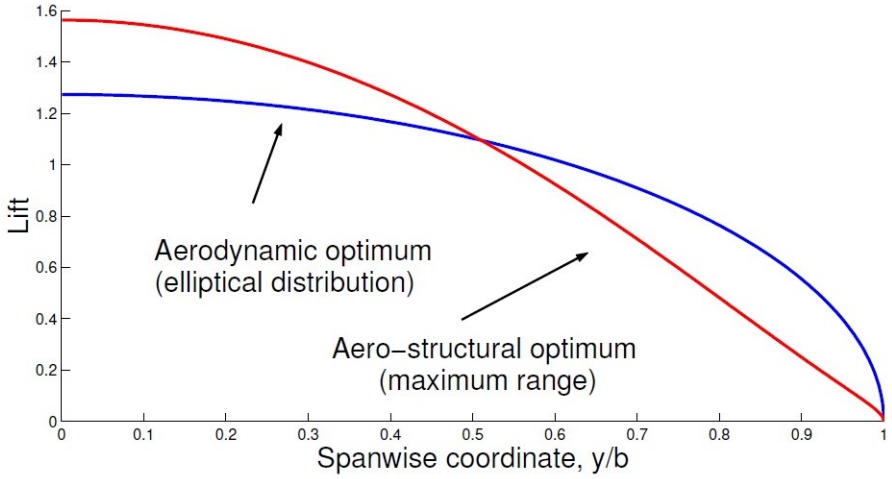


**Figure 1.3: Elliptic vs aero-structural optimum lift distribution *(J. R. R. A. Martins, 2002)***

The reason is that important disciplines involved in aircraft design such as aerodynamics, structural mechanics and flight mechanics are strongly coupled each other. Thus, for a global optimal configuration it is impossible to optimize independently one of them without considering this correlation. To better understand the importance of multidisciplinary design, a consideration on wing span is elaborated. From a purely aerodynamic point of view, the increase of span decreases the induced drag. However, in most of transport aircraft, the span modifications are mainly constrained by aero-structural (flutter, structural weight, etc) and fuel volume considerations. A good introduction to assess how the wing design parameters impact the aero-structural trade-off is presented by *I.* Ghazlane (*2012*). There, the author underlines how often a modification of whatsoever wing design parameters which has a positive/negative impact for one of the two disciplines has consequently the opposite impact (negative/positive) for the other discipline. It is then clear the importance of multidisciplinary design since the first design phases of an aircraft.

As stated above, conceptual and preliminary design are the phases where fast evaluations are required. Usually, data based empirical models are used to have a first evaluation of the whole aircraft characteristics. The closer the studied architecture to the cases from which the data base were created is, the more reliable the results of this first design phase are. Then, sophisticate physical models are usually not used until the detail design phase starts. Problems occur whenever unconventional architecture or physical behaviour are considered. In those cases, the models based on historical data lose effectiveness. For instance, if two aircrafts are considered and the

only difference is the sign of the sweep angle of the wing (same module though, a classical configuration with positive sweep and an unconventional one with a negative sweep) the results of a preliminary aerodynamic evaluation based on theoretical or data-based models will be identical since the flow behaviour changes with the cosine of the swept angle (then not effected by the sign of the angle). Theoretical and data-based conceptual and preliminary design models usually do not consider unconventional aerodynamic and aero-elastic behaviours. As consequence of that, a classical aircraft architecture can be designed with a certain reliability since the early design stages, which is not the case for the unconventional one. This is only one of several typical problems aircraft manufactures face during the assessment of a very new design. A possible solution involves the use of light physical evaluations capable to enrich the data-based Overall Aircraft Design (OAD) models with case-sensitive results. This last is the main goal of the investigation hereby discussed.

## 1.2 The proposed approach

The approach developed here aims to fulfil aircraft manufacturer's need to explore new unconventional designs and architectures. In particular, the whole analysis is based on Airbus preliminary design procedure which use an in-house semi-empirical models built on historical data bases and theoretical models. Starting from the definition of the top level requirements, such as payload, maximum range, etc… the tool is able to preliminarily estimate the whole aircraft characteristics like aerodynamic load, structural weight, flight domain and performances, engine, etc. Aerodynamics and structure were identified as the dominant factors for the aircraft design, then higher-fidelity approaches were adopted for these two disciplines, in order to provides more reliable results to be used by the preliminary design tool. In particular, for the aerodynamics the Euler formulation was chosen, while the Euler-Bernoulli formulation for the structural analysis. The Airbus overall aircraft design took care about the other preliminary design aspects while using enriched aero-structural information. This new approach was tested on a forward-swept wing aircraft and ultimately compared to a classical backward-swept configuration.

## 1.3 Organization of the thesis

The work was carried out aiming at performing the most reliable analyses in the lightest and fastest way possible. Analogously, the thesis is organized in such a way that all steps to reach the final multidisciplinary design optimization for the preliminary overall aircraft design are identified and described.

Chapter 2 identifies the procedures and the characteristics of the aerodynamic and structural analyses necessary to find the best trade-off between simplicity and reliability. The chapter is organized in three sections: *Aerodynamic analysis*, *Structural analysis* and *Aero-elastic coupling*. First, in the Aerodynamic analysis section, after the description of the chosen flow equations the attention is placed upon the far-field drag extraction method. This method relies on the possibility to identify the physical component of the total drag which includes also the numerical drag. Second, the geometrical and mesh features needed to have qualitative meaningful simulations were discussed. Finally, the presented results of aerodynamic investigations highlight the need to take the fuselage into account for a reliable aerodynamic wing design. In the Structural analysis section an introduction and validation of the light structural model used to perform the forthcoming aero-elastic coupling are presented. In addition, an investigation on the coupling parameters to have a reliable simulation is presented and the need to take structural deformation into account while performing the aerodynamic design of the wing is described.

Chapter 3 investigates the aerodynamic and structural optimization. First, the optimization techniques are introduced, followed by the monodisciplinary optimizations. Concerning the aerodynamic optimization, an investigation on the design parameters is carried out, focussing on the importance of performing aero-elastic optimization to obtain reliable results. Similarly, an investigation on the structural design variable is undertaken, and a consistent structural optimization procedure is developed in order to have structural sizing in line with the aerodynamic load.

Chapter 4 is devoted to show the new process of multidisciplinary design optimization for conceptual and preliminary design, as well as its application onto a conventional and an unconventional architecture. Initially, the aircraft manufacturer state of the art and the new design

procedure built around it are described. Second, a deep analysis on the way the empirical aircraft design models are enriched with physical information is provided and, in the end, the comparison between the results of the considered test cases is presented Here the author emphasises the importance of Multidisciplinary Design Optimization to support the overall aircraft design evaluations and to make possible reliable preliminary design for unconventional aircraft architecture.

Chapter 5 summarizes what has been described along the manuscript and underline the important results coming from the new proposed multidisciplinary design approach applied on an unconventional aircraft.

# Chapter 2

# Multidisciplinary Analysis

*This chapter introduces the disciplines used to perform the preliminary design of the aircraft configuration. The methods of analysis for both aerodynamic and structural investigations are presented, giving particular focus on the chosen model (fluid and structure models), pre and post-processing approach and on the importance of the aero-structural coupling since the early stages of an aircraft design.*

## Contents

## Introduction

The chapter is organized in three main parts. The first one (Sec. 2.1) is dedicated to the aerodynamic investigation. Here, the mesh definition is presented and the description of the mesh topologies of the isolated wing and the wing-body configuration underlining the mesh features which fit quality and time-cost compromises is given. The CFD problem definition is addressed and the work flow is introduced. The second part concerns the wing structure definition (Sec. 2.2). The beam model is shown and the validation of the software is presented. Subsequently, the fluid-structure interaction analysis is addressed and three main aspects are underlined (Sec 2.3): the parameters that play a role in the analysis convergence, the phenomena of the static divergence for FSW and the importance of considering more complex geometry rather than the isolated wing only.

## 2.1 Aerodynamic analysis

The ONERA in-house code called ***elsA*** (*A. Dumont et al., 2011; L. Cambier and JP. Veuillot, 2008; L. Cambier and M. Gazaix, 2002*) was used for fluid simulations. In order to be compatible with the fast simulation time required by preliminary design the Euler equations were solved to describe the aerodynamic flow around the aircraft. The inviscid approach captures the non-linear aerodynamic effects occurring in transonic flows, which are essential in the aerodynamic design of a transport aircraft. Although direct viscous forces are neglected in this analysis, such model appears as a significant improvement over much simpler models used traditionally at preliminary design stage (for example semi-empirical, lifting line, etc.). Particular attention was paid to the mesh generation due to the intrinsic non-dissipative nature of the fluid, which requires a well converged solution to be obtained, for the calculation of accurate sensitivity for optimization purposes. In order to check the mesh quality and to extract simulation results, an in-house post-processing tool called ***FFD72*** (G. Carrier et al., 2014; D. Hue, S. Esquieu, 2011; D. Hue, 2014; H. Toubin, D. Bailly, 2015; A. Viti et al., 2016) was used. It is able to perform an accurate extraction and decomposition of the drag components by far-field and near-field comparison. It therefore provides an evaluation of the numerical error (spurious drag) due to the mesh quality (*M. Ueno et al., 2011; Destarac D., 1993; L.* Paparone, R. Tognaccini, 2002).

As described above, the inviscid compressible formulation is used to describe the aerodynamic field. Although the viscous effects are not considered, previous studies show the efficacy of this model to predict induced and wave drag. For the latter, a small overestimation could be observed while the position of the shock is usually well predicted. The limits of the formulation will be described below. For drag estimation and mesh quality characterization, the far-field/near-field comparison theory is used. This post-processing approach has been shown to result in a reliable drag prediction even if very coarse mesh is used (*S. Esquieu, 2007; W. Yamazaki et al., 2006; R. Tognaccini, 2005*).

### 2.1.1 Flow description – Euler formulation

The most general continuum flow description for a inviscid, adiabatic fluid is described by the set of Euler equations, can be obtained from the Navier-Stokes equations by neglecting all shear stresses and heat conduction term. As is known from Prandtl's boundary layer analysis, this is a valid approximation for flows at high Reynolds numbers, outside the viscous region developing near solid surfaces and outside the wakes (*L. Prandtl, 1928; L. Prandtl, O.G. Tietjens, 1934; I. Tani, 1977;* D. *Christodoulou, S. Miao, 2014; H.W. Liepmann, A. Roshko, 1957; G. Buresti, 2012; J.D. Anderson, 2011; I.H. Abbott, A.E. Von Doenhoff, 1959*).

As *C. Hirsch* (*2007*) pointed out, considering flow conditions with uniform inflow, that is an irrotational flow far upstream, it is well known from inviscid flow and Helmholtz theorem that the flow will remain irrotational everywhere. In other words, it is equivalent to a potential flow. The first difference between potential and Euler equations lies in their mathematical properties, while another important difference concerns the potential generation of numerical entropy by the Euler model, as a consequence of the numerical dissipation of the selected discretization scheme (*C. Hirsch*, 2007; J.D. Anderson, 1995). The effect of this artificial dissipation on the flow behavior can overshadow the effects of the molecular or turbulent viscosity. Therefore, an accurate identification of the regions where an increase of entropy is observed, beside a quantification of the numerical dissipation is essential in order to establish the reliability of the numerical results. This concept will be more exhaustively addressed in the Sec. 2.1.2, where the far-field drag decomposition theory is presented.

The time-dependent Euler equations, in conservation form and in an absolute frame of reference, for the conservative variables *U* is defined as follows:

$$\frac{\partial U}{\partial t} + \vec{\nabla} \cdot \vec{F} = 0 \tag{2.1}$$

where the flux vector *F* has the Cartesian component (*f*,*g*) given by:

$$f = \begin{vmatrix} \rho u \\ \rho u^2 + p \\ \rho uv \\ \rho uH \end{vmatrix};\ g = \begin{vmatrix} \rho v \\ \rho vu \\ \rho v^2 + p \\ \rho vH \end{vmatrix};\ U = \begin{vmatrix} \rho \\ \rho u \\ \rho v \\ \rho E \end{vmatrix} \tag{2.2}$$

with *H* as total enthalpy. It is important to recognise the properties of the entropy variation in an inviscid flow. In absence of heat source, the entropy equation for continuous flow variations reduces to:

$$T\left(\frac{\partial s}{\partial t} + \vec{v} \cdot \vec{\nabla} s\right) = 0 \tag{2.3}$$

expressing that entropy is constant along the flow path. Hence, Euler equations describe isentropic flow, in the absence of discontinuities. As is known, this set of equations permits discontinuous solutions in certain cases, namely, vortex sheets, contact discontinuities or shock waves occurring in transonic and supersonic flows (*C. Hirsch*, 2007; J.D. Anderson, 2011).

Euler equations are only valid outside the viscous boundary layer and are not able to describe flow separation. Due to that, important practical limitations may come out:

- the flight conditions of the airplane have to be appropriate to the range of validity of the fluid model (no global or local high angle of attack). As will be show in Sec. 2.3, static aero-elastic deformation can result in high local angles of attack if a forward-swept wing is considered, making convergence of aero-elastic simulations a considerable numerical challenge;
- high surface curvatures can impede the numerical calculation from reaching adequate convergence level. This third aspect will be addressed in Sec. 2.1.3, where the geometrical features of the wing tip, as well as the topology of the mesh are introduced.

#### 2.1.1.1 Finite Volume Method (FVM) for Euler equations

The ONERA *elsA* CFD software (*A. Dumont et al., 2011; L. Cambier and JP. Veuillot, 2008; L. Cambier and M. Gazaix, 2002*) applies the Finite Volume Method (*C. Hirsch, 2007; H. Versteeg, W. Malalasekera, 2007*) to obtain an approximate numerical solution of Eq. 2.1. In this section is presented the formulation for the used compressible inviscid equation.

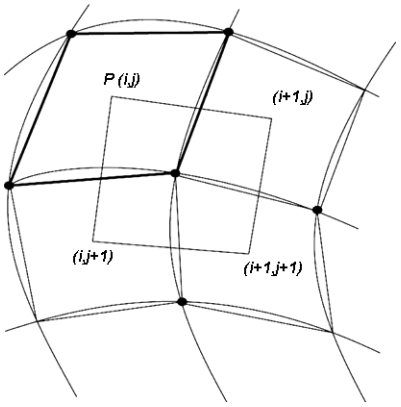


**Figure 2.1: Cell-centered finite volume space discretization on a structured mesh**

The integral conservation law is applied to each control volume $\Omega_{i,j}$, associated to the mesh point *P (i,j)* (Figure 2.1), defining hereby the discretized equation for the unknowns $U_{i,j}$ attached to that same vertex or cell:

$$\frac{\partial}{\partial t}\int_{\Omega_{i,j}} U \, d\Omega + \oint_{S_{i,j}} \vec{F} \cdot d\vec{S} = 0 \tag{2.4}$$

The previous equation is replaced by its discrete form, where the volume integrals are expressed as averaged values over the cell and where the surface integral is replaced by a sum over all bounding faces of the considered volume $\Omega_{i,j}$:

$$\frac{d}{dt}\left[\overline{U}_{i,j}\Omega_{i,j}\right] = -\sum_{faces} \vec{F}^{*} \cdot \Delta\vec{S} \equiv -R_{i,j} \tag{2.5}$$

The right-hand side defines the residual $R_{i,j}$ as the balance of fluxes over all the faces forming the cell (*i,j*). Some of the essential properties of the FVM are:

- the solution $\overline{U}_{i,j}$ of the system is the cell-averaged value of the conservative variable *U* over the cell (*i,j*);

- when the results of the simulation are post-processed, the cell-averaged values is assigned to the center of the cell. This introduces an error which is part of the discretization error;
- the numerical flux $\vec{F}^*$ represent the discretization of the physical fluxes.

For spatial discretization, appropriate schemes are selected to ensure consistency with the development of the discrete adjoint solver that will be presented after. In particular, convective flux is discretize using Roe's flux difference formula (*P.L. Roe, 1981*) and the MUSCL approach with Van Albada limiter (*G.D. Van Albada, B. Van Leer, W. Roberts, 1982*). For temporal discretization, the convergence to steady state is performed using an implicit time integration algorithm based on a Backward-Euler scheme with locally varying time step.

### 2.1.2 Far Field Drag extraction

Drag is the component of the force exerted by a fluid on a solid body, the two being in conditions of relative movement, which acts against the flight direction. It results from stresses exerted by the fluid on the surface of the body, in the normal direction to this surface (pressure) and in the tangential plane (shear stress) if the fluid is viscous. The most straightforward method to extract drag from a numerical solution of the fluid dynamic equations, solved under appropriate boundary conditions, is to resolve the components of static pressure and viscous stresses against the flight direction, and integrate these over the body surface. In this way, drag can be broken down into (static) pressure drag and friction drag, the so-called *mechanical breakdown*. This method requires only data computed on the body surface, and is known as the ***near-field approach*** to drag computation. Another approach consists in deriving an expression for drag, not from the effects of the fluid on the body, but conversely from the effects of the body on the fluid, by using the conservation laws of fluid motion expressed by the flow equations. This approach involves control volumes (and then bounding surfaces) which extend within the flow-field and not only at the fluid/solid interface. This is known as the ***far-field approach***, which, contrary to the near-field approach, can lead to a *physical breakdown* of the drag upon making some adequate assumptions (*J.L. Steger, B.S. Baldwin, 1972*; *D. Destarac, 2008; M. Gariépy et al., 2010*). Since the model is based on the conservation laws of fluid motion, the convergence of the residuals, then a good resolution of the flow equations in the domain, is required otherwise bad calculation of the far-field

drag terms may occurs. *J.W. Slooff* (*1985, 1989*) gave an important overview of the problem and he emphasized the far-field approach to drag extraction as a promising alternative to the classical and straightforward surface stress integration.

Several overall and partial drag decompositions could be defined (for a complete overview of the physics of the drag, *D. Destarac, 2008*):

A. Total drag = pressure drag + friction drag
B. Total drag = wave drag + viscous drag + induced drag
C. Total drag = wave drag + viscous pressure drag + friction drag + induced drag
D. Total drag = profile drag + induced drag
E. Total drag = friction drag + form drag + induced drag
F. Pressure drag = wave drag + viscous pressure drag + induced drag
G. Pressure drag = form drag + induced drag
H. Profile drag = viscous drag + wave drag
I. Profile drag = friction drag + form drag
J. Form drag = wave drag + viscous pressure drag
K. Viscous drag = viscous pressure drag + friction drag

Only breakdown (A) is possible in the near-field approach. Each breakdown from (B) to (K) requires the far-field approach. In aerodynamic performance assessment or shape design, more significant and detailed information can be found in a physical breakdown than in the mechanical breakdown approach. Hence the increasing importance of far-field drag extraction in aerodynamic assessment and design (*L. Paparone, R. Tognaccini, 2003; H. Toubin, D. Bailly, 2015; M. Méheut, D. Bailly, 2008; C. Masson et al., 1998; T. Sibilli, M. Savill, 2011*). C.P. Van Dam (*1999*) proposes a review of experiences in CFD-based drag prediction with an emphasis on flow solution described by the Euler and Reynolds-averaged Navier-Stokes equations.

#### 2.1.2.1 Theoretical formulation of the Far-field / Near-field balance

Detailed description of the theoretical aspects of the far-field approach is given by *J. Van der Vooren and J.W. Slooff* (*1990*). *D. Destarac and J. Van der Vooren* (*2004*) presented the far-field /

near-field drag balance in a new form. A method for the computation and breakdown of the aerodynamic drag into viscous and wave components, applicable to aircraft configuration with operating engines, is also proposed by *L. Paparone* and *R. Tognaccini* (2002) and by *R. Tognaccini* (*2003, 2005*). A simple summary of the approach is also proposed in (*D. Destarac, 2003*).

The mathematical formulation described in *D. Destarac* (*2008*) is reported below. Let's consider the formulation for steady flow described by RANS equation with subsonic freestream state before. The particular case of inviscid compressible equation is easily derivable. The combination of the conservation of the mass and of the *x*-momentum (*x* = freestream flow direction) gives:

$$div[\rho(u-u_\infty)\vec{q}+(p-p_\infty)\vec{\imath}-\overrightarrow{\tau_x}]=0 \tag{2.6}$$

where $\vec{q}$ is the velocity vector, $\rho$ is the fluid density, $u$ is the velocity component along the x-axis, $p$ is the pressure, $\vec{\imath}$ is the x-axis direction and $\overrightarrow{\tau_x}$ is the x-axis component of the stress tensor. By defining the vector $\vec{f}$ as:

$$\vec{f}=-\rho(u-u_\infty)\vec{q}-(p-p_\infty)\vec{\imath}+\overrightarrow{\tau_x} \tag{2.7}$$

in the flow control volume *V*, $\vec{f}$ has the following property:

$$div\vec{f}=0 \rightarrow \iiint_V div\vec{f}dV=0 \rightarrow \iint_{S_A+S_O}(\vec{f}\cdot\vec{n})dS=0 \rightarrow \iint_{S_O}(\vec{f}\cdot\vec{n})dS=-\iint_{S_A}(\vec{f}\cdot\vec{n})dS \tag{2.8}$$

where $S_A$ represents the closed aircraft surface and $S_O$ the closed outer boundary of the flow control volume, with the unit normal vector oriented as indicated in Figure 2.2. Making use of the fact that the first term in $(\vec{f}\cdot\vec{n})$ is equal to zero on the aircraft surface because for viscid flow the velocity is null at the wall (adherence condition), it is possible to express the sum pressure drag plus friction drag as the integral of $-(\vec{f}\cdot\vec{n})$ over $S_A$:

$$D=D_p+D_f=\iint_{S_A}[(p-p_\infty)n_x-(\overrightarrow{\tau_x}\cdot\vec{n})]dS=-\iint_{S_A}(\vec{f}\cdot\vec{n})dS \tag{2.9}$$

Here, pressure drag plus friction drag will be called *near-field drag*. Thus, a straightforward expression for the *far-field drag* is:

$$D = \iint_{S_O} (\vec{f} \cdot \vec{n}) dS = \iint_{S_D} (\vec{f} \cdot \vec{n}) dS \left( = - \iint_{S_A} (\vec{f} \cdot \vec{n}) dS = D_p + D_f \right) \tag{2.10}$$

where $S_D$ is the downstream boundary of the control volume. This result comes from the fact that, extending the control volume to infinity and breaking $S_O$ down into $S_\infty$ (lateral and upstream boundary) and $S_D$, it is easy to find that $\vec{f} = \vec{0}$ in $S_\infty$ since the flow may be considered inviscid ($\overrightarrow{\tau_x} = \vec{0}$) and non-perturbed ($u = u_\infty$, $p = p_\infty$). It is important to notice that this theory cannot be valid for supersonic flows since the latter condition will be not fulfilled.

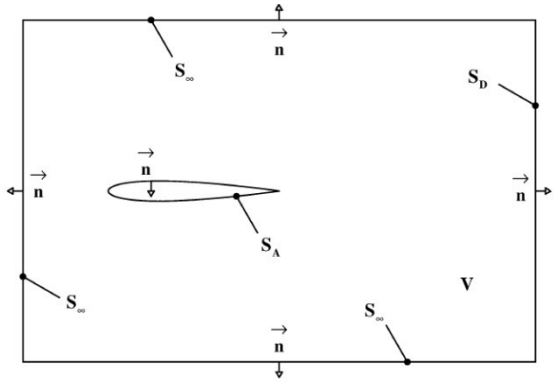


**Figure 2.2: Basic boundaries and control volumes (*D. Destarac, 2008)***

In the absence of trailing vortices (induced drag), there are only viscous drag $D_v$ and wave drag $D_w$ present. If the downstream surface $S_D$ is located in the inviscid part of the flow and enough downstream, then it is possible to assume that $\overrightarrow{\tau_x} = \vec{0}$, $v = w = 0$ and $p = p_\infty$. Moreover, introducing the thermodynamic variables of entropy *s* and enthalpy *H*, it is possible to write the following expression:

$$D = D_p + D_f = D_v + D_w = - \iint_{S_D} \rho(u - u_\infty)(\vec{q} \cdot \vec{n}) dS = - \iint_{S_D} \rho \Delta\bar{u} (\vec{q} \cdot \vec{n}) dS \tag{2.11}$$

where

$$\Delta\bar{u} = u_\infty \sqrt{1 + 2\frac{\Delta H}{u_\infty^2} - \frac{2}{(\gamma - 1) M_\infty^2} \left[ \left( e^{\frac{\Delta s}{R}} \right)^{\frac{\gamma - 1}{\gamma}} - 1 \right]} - u_\infty \tag{2.12}$$

Let's define $\vec{f}_{vw} = -\rho\Delta\bar{u}\vec{q}$. On $S_\infty$ the flow is in the freestream state and therefore $\Delta\bar{u} = 0$. It is thus possible to extend the integration to $S_D + S_\infty$. Moreover, on the aircraft surface $S_A$, $\left(\vec{f}_{vw} \cdot \vec{n}\right) = 0$. So, it is possible to extend the integration further to:

$$D = D_p + D_f = D_v + D_w = \iint_{S_D+S_\infty+S_A} \left(\vec{f}_{vw} \cdot \vec{n}\right) dS = \iiint_V div\, \vec{f}_{vw} dV \tag{2.13}$$

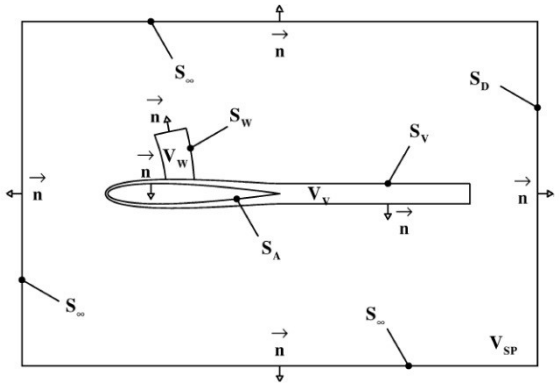


**Figure 2.3: Boundaries and control volumes for far-field drag breakdown (*D. Destarac, 2008)***

By definition, there are neither viscous effects nor heat conduction in $V - (V_V + V_W)$ (Figure 2.3). Consequently, entropy and stagnation enthalpy and thus also $\Delta\bar{u}$ do not vary along a streamline. It follows that $div\vec{f}_{vw} = 0$ in $V - (V_V + V_W)$:

$$\iiint_V div\, \vec{f}_{vw} dV = \iiint_{V_V+V_W} div\, \vec{f}_{vw} dV \tag{2.14}$$

In a flow without trailing vortices (no induced drag), this formula gives the total drag. In the general case of a lifting three-dimensional flow, it gives the components of drag produced through irreversible processes. This form of drag is called "irreversible" drag. It is easy to obtain that viscous drag and wave drag are given by:

$$D_v = \iiint_{V_V} div\, \vec{f}_{vw} dV \,, D_w = \iiint_{V_W} div\, \vec{f}_{vw} dV \tag{2.15}$$

It is possible to define the induced drag $D_i$ ensuring an exact far-field / near-field drag balance, having $\vec{f} = \vec{f}_{vw} + \vec{f}_i$. Defining $S_V$ and $S_W$ the outer boundaries of respectively the volumes $V_V$ and $V_W$, from Eq. 2.8 after some manipulation it is possible to obtain (*D. Destarac, 2003*):

$$D_p + D_f = \iint_{S_V+S_W} (\vec{f} \cdot \vec{n}) dS = \iint_{S_V+S_W} (\vec{f}_{vw} \cdot \vec{n}) dS + \iint_{S_V+S_W} (\vec{f}_i \cdot \vec{n}) dS = \cdots$$

$$= D_v + D_w + \iiint_{V_V+V_W} div\, \vec{f}_i dV - \iint_{S_A} (\vec{f}_i \cdot \vec{n}) dS \quad (2.16)$$

Van der Vooren and Destarac's general definition of induced drag is then:

$$D_i = \iiint_{V_V+V_W} div\, \vec{f}_i dV - \iint_{S_A} (\vec{f}_i \cdot \vec{n}) dS \quad (2.17)$$

This definition thus ensures an exact near-field / far-field drag balance:

$$D_p + D_f = D_v + D_w + D_i \quad (2.18)$$

As *D. Destarac* (*2003*) shows, the classical formulation of the induced drag can be derived from the present definition. Thus, the abovedescribed definition is consistent with this.

#### 2.1.2.2 Numerical deviation from the theory: the Spurious Drag

An important discrepancy between the numerical and theoretical aspects of drag is that numerical technique used to solve the equation may generate what is termed ***spurious drag***, a *non-physical purely numerical process*. When the first numerical methods to solve the Euler equations were derived, spurious losses of stagnation pressure (or spurious increasing of entropy along streamlines) were detected, and explained through numerical viscosity and grid inadequacy (*A. Jameson, 1981; A. Rizzi, 1985*). This phenomenon (sometime described as numerical boundary layer) was then linked to the spurious viscous drag production. *A. Rizzi* (1985) identified four possible causes of this spurious production: mesh spacing, convective difference scheme, artificial dissipation model and boundary condition.

*M. Gariépy et al.* (*2010*) clearly showed spurious entropy in inviscid flow around an airfoil, creating "false" boundary layer, and *D. Destarac* (*2008*) shows peaks of spurious drag production in correspondence to shock waves but also in areas of the flow (in particular around the leading edge of an airfoil) where, with an inviscid flow model, there is no physical justification for drag generating processes. Figure 4.4 shows two-dimensional solutions of the Euler equations around the NACA0012 airfoil with zero angle of attack at Mach number 0.77.

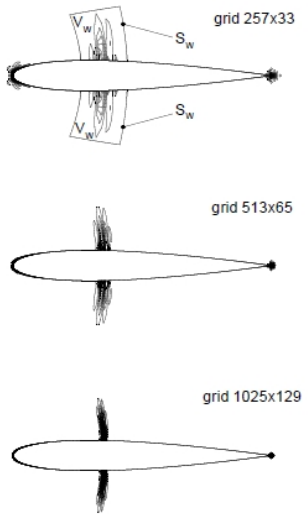


**Figure 2.4: Entropy generation in compressible inviscid flow, depending on the mesh size (*D. Destarac, 2008)***

In the low-subsonic range, the solution of the Euler equations for uniform inflow condition should be identical to the potential flow solution. But the main difference, as stated before, is that Euler equations do not guarantee the calculated flow remains irrotational or isentropic. Theoretically, in inviscid flow it is possible to detect entropy varies along a streamline only across shock discontinuities, but Figure 2.4 shows that numerically this is not the case. Beside the dominant entropy production in the shock wave areas, other areas of entropy production appear at the leading edge and at the trailing edge of the airfoil. The greater part of spurious drag comes from the flux around the leading edge (*D. Destarac, 1993*). The entropy generation in these unjustified areas gives the spurious drag component and, in inviscid flow, it is usually considered as a unique indicator of the presence of numerical dissipation in the scheme. By monitoring and post-processing the evolution of the entropy a direct measure of the quality of the numerical scheme on the selected grid can be provided (*C. Hirsch, 2007*).

Figure 2.4 illustrates also the effect of grid refinement: solutions on three increasingly refined (structured) grids are compared. Noticeable is the decay of the spurious phenomena at the leading edge with grid refinement (*D. Destarac, 2008*).

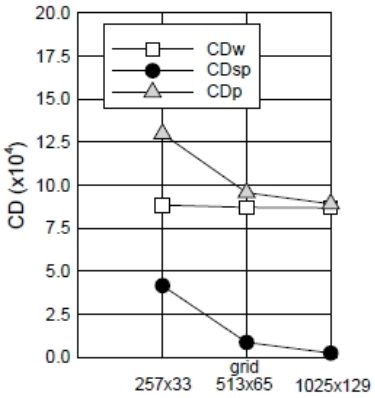


**Figure 2.5: Influence of grid refinement on wave, pressure and spurious drag (*D. Destarac, 2008)***

Figure 2.5 shows the influence of grid refinement on wave drag, pressure drag and spurious drag for the same test-case. It is important to underline that, since two-dimensional inviscid transonic flow is considered, the terms $D_v$, $D_f$ and $D_i$ of Eq. 2.18 are equal to zero. Thus, the near-field / far field drag balance is:

$$D_p = D_w \tag{2.19}$$

It is possible to see that wave drag is much less affected than pressure drag since: some spurious phenomena may also occur inside the wave drag control volume $V_W$, but the part produced outside it is clearly dominant. Drag thus computed in far-field proves much less dependent on mesh refinement than pressure drag. For a given mesh density, it tends to be more accurate (*D. Destarac, 2008*).

It is important to underline that *D. Destarac* (*1993*) showed that far-field drag is not intrinsically more accurate, nor less accurate, than near-field drag, since the integration of all sources of drag in the field (physical and spurious) tends to the same result as near-field integration if the mesh size tends to infinite.

#### 2.1.2.3 Far-field drag extraction for Aerodynamic Optimization

The far-field approach results to be very useful for aerodynamic optimization (*W. Yamazaki, K. Matsushima, K. Nakahashi, 2008; W. Yamazaki, 2015; F.* Bisson, S. Nadarajah, 2014). With a very coarse mesh as must be used in three-dimensional optimization for computational cost reasons, drag cannot be computed accurately by pressure integration. In (*D. Destarac, 1993*) a

simple case of optimizing a rectangular, unswept, untwisted, wing of high aspect-ratio, in transonic flow, achieving drag minimization is shown. The same optimization by using far-field and near-field to compute the drag is undertaken. The pressure integration based near-field approach involves an amount of spurious drag around the leading edge which can be avoided by the far-field approach. If the near-field drag is minimized, the optimization process reduces the un-physical spurious drag rather than the physical wave drag. Conversely, far-field drag minimization, ignoring the spurious contribution by the exclusion of the leading-edge area, reduces the true, physical, wave drag.

The discernment of the drag sources imparted by far-field analysis and component breakdown is also very important. It has been illustrated by D. Destarac by researching different twist distributions of a wing minimizing each drag component separately (lift-induced and wave drag), and the sum of the two (total drag in inviscid flow).

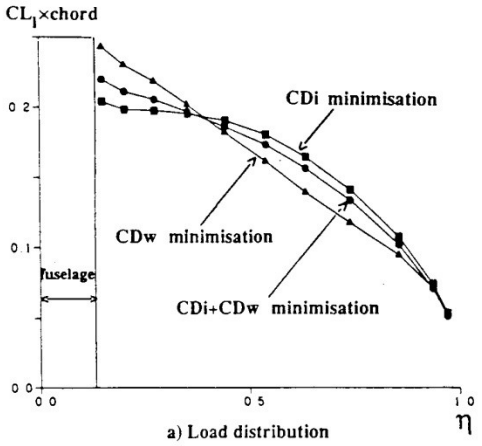


**Figure 2.6: Wing drag minimization by using drag breakdown (*D. Destarac, 1993)***

Figure 2.6 shows how different the optimized wing can be while reducing one or another drag component. In that case, for instance, minimum wave drag is obtained by unloading the two outer thirds of the wing, and increasing load of the inner third. Consistently minimizing the total inviscid drag leads to a load distribution lying between the previous result and the typical elliptic load distribution of induced drag minimization. It is important to underline that the possibility to treat and optimize the single drag components separately is very useful in understanding the physics of the considered phenomena, while keeping the other components frozen. *W. Yamazaki* (*2015*) shows how the breakdown approach allows drag reduction effect to be analysed quantitatively, and to visualize drag source distribution in its flow-field intuitively. Moreover, *W. Yamazaki et al.* (*2008*)

underlines that the results of the optimization based on the drag-decomposition method are more reliable and efficient.

### 2.1.3 Geometry and Mesh features

A Forward Swept Wing (FSW) architecture is chosen. As introduced in Sec.1.1, the main reason is that an unconventional geometry needs to be considered and the chosen one is not conventional but enough know to evaluate possible results of the design approach will be presented later on.

The problem of convergence, Euler formulation limits and what all that implies on detailed geometrical and mesh features are examined here. Starting from the airfoils definition, passing through the wing with a particular focus on the wing tip before introducing the wing-body configuration, an analysis of the abovementioned features will be given.

#### 2.1.3.1 Airfoils and isolated wing

The geometry of the wing was not given a priori. First of all, the airfoils to be used to generate the wing geometry were chosen. Since FSW architecture presents particular aerodynamic features at the wing-body intersection, the ONERA airfoil *OALE10* was chosen. The objective was to alleviate the effect of the flow acceleration over the surface at the root of the wing. Since this flow acceleration usually has no impact on the wing outboard, the influence zone of that airfoil was kept no more that 25% of the span. The majority of the wing was generated using the ONERA supercritical airfoil *OAT15A*.

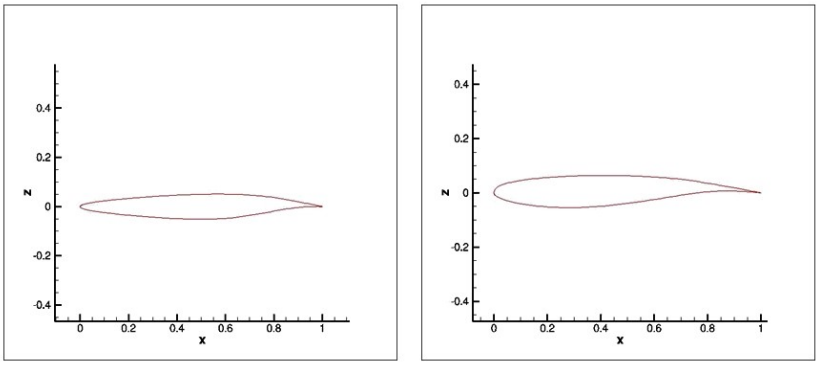


**Figure 2.7: On the left, the airfoil OALE10; on the right, the airfoil OAT15A**

Figure 2.7 shows the geometry of the airfoils and the flow domain meshes that were used to get the aerodynamic properties of them. The results of the investigation are shown in Sec. 2.1.4.1.

At the beginning, in order to generate the wing geometry the modeller *SUMO*® by *Larosterna Engineering Dynamics Lab* was used (*M. Tomac et al., 2010; A. Rizzi et al., 2011; A. Bérard et al., 2008; M. Zhang et al., 2011, 2012*). It is a surface modeller aimed at rapid creation of aircraft geometries and automatic surface mesh generation. Fuselage surfaces are modelled by modifying the shape of several cross-sections perpendicular to the longitudinal direction. Wing surfaces are created from airfoils, which can be read from files or generated. Although *SUMO*® is able to generate geometries, the CAD software *CATIA*® was preferred and then used all over the design process since its high degree of geometry control options and effectiveness in generating very good quality aerodynamic surfaces. Very appreciate is the automatic generation of high quality unstructured mesh that *SUMO*® offers, which is actively developed in order to streamline the design workflow. Unfortunately, the CFD software *elsA* handles structured mesh, therefore even this advantage could not be used.

As described above, *CATIA*® was used to generate the wing geometry and the ONERA project called *NACRE* (*J. Frota, 2006*) was used as reference for the wing planform dimensions. The work aimed at integrating and validating technologies that will enable new aircraft concepts to be assessed and potentially developed. Table 2.1 summarize the baseline wing planform characteristics and the wing geometry is shown in Figure 2.8.

| | | | |
|---|---|---|---|
| Semi-Span | [m] | b/2 | 19.5 |
| Sweep at 25% | [°] | $\varphi_{1/4}$ | 18.15 |
| Semi-Surface | [$m^2$] | S | 80 |
| Taper ratio | [-] | λ | 0.265 |
| Aspect ratio | [-] | AR | 9.45 |
| Root chord | [m] | $C_r$ | 6.225 |
| Tip chord | [m] | $C_t$ | 1.649 |

**Table 2.1: Planform dimensions of the wing**

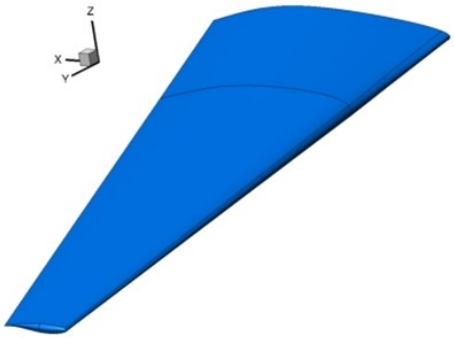


**Figure 2.8: Wing Geometry**

#### 2.1.3.2 Geometrical and mesh characteristics for qualitative Euler analysis

In this section a detailed analysis of the wing geometry and mesh is provided. Following the limits of the Euler formulation, some features of the baseline wing geometry were modified, as well as the mesh morphology. The far-field approach introduced in Sec. 2.1.2 was used for monitoring the mesh quality due to the spurious drag extraction. Moreover, particular attention was paid to the CFD analysis convergence. Figure 2.9 shows the geometry and mesh features of the baseline wing.

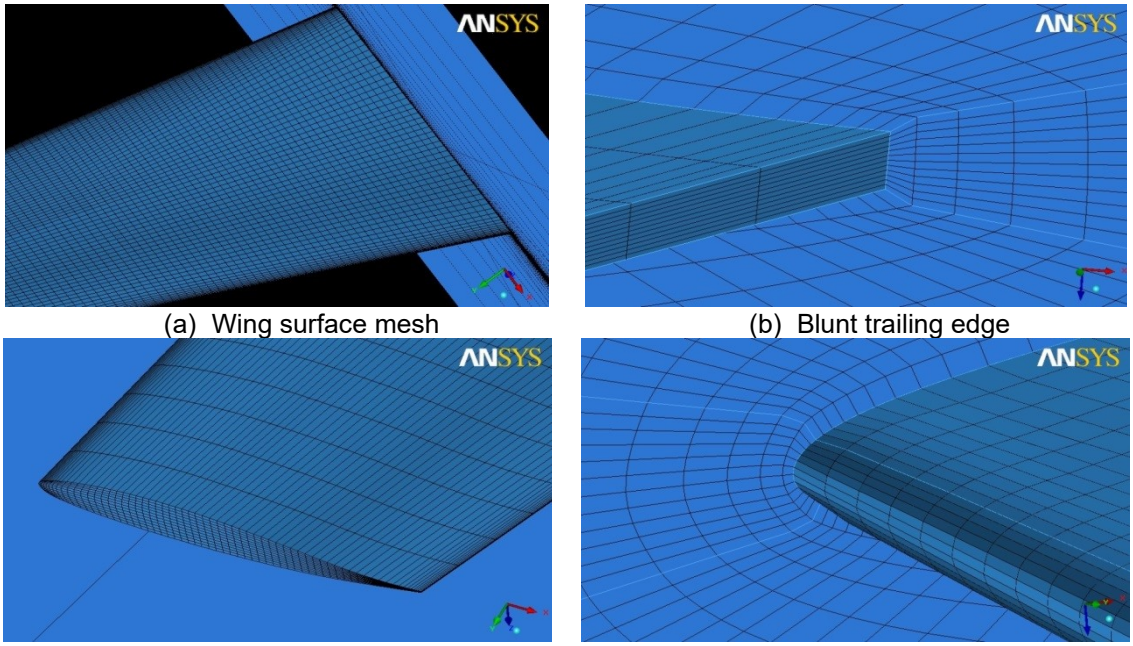


(a) Wing surface mesh (b) Blunt trailing edge

(c) Cut wing tip (d) Leading edge

**Figure 2.9: Baseline wing geometry and mesh features**

The wing is characterized by *blunt trailing edge* and *cut wing tip* (Figure 2.9 *a* and *b* respectively). For what concerns the mesh, the first choice was to have *uniform* and *isotropic* mesh for the wing surface and for the mesh planes parallel to it (Figure 2.9 *c*), while a more *anisotropic* mesh on the mesh planes perpendicular to the wing (Figure 2.9 *d*). The mesh size is about 800 000 cells.

Good convergence of the CFD analysis has to be ensured. Actually, it is an important requirement for the calculation of the adjoint sensitivity which will be used later for shape optimization (Chapter 3). Moreover, a relative spurious drag less than 5% is desirable for reliable aerodynamic force calculation. The relative spurious drag is expressed by:

$$rel\_D_{sp} = {D_{sp}}/{T_{ffd}} \cdot 100 \tag{2.19}$$

where $D_{sp}$ is the spurious drag and $T_{ffd}$ is the total far-field drag. The above presented mesh fulfilled the convergence requirements of the forthcoming aerodynamic optimisation (Sec. 3.2) but the CFD calculation exhibit 70% of relative spurious drag, which is significantly higher that the reasonable limit of 5%. Trying to increase the mesh quality of the configuration, a new wing mesh was produced keeping the same mesh size but following the criterion expressed by *J.C. Vassberg* and *A. Jameson*

(*2010*) and *D. Destarac* (*2011*), Figure 2.10. For a good Eulerian calculation, the mesh on the planes perpendicular to the wing must follow two important indications:

- the cells have to be as perpendicular as possible to the wing surface and very regular, almost square;
- the change in direction from a cell to another has to be taken under control in order to have very smooth mesh behavior.

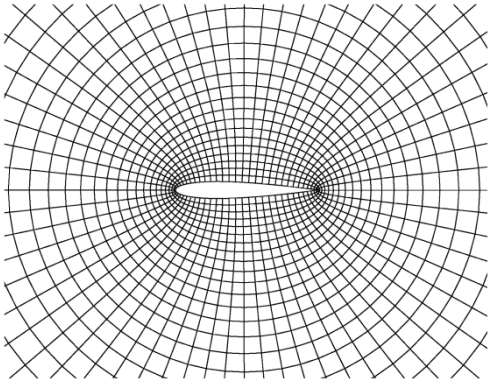

**Figure 2.10: Eulerian mesh, J.C. Vassberg and A. Jameson (2010)**

Following the abovementioned indications, a second wing mesh was generated and tested. Figure 2.10 shows the new mesh feature at the leading and trailing edges. Note that no geometrical modification was applied.

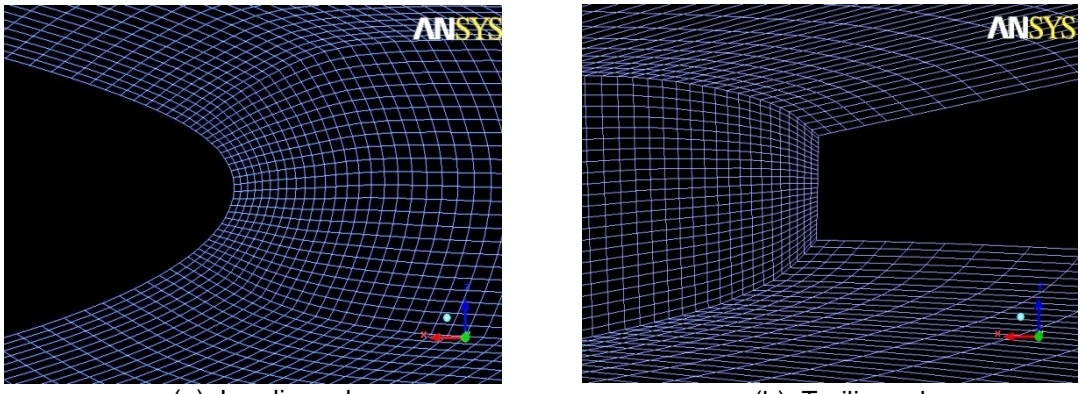


(a) Leading edge (b) Trailing edge

**Figure 2.11: Meshes on a plane perpendicular to the wing span direction**

By comparing Figure 2.11 with Figure 2.9 it is possible to notice that the mesh on the plane perpendicular to the wing results to be much more *isotropic* than before and the cells are almost

*perpendicular* to the wing surface everywhere. The mesh behaviour is now smoother. The skewness of the cells was kept the lowest possible ending up with a squared mesh.

From these modifications, the spurious drag dropped down to 3%, while the convergence of the analysis was unacceptable. Looking at the residuals in the fluid domain, very high values were found to the cells near by the trailing edges. As described by *A. Viti et al.* in *2015*, Euler simulations suffer difficult convergence whenever a blunt edge is present. It is probably due to the fact that cells in the blunt trailing edge have high aspect ratio hence correction of pressure from the cell centre to the wall to fulfil an accurate inviscid well boundary may start to oscillate showing high variation from one cell to another. Some less accurate inviscid wall boundary treatments like direct extrapolation of pressure cell centre to wall may damp this unstable behaviour.

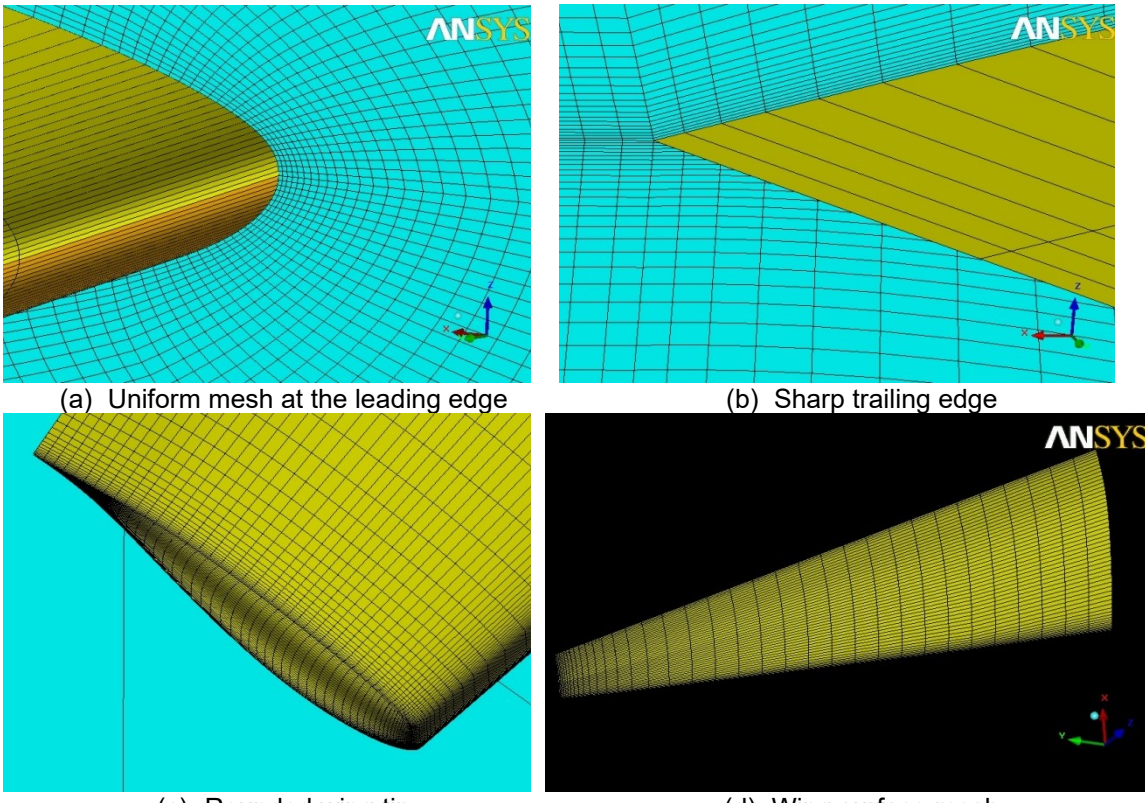


(a) Uniform mesh at the leading edge (b) Sharp trailing edge

(c) Rounded wing tip (d) Wing surface mesh

**Figure 2.12: Final wing geometry with sharp trailing edge, rounded wing tip and uniform**

As a consequence, the blunt trailing edge was modified in a sharp one and the cut wing tip in a round one (Figure 2.12). The mesh features were not modified. This final configuration ensured a CFD analysis convergence and very reliable result with a very low spurious drag, while keeping the same mesh size of about 800 000 elements. Actually, this last mesh was considered as *fine* mesh

for preliminary design purpose, thus a *coarse* mesh was also generated with about 120 000 elements and compared with the abovementioned one to see if it could be used instead. The comparison is shown in Sec. 2.1.4.22. Table 2.2 summarizes the steps to have an acceptable preliminary design mesh.

| | Characteristics | Size | Spurious | Convergence |
|---|---|---|---|---|
| **First step mesh** | • Blunt trailing edge end cut wing tip<br>• Uniform and isotropic mesh for planes parallel to the wing<br>• Anisotropic mesh for the planes perpendicular to the wing | 800 000 cells | 70% | 7 order magnitude |
| **Second step mesh** | • Blunt trailing edge end cut wing tip<br>• Cells perpendicular to the wing surface<br>• Very smooth change in direction from a cell to another | 800 000 cells | 3% | Unacceptable/ Not converged |
| **Third step mesh** | • Sharp trailing edge and rounded wing tip<br>• Cells perpendicular to the wing surface<br>• Very smooth change in direction from a cell to another | 800 000 cells | 10% | 4-5 order magnitude |
| **Preliminary design mesh** | • Sharp trailing edge and rounded wing tip<br>• Cells perpendicular to the wing surface<br>• Very smooth change in direction from a cell to another | 120 000 cells | 30% | 4-5 order magnitude |

**Table 2.2: Wing mesh and geometry modifications**

It is important to notice that the first wing geometry and mesh expressed a very good convergence (even better than the last one), although blunt trailing edge and cut wing tip were still present. Probably, the reason why the first case gets a zero-machine convergence (single precision where used, then 8 digits are considered, so 7 order of magnitude convergence is the limits of the results precision), while the second case performs serious convergence problem while having the

same geometry features, lies on the spurious drag level. For the first case the relative spurious drag was about 70% while the second case is characterized by a very low level of about 3% that means almost no spurious drag and, consequently almost no numerical dissipation (refer to Sec. 2.1.2.2). It is possible that the high numerical dissipation present in the first case could “dissipate” incipient flow detachment problem (and consequent residuals increment) for which Euler formulation suffers.

Another limit of the Euler model was found while increasing the wing angle of attack. For relatively high global angle of attack convergence problem occurs. This was observed for the flexible wing, whenever the local angle of attack reaches a certain level. The problems occur close to the wing tip trailing edge where the rounded wing tip is characterized by a very high curvature. For this particular geometry, once the angle of attack was greater than 3,5 – 4 degree, the residuals increase and the convergence is no-longer ensured. In order to obtain a converged simulation, as soon as the angle of attack become greater that the abovementioned limits the artificial dissipation has to be increased too much, with a consequent deterioration of the drag estimation reliability. For this reason, the cruise conditions are, for the Euler formulation, the only possible ones considered and whenever aero-elastic analysis is undertaken, the structure cannot be too flexible to ends up with high local angle of attack.

#### 2.1.3.3 The wing-body configuration

Once that the wing was defined, a forward swept wing configuration with a lifting fuselage was generated. In Figure 2.13 the top view of the aircraft is shown, while Table 2.3 gives the main dimensions.

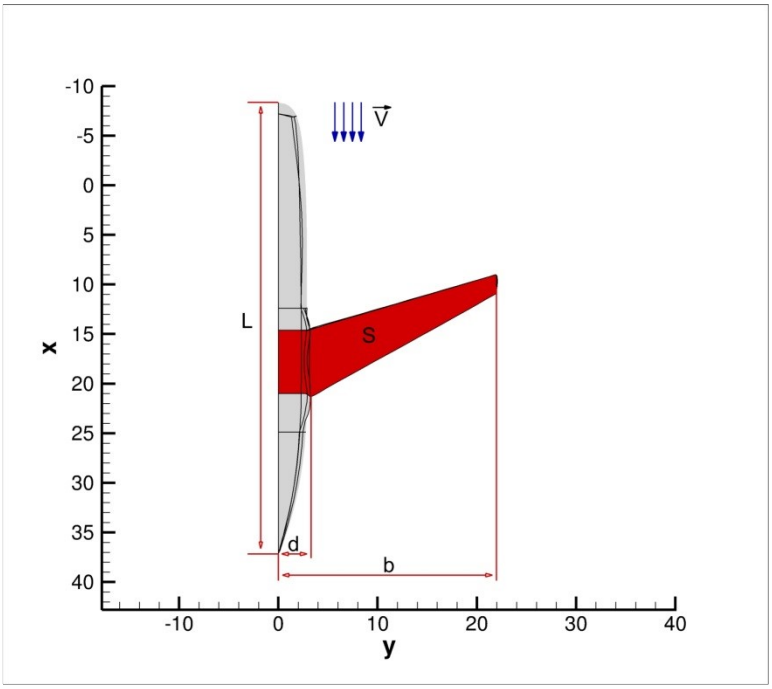


**Figure 2.13: Top view of the architecture**

| | | | |
|---|---|---|---|
| Fuselage length | [m] | L | 45.65 |
| Root position | [m] | d | 3.3 |
| Span | [m] | b | 43.8 |
| Reference Surface | [$m^2$] | S | 193.4 |
| Sweep at 25% | [°] | $\varphi_{1/4}$ | 18.15 |
| Aspect ratio | [-] | AR | 9.45 |
| Taper ratio | [-] | λ | 0.265 |
| Root chord | [m] | $C_r$ | 6.225 |
| Tip chord | [m] | $C_t$ | 1.649 |

**Table 2.3: Wing-body configuration dimensions**

The isolated wing mesh size was about 120 000 cells and was considered adequate for preliminary design purpose. The wing-body geometry and mesh were created by maintaining the wing geometry and mesh characteristics introduced in the previous section. The wing-body mesh size is about 170 000 elements and it performs good CFD analysis convergence.

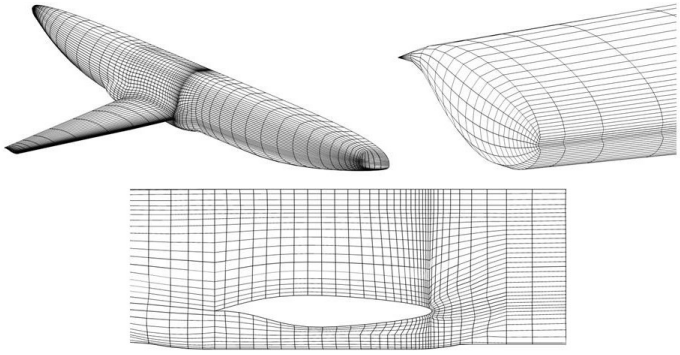

**Figure 2.14: Wing-Body mesh**

### 2.1.4 Aerodynamic Investigation

The procedure for producing an adequate mesh was an iterative procedure. Several aerodynamic investigations of the isolated wing were carried out in order to find a good compromise between convergence and mesh quality. Moreover, a CFD campaign was undertaken in order to understand whether the fuselage was needed or isolated wing was enough for preliminary design investigation. Mesh convergence analysis of the wing-body configuration was addressed. In the next sections, these preliminary aerodynamic investigations are presented.

#### 2.1.4.1 Airfoil aerodynamic characterization

In Sec. 2.1.3.1 the two airfoils used to generate the wing are presented. In the inboard wing, the airfoil *OALE10* is used. This is a particular airfoil designed by ONERA for inboard flow acceleration occurring for forward-swept wing configuration. Figures 2.15 and 2.16 show the aerodynamic characterization of it for 3 Mach numbers: $M = 0.5, 0.6, 0.7$. It is possible to notice that the complete researched polar has not been traced for the airfoil at $M = 0.5$. This is due to the fact simulation convergence problems have been encountered for angle of attack higher that 4°. A possible reason of that may be related to the level of numerical dissipation generated during the research of the numerical solution. As matter of the fact, the Euler formulation chosen to describe the flow is a non-linear hyperbolic partial derivative equation. Numerical solution of non-linear hyperbolic equations may suffer oscillations due to the numerical scheme adopted to discretize the equations. Numerical viscosity (that generates spurious drag Sec.2.1.2.2), introduced by the numerical scheme and by the discretization of the continuous domain, helps (and sometime is enough) to suppress the abovementioned oscillations (*X. Karalliu, 2018; J. Li et al., 2009*). It is then

possible that, for low velocity, the numerical dissipation together with the artificial viscosity constantly added for Euler solutions are not enough to stabilize the numerical solution.

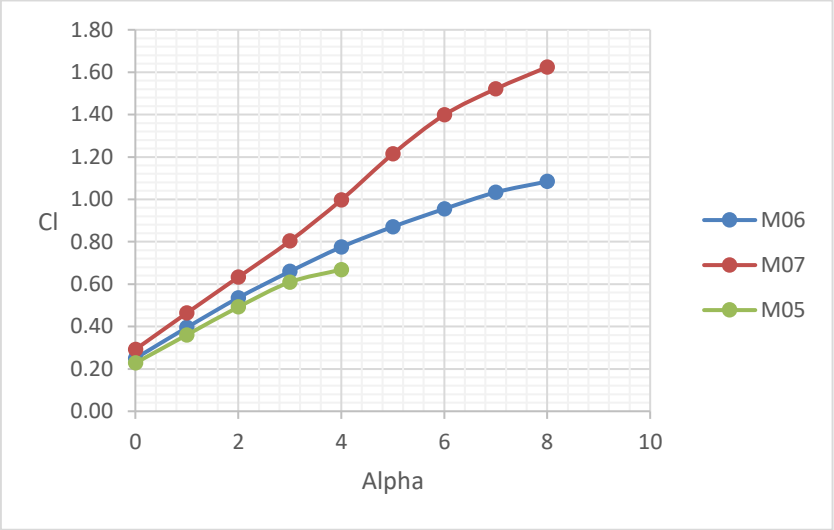


**Figure 2.15: CL - Alpha curve of the airfoil OALE10**

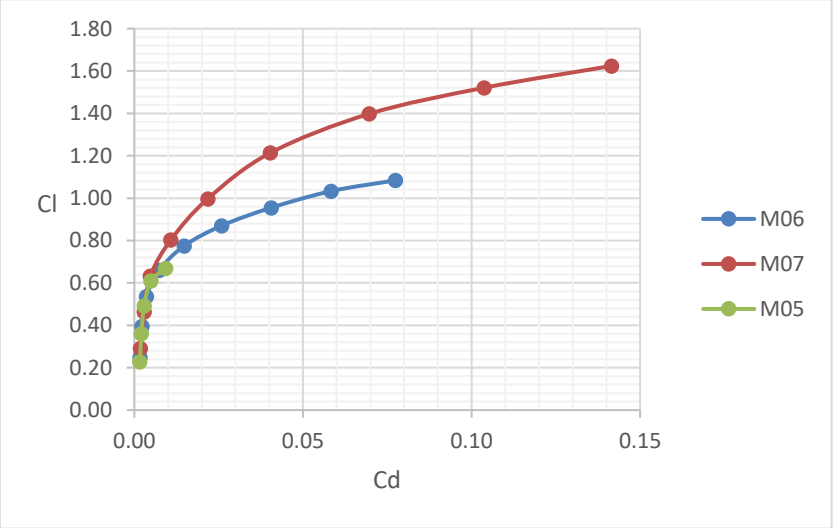


**Figure 2.16: Polar of the airfoil OALE10**

The outboard wing is generated using the classic transonic supercritical airfoil *OAT15A* (*V. Brunet et al., 2005; L. Jacquin et al., 2005*). Below, the aerodynamic behaviour is presented.

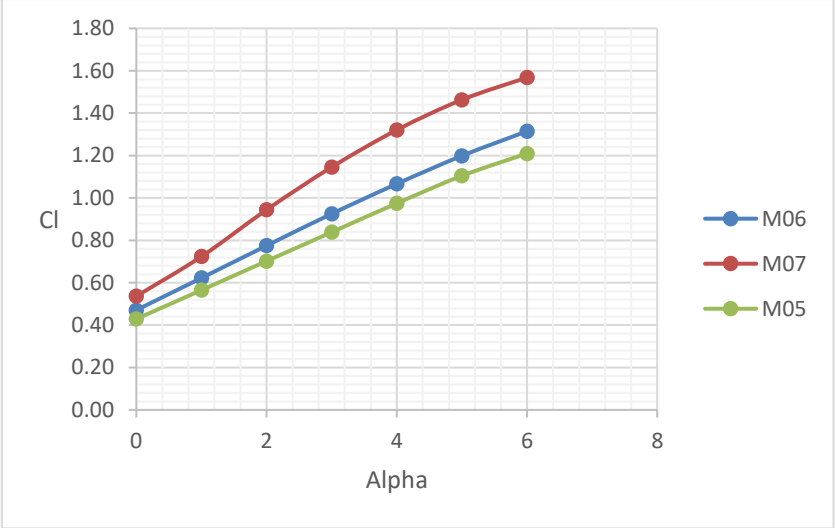


**Figure 2.17: CL - Alpha curve of the airfoil OAT15A**

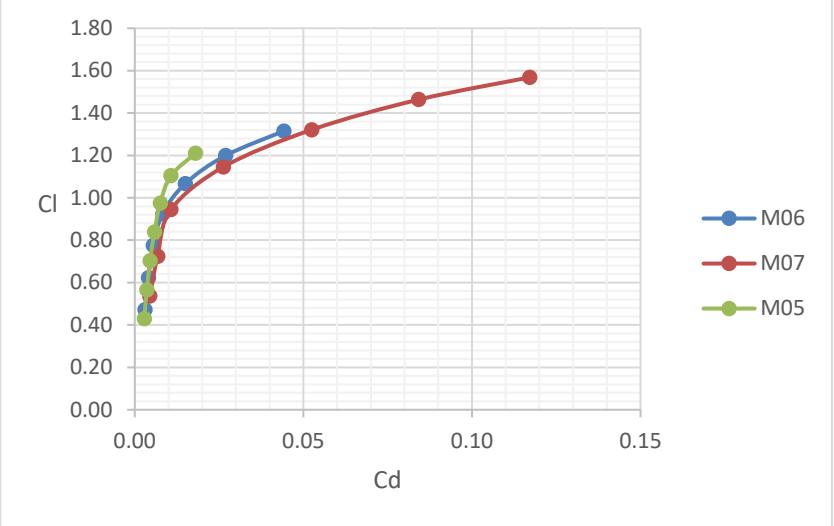


**Figure 2.18: Polar of the airfoil OAT15A**

### 2.1.4.2 Mesh convergence study for the isolated wing

An Eulerian mesh, together with some geometrical modifications, is able to ensure the convergence of the simulations and good quality of the results in terms of spurious drag. As described in Sec. 2.1.3.2, the isolated wing mesh size is about 800 000 elements. A coarse mesh of about 120 000 elements was generated to speed up the aerodynamic analysis. Comparing the results of the aerodynamic investigation using the two meshes, it is possible to see a small underestimation of lift and far-field total inviscid drag coefficients of the coarse mesh with respect to the fine one. Figure 2.19 and Figure 2.20 show the $C_l - \alpha$ and the $C_{d_{ff}} - \alpha$ curves respectively.

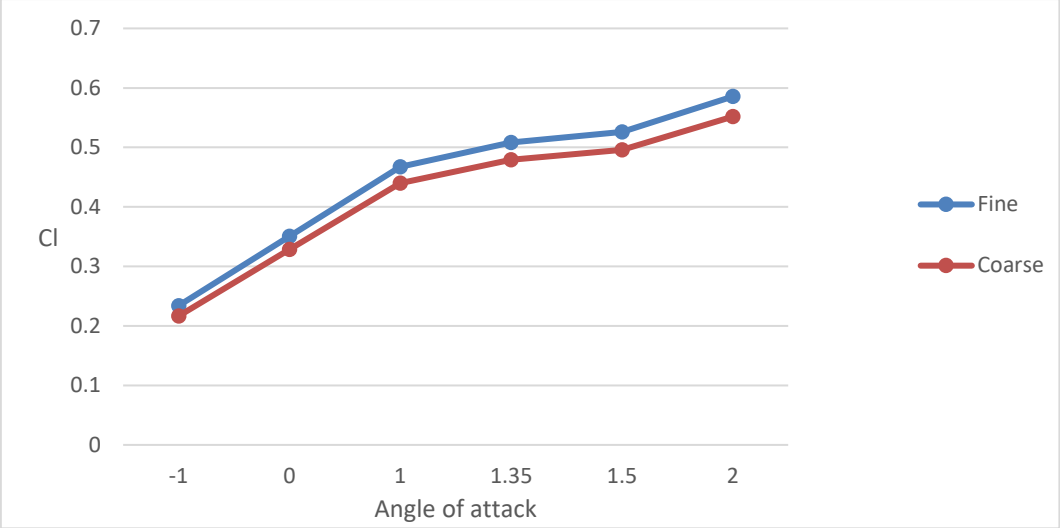


**Figure 2.19: $C_l - \alpha$ curve for fine and coarse isolated wing mesh**

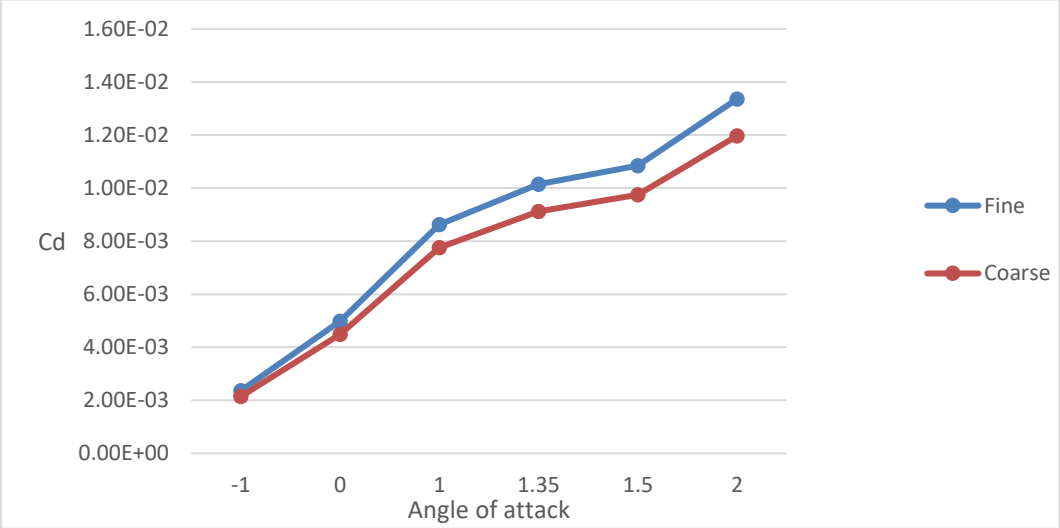


**Figure 2.20: $C_{d_{ff}} - \alpha$ curve for fine and coarse isolated wing mesh**

The red curve corresponds to the coarse mesh, while the blue one corresponds to the fine one. The green curve represents the error, in percentage, of the aerodynamic coefficients with respect to the evaluation calculated with the fine mesh. The underestimation of the lift coefficient for the coarse mesh is between 5.7% and 7.4%, while the one of the drag coefficient runs between 9.1% and 10.4%. It is important to recognize that the values of error are relative to evaluations done by keeping the same angle of attack for the two meshes. It is also important to highlight that, usually, the aerodynamic design is done by choosing a reference lift coefficient that comes from aircraft weight and mission estimation. Thus, error estimation for drag calculation at the same lift is much more relevant than comparing the coefficients at the same angle of attack.

| $C_L = 0.5$ | Fine | Coarse | Err % |
|---|---|---|---|
| Angle of attack [°] | 1.28 | 1.538 | 20.16 |
| $C_{d_{ff}}$ tot inviscid | $98.3 \cdot 10^{-4}$ | $99.0 \cdot 10^{-4}$ | 0.736 |

**Table 2.4: Comparison between fine and coarse meshes at constant $C_L$**

Table 2.4 shows that the coarse mesh estimates the angle of attack with an error of about 20%, while an almost perfect matching for the far-field total inviscid drag coefficient (less than 0,75%). That means that the coarse mesh can be used for polar estimation and efficiency optimization without significant loss of fidelity. The coarse mesh was adopted for the design phase.

The far-field total inviscid drag appears to be independent of the mesh size, then the far-field technique the good approach for reliable aerodynamic design and optimization when coarse mesh is used, as reported in Sec. 2.1.2.2. The spurious drag values for the two meshes are shown in Table 2.5.

| | Cd spurious – fine mesh | Cd spurious – coarse mesh |
|---|---|---|
| $\alpha = 0°$ | $28.8 \cdot 10^{-4}$ | $110.0 \cdot 10^{-4}$ |
| $\alpha = 1°$ | $31.6 \cdot 10^{-4}$ | $115.0 \cdot 10^{-4}$ |
| $\alpha = 2°$ | $39.2 \cdot 10^{-4}$ | $129.0 \cdot 10^{-4}$ |
| $C_L = 0.5$ | $33.0 \cdot 10^{-4}$ | $121.0 \cdot 10^{-4}$ |

**Table 2.5: Spurious drag for different flight conditions**

The spurious drag results provide a good indication of the quality of the mesh, while the far-field approach is able to detect that and consider the physical drag only.

#### 2.1.4.3 Isolated wing vs wing-body configuration

In order to assess the role of the fuselage on the aerodynamics predictions, rigid aerodynamic analyses were undertaken and, as it will be introduced later on (Sec.2.3.3.2), elastic aerodynamic analyses of the isolated wing and wing-body configurations were compared. The coarse mesh is adopted.

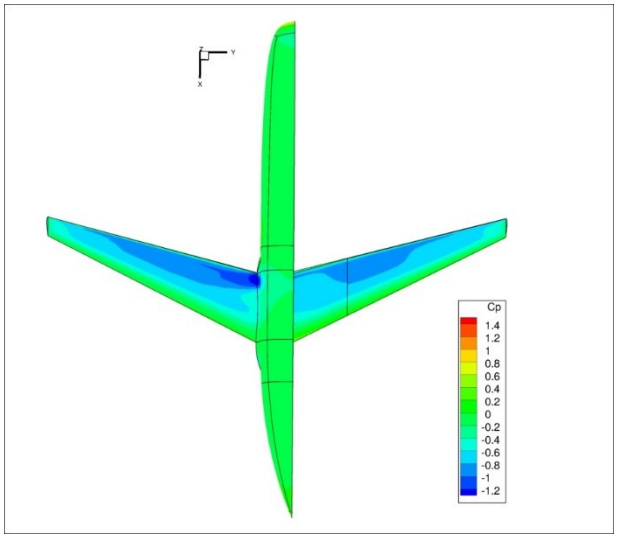


**Figure 2.21: Comparison between isolated wing and wing-body surface pressure field for $C_L = 0,5$**

The pressure distribution of the isolated wing skin and wing-body configuration skin are shown in Figure 2.21. The comparison helps to underline the importance of the aerodynamic interaction between the wing and the fuselage (*A. Viti et al., 2015; D. Baumgärtner at al., 2016*). As it is possible to see in figure, the main differences are at the wing-fuselage intersection. For the case of isolated wing the shock free condition is present, while for the wing-body configuration a strong inboard shock is present. It is thus evident how important the inclusion of the fuselage is in this stage of design since the nature of the flow field may change. The different treatment for the shock and shock free condition while an aerodynamic optimization is performed will be described in Chapter 3. Table 2.6 shows the aerodynamic results for the isolated wing and the wing-body configuration at $C_L = 0.5$.

| $C_L = 0,5$ | Isolated wing | Wing-body |
|---|---|---|
| Alpha [°] | 1.538 | 1.364 |
| $C_{dff\_wave}$ | $0.0 \cdot 10^{-4}$ | $10.38 \cdot 10^{-4}$ |
| $C_{dff\_ind}$ | $99.0 \cdot 10^{-4}$ | $84.17 \cdot 10^{-4}$ |

**Table 2.6: Comparison between isolated wing and wing-body for $C_L = 0,5$**

From the previous analysis, the wing-body configuration was then preferred to the isolated wing in determining aerodynamic performance.

#### 2.1.4.4 Comparison among backward-swept, forward-swept and zero-sweep rigid wings

In the present section a comparison among different swept wing configurations is presented. In particular, the forward-swept wing (FSW), the backward-swept wing (BSW) and the no-sweep wing (NSW) not optimized wings are considered. The wing geometry is exactly the same for the three cases. The sweep angle for the backward-swept wing is, in module, the same as the forward-swept one. The aerodynamic investigations were carried out at constant lift coefficient ($C_L = 0.635$) and at the same flight conditions. Table 2.7 shows the results for the three configurations.

| $\boldsymbol{C_L = 0.635}$ | Alpha [°] | $C_{dff\_wave}$ | $C_{dff\_ind}$ |
|---|---|---|---|
| NSW | 1.490 | 37.18e-4 | 128.18e-4 |
| BSW | 1.435 | 55.21e-4 | 123.96e-4 |
| FSW | 2.401 | 37.05e-4 | 136.48e-4 |

**Table 2.7: Comparison of configurations with different sweep angle**

In subsonic flow for isolated wing, for the same flight conditions a swept wing usually produces less lift than the same one unswept. The lift of the swept wing is reduced by a factor of approximately $\cos(\varphi_{25\%})$, with $\varphi_{25\%}$ sweep angle at 25% of the wing chord, with respect to the unswept wing lift. Thus, backward and forward swept wings with the same absolute value of sweep angle should produce the same lift (*I.H. Abbott* and *A.E. Von Doenhoff, 1959*). The transonic flow is usually different to the subsonic one. For the cases considered, it is possible to see (Table 2.7) that the NSW is not the system that produces the higher lift, while BSW is. Moreover, the BSW and FSW are different.

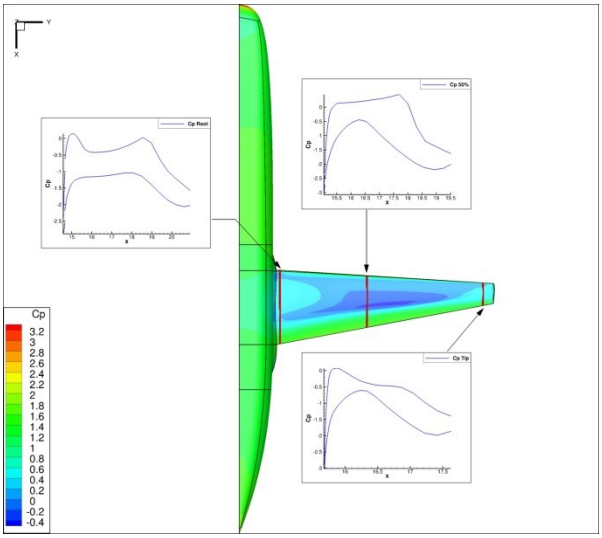


(a) NSW pressure coefficient distribution

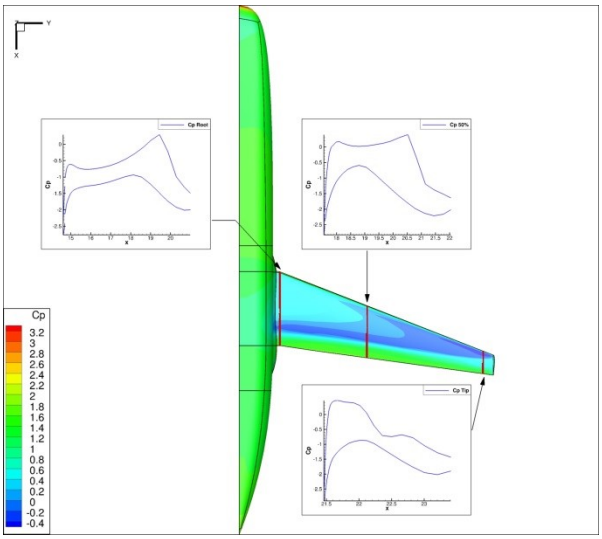


(b) BSW pressure coefficient distribution

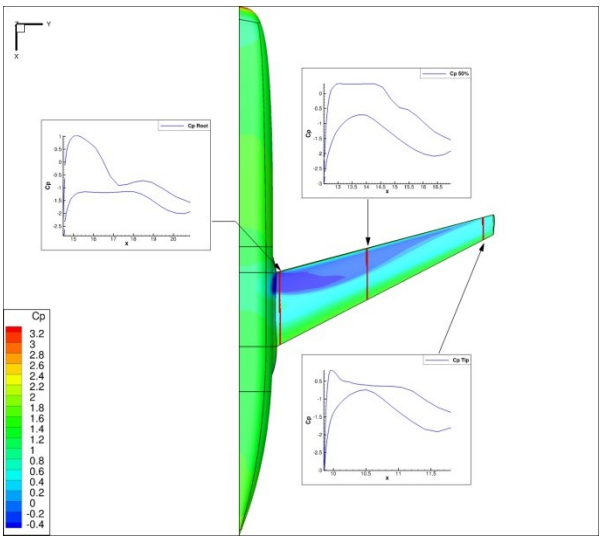


(c) FSW pressure coefficient distribution

**Figure 2.22: Pressure coefficient distribution for the three wings architecture**

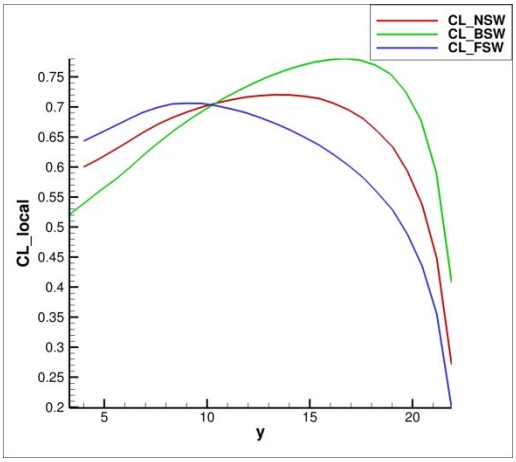


**Figure 2.23: Lift coefficient spanwise distributions for different sweep angles**

Figure 2.22 shows the pressure distribution of the three architectures. It is possible to see that the possible reason of the fact that the BSW needs an angle of attack much smaller than what FSW needs is that strong inboard shock occurs for the latter. Moreover, the shock on the FSW geometry is close to the leading edge so that the lifting surface area is reduced significantly. It is important to notice that this particular phenomenon occurs inboard and, as can be seen in Figure 2.23 is the most important lifting surface region for FSW. Concerning the NSW architecture, it seems to be far from an efficient flight condition. In fact, a big part of the wing is not producing adequate suction. It should be noted that the analysed geometries are the not optimized baseline and the structural deformation is not considered. In Sec. 2.3.3.4 the same comparison is presented letting the structure to deform under the load.

Figure 2.23 shows the lift coefficient distributions of the three wing systems. It can be seen that the BSW and FSW $C_L$ distributions are very different while the NSW generally lies between the two. In particular, the FSW has higher local lift coefficient inboard while the BSW outboard. The latter condition is dangerous since wing tip stall may occur, causing a loss of manoeuvrability. The first condition is then safer. Aircraft manufacturer solve this problem by twisting the wing in such a way that the wing tip results to be unloaded while the root more loaded. This is called wing *washout* and it could provoke an increasing of angle of attack during the off-design conditions (landing/take-off) as described by *Martin Hepperle* (*2008*).

## 2.2 Structure analysis

The structural module *InAirSsi* (*Internal Aircraft Structural sizing*) was developed by *I. Ghazlane* (*2012*) during her PhD thesis. The work sought to obtain the best compromises between wing aerodynamics and structures for optimal performance. Thus, for a given wing the sizing of the different structural components for weight minimization was needed.

Powerful, commercial tools for structural analysis, with fully featured finite elements models, exist and could be coupled with the ONERA CFD software *elsA*, but at the cost of high complexity in the preprocessing and actual use. The approach used by *I. Ghazlane* and adopted by the author derives from the idea that a tool used in conceptual and/or preliminary design needs to converge in a short time to a feasible solution. It is also not desirable to have complex set-up processes in early design phases where the reduction of time/cost is a target. For these reasons, an Euler-Bernoulli beam model was chosen to compute the wing structure behavior. This model is a unidimensional model based on the assumption that the cross-sectional beam plane does not deform. Although this is a low-fidelity model, it is able to provide a valuable insight into the behavior of slender structures. However, the limitation of this approach are considered as discussed below.

In the following sections the structural module InAirSsi will be introduced and its capabilities presented, after an overview of the beam model theory. Validation of the structural module for simple geometry against theory is also provided.

### 2.2.1 Euler-Bernoulli beam model

The InAirSsi (*I. Ghazlane*, *2012*) wing model is a cantilevered Euler-Bernoulli beam with linear coupled bending and twist motions. Several aeronautical structures such as wings and fuselages can be treated as thin-walled beams since, by definition, a *beam* has one of the dimensions much larger than the other two. Solid mechanics *beam theory* plays an important role in structure analysis it enables simple yet accurate results to be obtained. Beam models are often used at a preliminary design stage because they provide value insight into the behaviour of the structure (*O.A. Bauchau and J.I. Craig, 2009)*.

The theory of Euler and Bernoulli (*O.A. Bauchau and J.I. Craig, 2009; E. Carrera, G. Giunta, M. Petrolo, 2011*) makes the fundamental assumption that the cross-section of the beam is infinitely rigid in its own plane. Thus, no deformations occur in the plane of the cross-section, and only in-plane displacements are allowed. Consequently, during deformation the cross-section is assumed to remain plane and normal to the deformed beam axis.

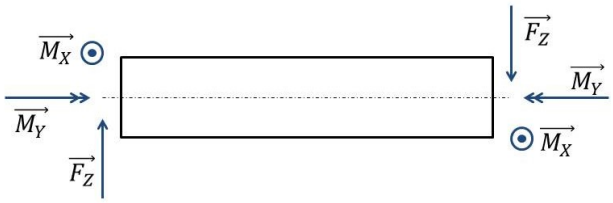


**Figure 2.24: Euler beam model loads**

The wing beam model is usually subject to the following loads, Figure 2.27:

- Vertical force $F_z$
- Flexural moment $M_x$
- Torsional moment $M_y$

As consequence, *bending*, *torsional* and *shear* stresses are considered.

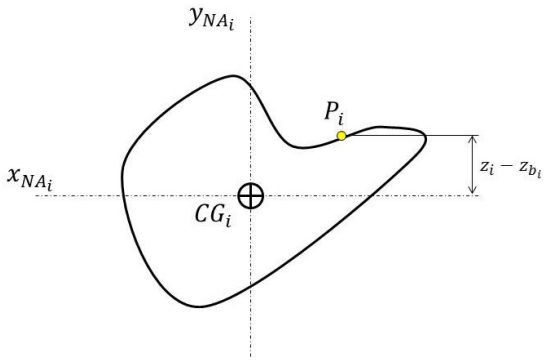


**Figure 2.25: Section "*i*" of the beam model**

Assuming that the *x* and the *z* axes are the principal axes of the beam section and no axial force is acting on the structure (Figure 2.25), the general expression of the *normal stress* due to bending is:

$$\sigma_{xx_i}(y) = \frac{M_{x_i}(z_i - z_{b_i})}{I_{xx_i}} \tag{4.20}$$

where $I_{xx_i}$ is the moment of inertia about the y-axis of the cross-section $i$, $(z_i - z_{b_i})$ the distance of a point on the cross-section of vertical coordinate $z_i$ to the neutral axes and $M_{x_i}$ is the bending moment. In particular, for a wing beam model, the moment $M_{x_i}$ is the integrated bending moment of all aerodynamic forces acting on the wing from the tip to the current cross-section $i$ and it is expressed by:

$$M_{x_i} = \sum_{k=tip}^{i} \left( M_{x_k} + \overrightarrow{P_i P_k} \wedge \vec{F} \right) \tag{2.21}$$

where $M_{x_k}$ represents punctual bending moments and diffused bending moments integrated from the cross-section $i$ and the beam tip $\int_{s=i}^{tip} m_x(s)ds$, $\overrightarrow{P_i P_k} \wedge \vec{F}$ represents bending moments due to punctual forces and bending moments due to diffused forces integrated from the cross-section $i$ and the beam tip $\int_{s=i}^{tip} [f(s) * (tip - s)]ds$. The wing is assumed to behave in torsion like a thin-walled closed section beam. Such an approach has been used by *Bach et al.* (*2016*) for stacking sequence optimization and aero-elastic tailoring of forward-swept composite wings. Assuming a constant thickness of the cross-section $i$, the *shear stress* due to torsion is computed by:

$$\tau = \frac{M_{y_i}}{2A_i t} \tag{2.22}$$

where $t$ is the thickness and $M_{y_i}$ is the torsional moment. For the wing beam model $M_{y_i}$ is the integrated torsional moment of all aerodynamic forces acting on the wing from the tip to the current cross-section $i$. For detailed proof of the abovementioned mechanical properties of the beam model, refer to (*D.J. Peery, 1950*).

### 2.2.2 InAirSsi structural model

In this section, the structural module InAirSsi is introduced and the major capabilities explained. For an exhaustive presentation of the module refer to (*I. Ghazlane, 2012*).

The capabilities of the structural model InAirSsi can be summarized as:

- Structural modelling capability;

- Weight computation capability;
- Load application capability;
- Material stress computation capability;
- Sensitivity analysis capability;
- Gradient-based optimization capability.

InAirSsi input-output system can be summarized as (Table 2.8):

| InAirSsi input | InAirSsi output |
|---|---|
| • Wing CFD surface mesh<br>• Structural parameters<br>• Material properties<br>• Sizing load | • Wing-box structural model<br>• Analytical beam model<br>• Flexibility matrix<br>• Structural weight<br>• Material stresses<br>• Sensitivities |

**Table 2.8: InAirSsi Input-Output system**

Giving the CFD surface mesh to the structural module, by defining the spanwise control sections ($k$) and setting the structural parameters ($\alpha_{struc}$) of them the structural model of the wing come up automatically. The module generates only the primary structure of the wing. The wing structure is assumed to be composed of two spars which are joined by a strengthened skin, forming the so-called *torsion box*. The spars are major structural elements of the wing and the most heavily loaded structure of an aircraft. They usually consist in a beam with an *I-shape* cross section that is composed of a vertical part, the web and a horizontal one, the cap. The role of the spar caps is mainly to resist bending loads and axial loads, while also increasing the torsional resistance. The skin, as part of the torsion box, takes up the torsional loads together with the spar web. Moreover, the skin links the caps of the front spar to the caps of the rear spar, helps in resisting bending and transmits the aerodynamic loads to the structure. For that reason, in InAirSsi the skin and the spar caps are lumped into a single effective element, forming a unique box with the spar webs. The spanwise wing box sections remain rigid within their own plane.

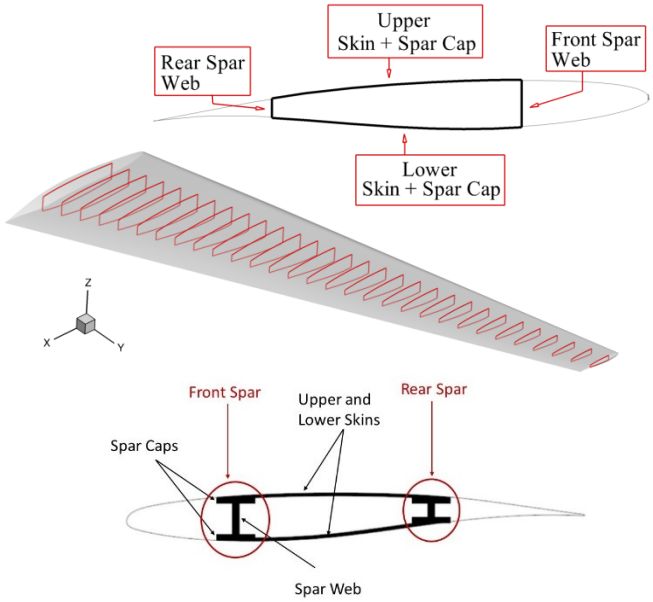


**Figure 2.26: Internal wing structure and wing box section**

Referring to Figure 2.26, the components of the wing box are defined by the following geometrical structural parameters:

- Thickness of the front spar web: $t_{fs}$
- Thickness of the rear spar web: $t_{rs}$
- Position of the front spar web: $p_{fs}$
- Position of the rear spar web: $p_{rs}$
- Thickness of the lower surface spar cap: $t_{lc}$
- Thickness of the upper surface spar cap: $t_{uc}$
- Thickness of the lower surface skin: $t_{ls}$
- Thickness of the upper surface skin: $t_{us}$

Thus, the structural parameters $\alpha_{struct}$ are equal to $8 * k$, with $k$ as number of spanwise control sections. At each control section, each of the eight inputs are given as percentage of the local airfoil thickness (for the upper and lower thicknesses) or a percentage of the local chord (for the front and rear thicknesses). These values are then interpolated in the spanwise direction at the *beam discretization nodes*. From this, mechanical properties as bending stiffness *EI*, torsion stiffness *GJ* and the *centroid* are computed. From the centroid positions, the *elastic axis* is then known. Only isotropic materials are considered in the analysis.

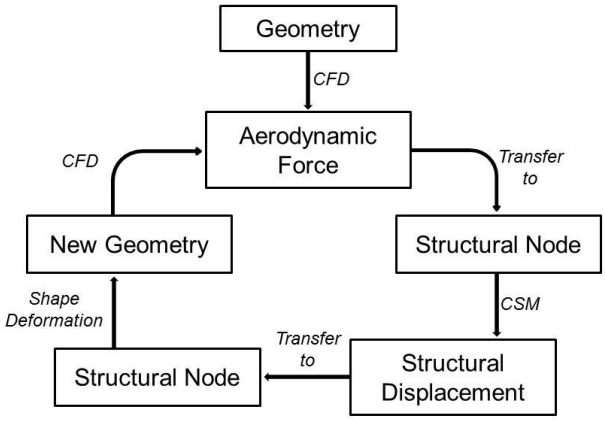


**Figure 2.27: Aero-elastic coupling flowchart**

The aero-elastic coupling passes through the nodes of the discretized beam model. These nodes are displacement and load nodes at the same time. The nodes are the points where aerodynamic forces are transferred to the wing structure, and where the structural displacements are transferred back into the aerodynamic mesh during the aero-elastic coupling (Figure 2.27). Thus, once the aerodynamic forces are transferred to the structural nodes, the displacement of them are computed by using the flexibility matrix. Then, the node displacements are converted to CFD mesh deformation and the loop could continue with a new aerodynamic force estimation. In order to avoid very big structural deformation, mostly at the beginning of load applications on the *jig-shape*, then to reach the coupling convergence, a relaxation factor of 0.7 is applied to the aerodynamic load. In that way, the structure deformation is kept under control even for very light structures or very loaded ones. This topic is better addressed in Sec. 2.3.1. Once the structure is loaded, by using the equations of Sec. 2.2.1 the stress level of each element is computed. A mechanical constraint during the weight minimization procedure can be applied in order to avoid material elastic limit being exceeded for the wing box structural elements. The wing structural weight is calculated by computing the elements volume between adjacent cross-sections, multiplying it for the constant material density (isotropic materials) and then summing them together.

InAirSsi is a structural module developed for adjoint-based optimization (Chapter 3) and it computes the structural weight, the stress levels and the sensitivity of the latter two with respect to the structural variables. Details of the sensitivity calculation are presented in Sec 3.3.1.

#### 2.2.2.1 Validation of the structural module

The validation of the sensitivity of the weight and the stress level with respect to the structural variable is presented by *I. Ghazlane* (*2012*), as well as the calculation of the total integrated aerodynamic forces along the wing spanwise. What was not addressed is the validation of the stress level of the structure subjected to specific loads. Below, the comparison between the InAirSsi stress levels and theoretical ones is analyzed.

A very regular square section beam was generated in order to have simple and intuitive results for the comparison. Figure 2.28 and 2.29 show respectively the geometry (used to give the internal structure) and the internal test case structure generated by the structural module.

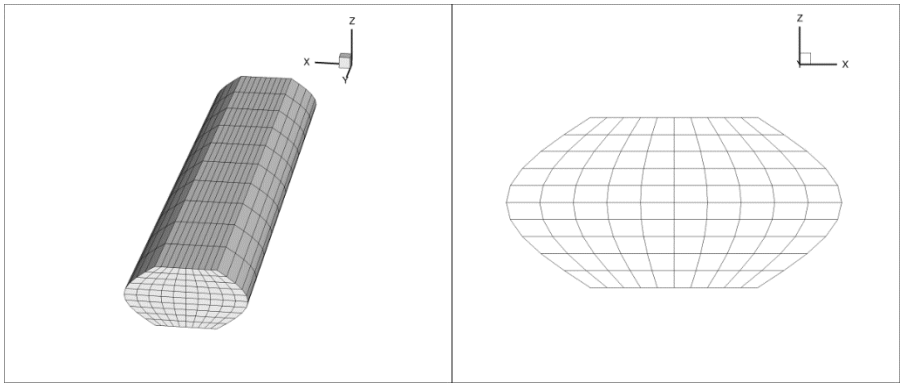


**Figure 2.28: Test case geometry**

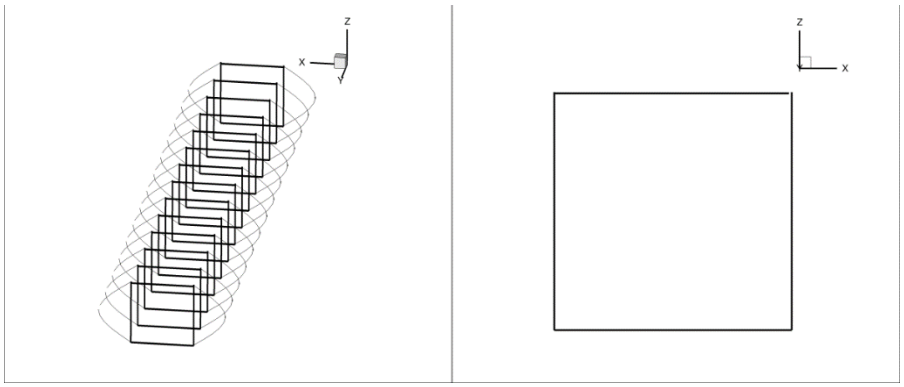


**Figure 2.29: Test case internal structure**

The beam is *1m x 1m x 10m* along the *x*, *z* and *y* axis respectively. As described above, each one of the structural variable inputs represent a percentage of the local airfoil thickness (for the upper and lower thicknesses) or a percentage of the local chord (for the front and rear thicknesses). The test case is characterized by *2m* local chord and *1m* local wing thickness, and *1.5%* is chosen as input for each one of the structural variables, apart for the front and rear spar position that are

respectively at *25%* and *75%* of the local chord. It is important to remember that the structural variables are given as percentage of the local airfoil thickness (for the upper and lower thicknesses) or a percentage of the local chord (for the front and rear thicknesses). Table 2.9 summarizes the structural elements thicknesses.

| | | **Skins** | **Caps** | **Spars** |
|---|---|---|---|---|
| Percentage | [%] | 1.5 | 1.5 | 1.5 |
| Thickness | [m] | 0.015 | 0.015 | 0.03 |

**Table 2.9: Size of the test case structural elements**

Two load cases were chosen: *distributed constant vertical load* $q$ and *tip torsional moment* $M_t$ (Figure 2.30).

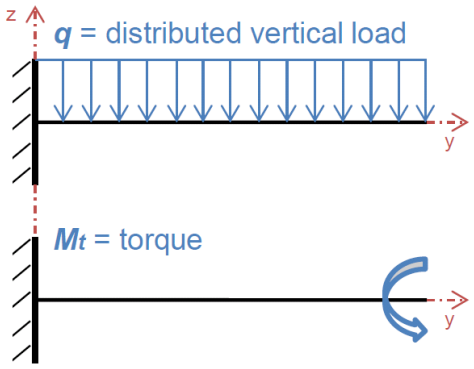


**Figure 2.30: Test case loads**

The first load results in a bending stress ($\sigma$) while keeping the shear ($\tau$) equal to zero. Conversely, the second load case induces shear stress only. Eq. 2.20 and 2.22 describe the analytical solution for the two cases. The validation is made by comparing the stress level of the *extrados elements* (skin + cap thicknesses) along the beam.

Table 2.10 gives the results of the theoretical calculation and the computational model estimation of the test case cross-section inertia $I_{xx_i}$ (that is the same all along the spanwise). The error, given in percentage of the theoretical value of the inertia, is around *1.1%*.

| | Theory | InAirSsi |
|---|---|---|
| Inertia $I_{xx_i}$ [m$^4$] | 0.018271 | 0.01807 |

**Table 2.10: Inertia of the test case cross-section**

The $M_x(y)$ changes along the y-direction with the Eq. 2.21:

$$M_x(y) = {}^{q}/_{2} * (span - y)^2 = {}^{q}/_{2} * (10 - y)^2 \tag{2.23}$$

So, for $q = 200000\ {}^{N}/_{m}$ the theoretical bending stress in the extrados will be:

$$\sigma_{extrados}(y) = \frac{100000 * (10 - y)^2}{0.018271} * 0.5 \tag{2.24}$$

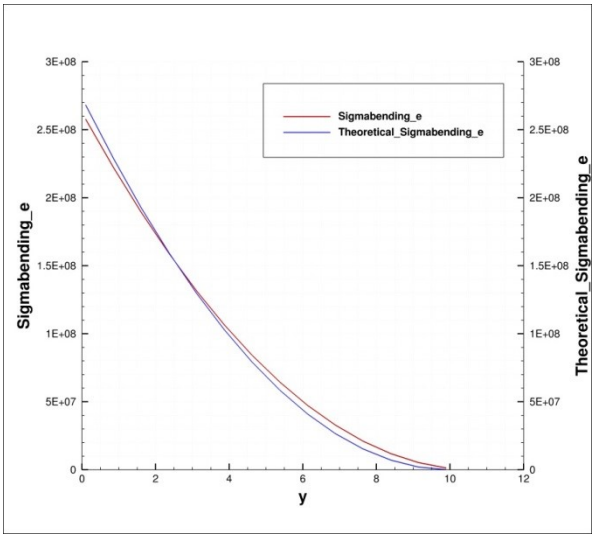


**Figure 2.31: Comparison between the theoretical and InAirSsi bending stress**

Figure 2.31 shows the trend of the normal stress due to the distributed bending moment and the two evaluations differ of *3.8%* maximum. For the second load case, a torsional moment of $M_t = 2000000\ {}^{N}/_{m}$ is taken, for which the theoretical shear stress is constant and it is expressed by:

$$\tau_{extrados} = \frac{M_t}{2tA} = 266666667\ \left[{}^{N}/_{m^2}\right] \tag{2.25}$$

In this case, the InAirSsi torsional stress differ by 2% maximum from the theoretical one.

These discrepancies may come from the imperfect definition of the structural model automatically generated from a surface mesh model. For preliminary design purpose, the capability

to automatically generate a structural model is more important than the minor error in inertia and stress level calculation. For this reason, the reliability of the structural module for stress level computation is appropriate for the purpose of the study.

## 2.3 Aero-elastic coupling

Reliable aerodynamic design cannot exclude elastic deformation under loads. Since that, the aero-elastic module of the CFD software *elsA* named *elsA BAG* is used. This module was developed by *M. Marcelet* (*2008*) during her PhD, and it was mainly developed for aero-elastic gradient computation with adjoint method (Chapter 3). In the following sections the static aero-elastic investigation is presented, and the particular static divergence feature of the FSW architecture is addressed. Finally, the importance of considering elastic deformation within aerodynamic investigation is showed.

### 2.3.1 Fluid-structure interaction method

Various approaches to Fluid-Structure interactions can be considered, ranging from one-way coupling to two-way coupling, up to fully coupled methods based on monolithic codes. Considering the importance of FSI in the design of light and robust structures, industry needs an access to efficient and accurate tools for FSI and aero-elastic prediction (*F. Debrabandere, B. Tartinville, C. Hirsch, 2011*). The approach used here is a two-way coupling: once the Euler flow is computed based on the unloaded shape, the aerodynamic load is transferred to the beam nodes and the displacement is obtained. The new shape will be the input for the further CFD iterations, going through this process till the aero-elastic equilibrium is reached. Thus, the equilibrium position is reached after a number of iterations where the fluid and the structure exchange aerodynamic loads and structural displacement. During the aero-elastic coupling, the structure is assumed not to store any kinetic energy (*M. Marcelet*, *2008*).

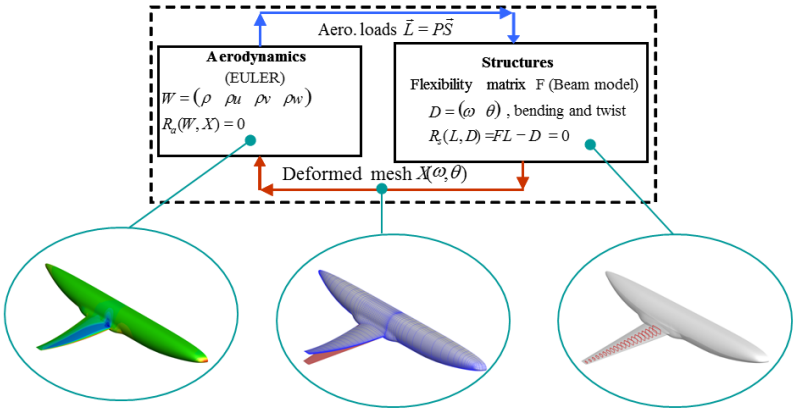


**Figure 2.32: Aero-elastic coupling**

In summary: the aero-elastic equilibrium is an iterative procedure performed through the following sequence of action (Figure 2.32):

- loads transfer from the aerodynamic mesh to the structural one;
- beam displacement computation by means of *flexibility matrix*;
- displacements transfer from the structural mesh to the aerodynamic one;
- load computation via solving the flow equation for the new aerodynamic mesh

In the next sections, the loads and displacements transfer method is introduced, as well as the displacements computation using the flexibility matrix approach. For a more exhaustive analysis refers to *M. Marcelet*, *(2008); R.L. Bisplinghoff, H. Ashley, R.L. Halfman, (1996)*.

#### 2.3.1.1 Aerodynamic load transfer to the structural nodes

At each coupling iteration of the aero-elastic procedure, the aerodynamic loads are extracted from the aerodynamic mesh and applied to the beam nodes $i$ $(1 \leq i \leq n_b)$ with which the structure is discretized. The aerodynamic loads extraction is performed by computing equivalent loads to be transfer to the nodes, and the physical properties of the system have to be ensured during the procedure: *load equilibrium* and *conservation of the energy*. The first condition is ensured if the aerodynamic loads computed on the surface aerodynamic mesh are equal to the loads applied on the structural mesh. The conservation of the energy in ensured if the energy produced (absorbed) by the structure is equal to the energy absorbed (produced) by the fluid. The energy conservation is desirable also when static cases are considered because it ensures accurate, robust and reliable

results anytime that the interpolation of forces and displacements from/to the aerodynamic and structural mesh can be inaccurate due to coarse meshes. *Farhat et al.* (*1997*, *1998*) demonstrate that the procedure that is briefly presented in this section ensures the abovementioned physical properties.

$\overrightarrow{F_i}$ and $\overrightarrow{M_i}$ are, respectively, the aerodynamic force and moment at the *i*$^{th}$ beam node $P_i$. Considering Euler (inviscid) equations to solve the fluid behavior, the beam loads are given by:

$$\overrightarrow{F_i} = \sum_{l=1}^{n_{surf}^I} S_l^i (p_l - p_\infty) \overrightarrow{n_l} \tag{2.26}$$

$$\overrightarrow{M_i} = \sum_{l=1}^{n_{surf}^I} \overrightarrow{P_i G_l^i} \wedge S_l^i (p_l - p_\infty) \overrightarrow{n_l} \tag{2.27}$$

where $n_{surf}^I$ is the number of aerodynamic surface mesh cells within the influence zone $I_i$ of the beam node $P_i$ (Figure 2.33). $S_l^i$ is the surface intersection of the mesh cell and the influence zone, while $G_l^i$ is the barycenter of the intersection.

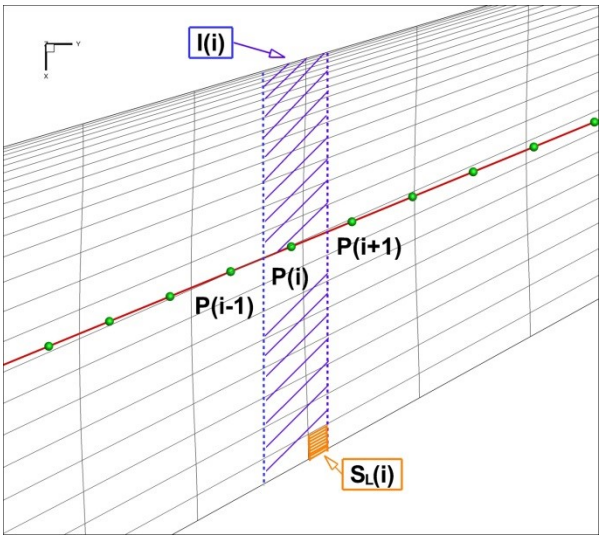


**Figure 2.33: Load transfer to beam nodes**

Once the aerodynamic loads are transferred to the beam nodes, the deformation has to be evaluated.

#### 2.3.1.2 Flexibility matrix approach

In order to calculate the structural equilibrium under the aerodynamic forces, the *flexibility matrix approach* (*R.L. Bisplinghoff, H. Ashley, R.L. Halfman, 1996*) was chosen. According to the principle of superposition for a linear elastic structure, the total displacements of a given point of the structure is equal to the sum of the displacement induced at this point by the loads applied individually at any structural point. For a discrete number of forces, any displacement can thus be expressed as:

$$D_i = \sum_{j=1}^{n} F_{ij} L_j \tag{2.28}$$

where $D_i$ is the displacement of the *i*th structural node due to the load $L_j$ that results to be applied to the *j*th node. $F_{ij}$ is the coefficient that transforms the *j-force* into *i-displacement*. The associated linear system is:

$$D = FL \tag{2.29}$$

with *F* the *Flexibility Matrix*. In general, with $(\omega_x, \omega_y, \omega_z)$ is defined the linear field deflection along the three axes, the vector $(\theta_x, \theta_y, \theta_z)$ defines the angular field deflection, $(F_x, F_y, F_z)$ and $(M_x, M_y, M_z)$ defines the forces and moments acting on the structure. Since the Euler-Bernoulli beam model is chosen, only $\omega_z$ and $\theta_y$ are possible and only the loads $F_z$, $M_x$, $M_y$ are taken into account. The resulting flexible matrix will be so defined:

$$F = \begin{bmatrix} [F^{zz}]_{(1\le i,j\le n_b)} & [F^{z\theta_y}]_{(1\le i,j\le n_b)} & [F^{z\theta_x}]_{(1\le i,j\le n_b)} \\ [F^{\theta_y z}]_{(1\le i,j\le n_b)} & [F^{\theta_y\theta_y}]_{(1\le i,j\le n_b)} & [F^{\theta_y\theta_x}]_{(1\le i,j\le n_b)} \end{bmatrix} \tag{2.30}$$

where $n_b$ is the amount of beam nodes used for the structure discretization and:

- the coefficient $F_{ij}^{zz}$ is the linear vertical deflection $\omega_z$ at the *i*th node due to unit vertical force $F_z$ applied at the *j*th node;
- the coefficient $F_{ij}^{z\theta_y}$ is the linear vertical deflection $\omega_z$ at the *i*th node due to unit moment $M_y$ applied at the *j*th node;

- the coefficient $F_{ij}^{z\theta_x}$ is the linear vertical deflection $\omega_z$ at the *i*th node due to unit moment $M_x$ applied at the *j*th node;
- the coefficient $F_{ij}^{\theta_y z}$ is the angular deflection $\theta_y$ at the *i*th node due to unit vertical force $F_z$ applied at the *j*th node;
- the coefficient $F_{ij}^{\theta_y\theta_y}$ is the angular deflection $\theta_y$ at the *i*th node due to unit moment $M_y$ applied at the *j*th node;
- the coefficient $F_{ij}^{\theta_y\theta_x}$ is the angular deflection $\theta_y$ at the *i*th node due to unit moment $M_x$ applied at the *j*th node.

The computation of the flexibility matrix, as well as the analysis of the method to transfer the structural deformation back to the fluid mesh are briefly addressed in the following sections.

#### 2.3.1.3 Calculation of the flexibility matrix for arbitrary structure

Unless a rectilinear beam is considered, the structure is approximate by several rectilinear small elements of structure. Indicated $P_i$ for the *i*th beam node, the beam section between two adjacent beam nodes $P_{i-1}$ and $P_i$ is then considered rectilinear and a local reference system $(X_i, Y_i, Z_i)$ is defined: the axis $Y_i$ corresponds to the local direction $P_{i-1}P_i$, the axis $Z_i$ is the closes one to the ascending vertical direction ***z*** and the axis $X_i$ completes the system (Figure 2.34).

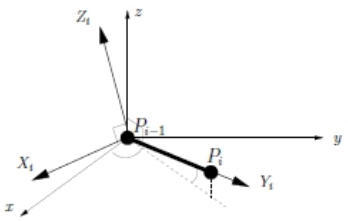


**Figure 2.34: Local reference system**

The aerodynamic loads applied to the beam node for which the displacement will be calculated are projected to the new local reference system. Once the displacement is computed, it will be projected back to the global reference system.

Assuming that the deformation is known at displacement node $P_{i-1}$, the induced deformation of the section $P_{i-1}P_i$ can be computed. The load at the beam point $P_j$, expressed in the global coordinate system (*x*, *y*, *z*), are:

$$\begin{pmatrix} 0 & M_{x_j} \\ 0 & M_{y_j} \\ F_{z_j} & O \end{pmatrix}_{(x,y,z)} \tag{2.31}$$

The moment induced at $P_i$ by the loading at $P_j$, expressed in the global coordinate system, is:

$$\left(\vec{M}(P_i)\right)_{(x,y,z)} = \vec{M}(P_j) + \overrightarrow{P_iP_j} \wedge F_{z_j}\vec{z} = M_{x_j}\vec{x} + M_{y_j}\vec{y} + \overrightarrow{P_iP_j} \wedge F_{z_j}\vec{z} \tag{2.32}$$

Projecting $\left(\vec{M}(P_i)\right)_{(x,y,z)}$ in the local coordinate system associated to the beam section $P_{i-1}P_i$:

$$\vec{M}(P_i) = M_{X_i}\overrightarrow{X_\iota} + M_{Y_i}\overrightarrow{Y_\iota} + M_{Z_i}\overrightarrow{Z_\iota} \tag{2.33}$$

With the assumption of the Euler-Bernoulli beam model, only flexural moment $M_{X_i}$ and torsional moment $M_{Y_i}$ at the point $P_i$ are considered for the deformation analysis. The structural deformation, expressed in the local coordinate system is the combination of $\omega_{Z_i}$ the linear deflection according to the axis $Z_i$, $\theta_{X_i}$ the angular deflection according to the axis $X_i$ and $\theta_{Y_i}$ the angular deflection according to the axis $Y_i$. *EI* and *GJ* are the bending and the torsional stiffness, if the loaded point $P_j$ is located beyond the point $P_i$ (it means at a location closer to the wing tip), the induced deformation at $P_i$ by the load is:

$$\left(\theta_{X_i}\right)_i = \left(\theta_{X_i}\right)_{i-1} + \frac{1}{2}\left(\frac{\left(M_{X_i}\right)_i}{EI_i} + \frac{\left(M_{X_i}\right)_{i-1}}{EI_{i-1}}\right)\|P_{i-1}P_i\| \tag{2.34}$$

$$\left(\theta_{Y_i}\right)_i = \left(\theta_{Y_i}\right)_{i-1} + \frac{1}{2}\left(\frac{\left(M_{Y_i}\right)_i}{GJ_i} + \frac{\left(M_{Y_i}\right)_{i-1}}{GJ_{i-1}}\right)\|P_{i-1}P_i\| \tag{2.35}$$

$$\left(\omega_{Z_i}\right)_i = \left(\omega_{Z_i}\right)_{i-1} + \frac{1}{2}\left(\left(\theta_{X_i}\right)_i + \left(\theta_{X_i}\right)_{i-1}\right)\|P_{i-1}P_i\| \tag{2.36}$$

If the loaded point $P_j$ is located closer to the wing root than the point $P_i$:

$$\left(\theta_{X_i}\right)_i = \left(\theta_{X_i}\right)_j \tag{2.37}$$

$$\left(\theta_{Y_i}\right)_i = \left(\theta_{Y_i}\right)_j \tag{2.38}$$

$$\left(\omega_{Z_i}\right)_i = \left(\omega_{Z_i}\right)_j - \left(\theta_{X_i}\right)_j \|P_{i-1}P_i\| \tag{2.39}$$

The induced deformation at $P_i$ follows different equations depending on the location of the loaded point $P_j$ because the considered beam element $P_{i-1}P_i$ results to be loaded (internal effort not null) or not loaded (null internal efforts) respectively if $P_j$ is beyond ($i \leq j$) or before ($i > j$) $P_i$.

As described above, the deformations $\left(\theta_{X_i}\right)_i$, $\left(\theta_{Y_i}\right)_i$ and $\left(\omega_{Z_i}\right)_i$ are than projected in the global coordinate system (*x*, *y*, *z*). Once the flexibility matrix of the structure is computed, the vector *D* of the displacements is easily found by the Eq. 2.29.

#### 2.3.1.4 Structural displacements transfer to the aerodynamic mesh

The previous section introduces the means to compute the beam node displacements. In this section the means to transfer these displacements to the aerodynamic mesh nodes are introduced. Identifying with $\overrightarrow{\chi_{rig_j}}$ the position of an aerodynamic mesh node corresponding to the *jig-shape* (undeformed), $\overrightarrow{\chi_j}$ the position of the same node at an iteration of the aero-elastic coupling and with $\overrightarrow{\chi'_{b_j}}$ the projection of $\overrightarrow{\chi_j}$ on the structural mesh, it is possible to write the following relation:

$$\overrightarrow{\chi_j} = \overrightarrow{\chi_{rig_j}} + \omega_z\left(\chi'_{b_j}\right)\vec{z} + \overrightarrow{\chi_{rig_j}\chi'_{b_j}} \wedge \vec{\theta}\left(\chi'_{b_j}\right) \tag{2.40}$$

where $\omega_z\left(\chi'_{b_j}\right)$ and $\vec{\theta}\left(\chi'_{b_j}\right)$ are, respectively, the linear and the angular deflection of the projection. The displacement field is available for the structural mesh nodes, thus the structural deformation for the projection $\chi'_{b_j}$ is linearly interpolated from the deformation values at the neighboring structural mesh points.

Then, the flow field around the new aerodynamic mesh will be solved and the procedure will iteratively continue till convergence.

### 2.3.2 Convergence of the coupled analysis

During the study, it was experienced that the convergence of a fluid-structure coupled analysis was subjected to two major problems arising from:

- deformation of the geometry and the mesh;
- consistent setting of the coupling parameters of the computation.

The two abovementioned cases lead both to incorrect results of different types. In the first case, CFD does not converge. In the other case, a miss-setting of the coupling parameters can end up with unreliable results.

The first problem can occur when the structure is not stiff enough to support the aerodynamic load, thus significant deformation is observed. In that case, the convergence failure might be due to two reasons:

- large deformation of the mesh cells;
- high local angle of attack at the tip for FSW configuration.

Due to the lift, the wing is naturally bent. It is evident that the wing deformation has to be "propagated" in some way to avoid large cell distortion that can compromise the quality and the convergence of the computation. For that reason, during the fluid-structure coupling a portion of the mesh volume around the wing follows rigidly the wing mesh skin deformation. Outside this rigid volume, the deformation field is analytically computed section by section perpendicular to the wing span and it depends on four parameters: a rotation angle generated by the wing twist, a translation vector defined by $\Delta$x and $\Delta$z generated by the wing bending and an expansion factor. Those four factors at a given point $P$ are used to compute the deformed point $P'$, as explained by *A. Dumont et al.* (*2011*). Although mesh distortion occurs between the deformed and undeformed mesh volumes, it is damped far away from the body, where the size of the cells is large enough to allow a slow transition without deteriorating the mesh quality. Figure 2.35 compares an undeformed and deformed portion of the volume CFD mesh.

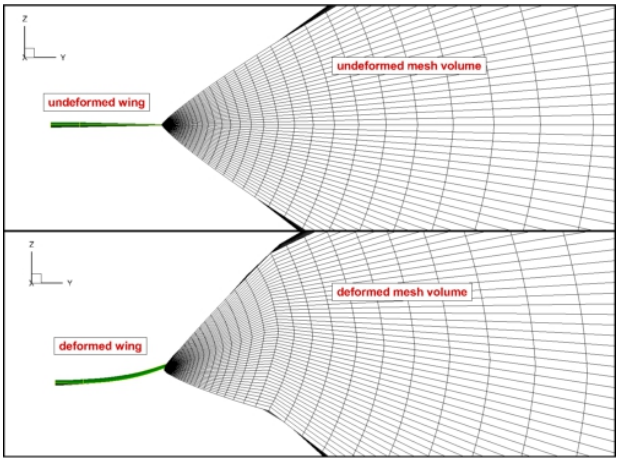


**Figure 2.35: Undeformed (above) and deformed (below) volume mesh**

Usually, regardless of wing configuration the bending deformation is linked to the local angle of attack that wing sections observe. When an FSW configuration is considered, the wing bending induces an increment of the local angle of attack. It is easy to understand that, if the wing ends up with a significant bending deformation the local angle of attack of the outboard wing (mostly for the wing tip) could go beyond the angle for which the Euler formulation is reliable, as described in Sec. 2.1.3.2. Thus, the wing structure should be stiff enough to avoid such problem. The consequences of this aero-structural limit are presented in Chapter 3 while the structural optimization is introduced.

As described above, the setting of the coupling parameters of an aero-elastic computation is very important in order to get reliable aerodynamic and structural results. There are 4 main parameters that play a role in the coupling:

- $n_{iter\_ini}$: number of initial CFD iterations, before the first coupling;
- $n_c$: number of coupled iterations during the aero-elastic computation;
- $n_{step}$: number of CFD iterations between a coupling and another;
- $n_{iter\_final}$: number of final CFD iterations, after the last coupling.

The first parameter could be seen as the starting point of the computation. So that, the initial solution has to be developed enough to avoid misleading aerodynamic loads on the flexible structure. The number of coupled iterations describes how many times the information will be exchanged between the CFD and the elastic solution. The less stiff the wing structure is, the more coupled iterations have to be performed to ensure the convergence to a reliable solution. $n_{step}$ defines how developed

the aerodynamic solution is after a shape deformation. Finally, the last parameter has to ensure a fully converged aerodynamic solution. By experience and experimentation with the simulation code, usually the following rules have to be respected:

- $n_{iter\_ini}$ has to be large enough to avoid a poor quality first aerodynamic evaluation;
- $n_c$ strongly depends on how stiff the structure is. Few couplings are enough for very stiff structure (5 – 7 to give an order of magnitude) while for thin structure the information has to be exchanged more times (around 15 times);
- usually, for a given structure the more couplings there are, the less $n_{step}$ CFD iteration are needed. Since after a shape deformation the aerodynamic computation is initialized from the previous one, big change in shape (typical for thin structure) needs larger $n_{step}$ to avoid very bad aerodynamic representation;
- $n_{iter\_final}$ has to ensure a very good analysis convergence (4-5 order of magnitude of residuals), mostly if gradient computation for optimization are requested.

### 2.3.3 Aero-elastic investigation

In the previous sections, the fluid-structure interaction method was introduced. In the following part, the aero-elastic investigations are presented. In particular, the problem of the static divergence for the forward-swept wing architecture is underlined, together with the comparison between the isolated wing and wing-body configuration. Moreover, the differences between the elastic approach with respect to the rigid one are put in evidence and comparison among backward-swept, forward-swept and zero-sweep wings is presented.

#### 2.3.3.1 Static divergence of the Forward Swept Wing architecture

The forward swept wing architecture suffers divergence problem. As described in Chapter 3, during the optimization of the wing structure, no explicit constraint concerning aero-elastic divergence is implemented. It will be shown that due to the strategy adopted for the consistent structural optimization, there is very small possibility that divergence can occurs, thus constraint is not needed.

If the wing structure is not stiff enough the aero-elastic computation will detect divergence. Since only steady simulations are considered, what it is possible to simulate is the *static* divergence, while the *dynamic* one is not computed. Thus, dynamic phenomena are not considered in the investigation. It is important to remember that the preliminary design phase is considered, and static divergence investigation results are already quite advanced compared to current preliminary design analysis. Figure 2.36 shows the wing deformation for a wing structure which is not stiff enough for the considered flight condition. The illustrated deformation does not represent the real wing deformation of a converged aero-elastic analysis since in that condition the CFD simulation cannot converge. It is the deformation computed just before that the analysis is unable to converge.

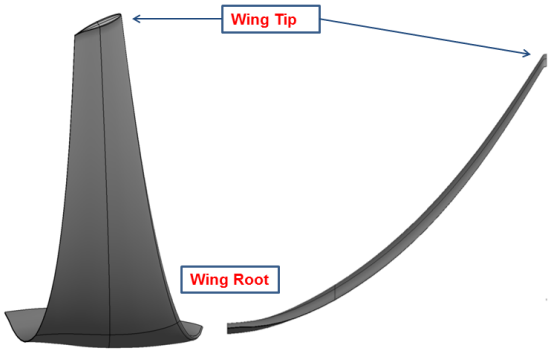


**Figure 2.36: Diverged forward-swept wing**

Figure 2.37 shows the wing shape in aero-elastic equilibrium. The structure is stiff enough to resist divergence due to the positive coupling between bending and twist which characterizes the considered wing architecture.

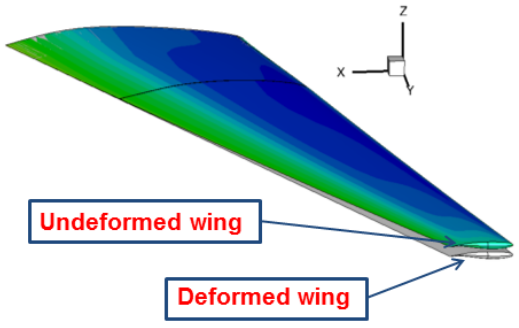


**Figure 2.37: Converged deformed wing**

### 2.3.3.2 Isolated wing vs wing-body configuration

In Sec. 2.1.4.3 the differences of the flow field around the rigid wing for the isolated wing and for the wing-body configurations are presented. It was shown how the presence of the fuselage can induce strong flow acceleration on the in-board wing zone. By analysing the aero-elastic behaviour of the wing, the importance of considering the wing-body configuration is shown once more. Figure 2.38 shows the wing deformations with and without the fuselage present.

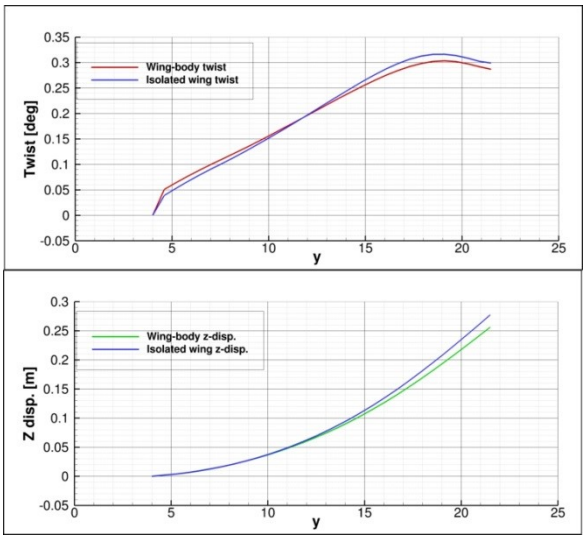


**Figure 2.38: Deformation of the isolated wing and the wing-body configuration**

It is possible to see that both twist deformation and Z-deflection change if the wing-body interactions are considered. It is important to notice that the comparison was made by considering a stiff structure, while after a structural optimization process (Chapter 3) a more flexible wing is present. The less the structure is stiff, the greater the fuselage influence is even for preliminary design.

### 2.3.3.3 Comparison between rigid and flexible wing

To conclude this section, both isolated wing and wing-body configuration were analysed once considering rigid wing then flexible. In both cases, the consequences of considering the structure deformation are quite similar. The comparison was made for the same flight condition characterized by $M = 0.75, h = 33000ft, C_L = 0.5$. Table 2.11 shows the flight details and aerodynamic coefficients of four investigations: rigid and flexible analysis for isolated wing and wing-fuselage configuration.

| $M = 0.75, h = 33000ft, C_L = 0.5$ | | | | |
|---|---|---|---|---|
| | | **Alpha** | $C_{D_w}$ | $C_{D_i}$ |
| **Rigid Wing** | Isolated Wing | 1.538 | $0.0 \cdot 10^{-4}$ | $99.5 \cdot 10^{-4}$ |
| | Wing-Fuselage | 1.364 | $10.38 \cdot 10^{-4}$ | $84.17 \cdot 10^{-4}$ |
| **Flexible Wing** | Isolated Wing | 1.419 | $0.0 \cdot 10^{-4}$ | $97.7 \cdot 10^{-4}$ |
| | Wing-Fuselage | 1.214 | $8.09 \cdot 10^{-4}$ | $83.51 \cdot 10^{-4}$ |

**Table 2.11: Comparison between rigid and flexible wing**

At first, it is possible to recognize that the lift coefficient is reached for different angle of attack if rigid or flexible wing is considered. Moreover, differences between the drag estimation are observed. It is one of the key points to demonstrate the inconsistency of the rigid polar with respect to the elastic one. This concept will be further examined and explained in Chapter 3.

For the abovementioned reasons, ***elastic wing-body*** configuration was adopted for the forthcoming preliminary design and optimization.

#### 2.3.3.4 Comparison among backward-swept, forward-swept and zero-sweep elastic wings

In Sec. 2.1.4.4 the comparison between backward-swept, forward-swept and zero-sweep rigid wings is presented. There, an analysis of the results for what concerns the lift generation and the wave drag production for the 3 configuration is presented. In this section the same comparison will be presented but letting the structure to deform under the aerodynamic loads, aiming at underlining the importance of structural deformation when aerodynamics loads and features are analysed. The aero-elastic investigations are carried out at iso-$C_L$ ($C_L = 0.635$) and at the same flight conditions. Table 2.12 shows the results.

| $C_L = 0.635$ | Alpha [°] | $C_{dff\_wave}$ | $C_{dff\_ind}$ | Tip twist [°] |
|---|---|---|---|---|
| NSW | 1.415 | $41.88 \cdot 10^{-4}$ | $127.95 \cdot 10^{-4}$ | 0.0 |
| BSW | 2.103 | $56.59 \cdot 10^{-4}$ | $126.60 \cdot 10^{-4}$ | -2.0 |
| FSW | 1.112 | $31.06 \cdot 10^{-4}$ | $126.32 \cdot 10^{-4}$ | 2.9 |

**Table 2.12: Comparison of configurations with different sweep angle**

Comparing those results with the results of the rigid aerodynamic investigation (Table 2.7) it is possible to notice how different the cruise conditions are. In particular, looking at the angle of attack is evident that FSW ended up in decreasing it while BSW in increasing. The NSW configuration almost does not change. Actually, once the structure deforms vertical deflection and wing twist occurs and the tip of the BSW configuration results with a wash-out of -2° while the FSW with a wash-in of 2.9°.

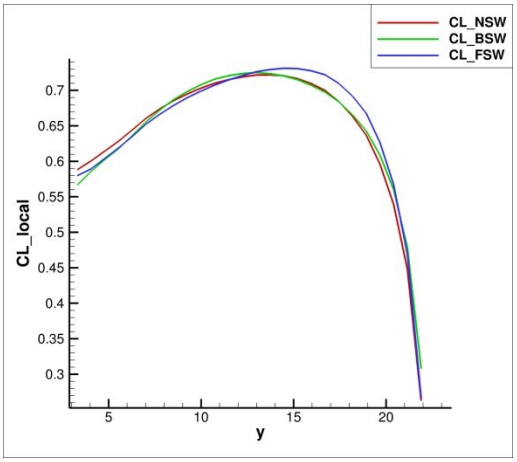


**Figure 2.39: Lift coefficient spanwise distributions for different sweep angles**

Figure 2.39 shows the lift coefficient distribution for the three configurations. It can be seen that the spanwise distribution is almost the same if structural deformation is taken into consideration, while in case of rigid wing the differences are evident (Figure 2.23). Considering a rigid structure, the BSW configuration suffers high local lift coefficient at the tip that imply the need of the washout, with the consequent reduction of the geometrical angle of attack of the whole wing. If elastic structure is considered, the BSW does not seems to suffer such a problem and the disadvantages related to that will disappear.

The importance of considering elastic deformation while solving the flow field around the wing is then underlined once again. Usually, the more rigid the wing is the more decoupled aerodynamics and structure are. It also aligns with conventional aircraft design companies which tend to have monodisciplinary departments working semi-independently of each other rather than a multidisciplinary design workflow, but it looks evident how far from the real global optimum the design could be. The importance of considering structure flexibility during the preliminary design phase is then underlined.

# Chapter 3

# Design Optimization

*In this chapter the optimization techniques are introduced. An overview of the optimization algorithm and the sensitivity analysis is given. The theory of gradient based optimization and the adjoint method for sensitivity computation are presented, while the aerodynamic and structural investigation is presented later. An investigation of the selected design variables to use with respect to the flow condition for a more efficient optimization is shown and the importance of performing aero-elastic optimization rather than rigid aerodynamic one is underlined. Finally, how the sensitivity of the aero-elastic optimization changes depending on the coupling parameters is presented.*

## Contents

## Introduction

*A. Jameson* (*1988*, *1995*) proposed that there are benefits in considering the design problem as a control problem in which the control is the shape of the boundary. Optimization methods have been used to increase the aerodynamic and structural efficiency of aircraft. Since the commercial success of the aircraft depends on cost and timeliness as well as quality, the design process is being reengineered to save cost and time scale. Optimization methods are becoming very attractive in today's competitive environment as they can reduce the design cycle time by automating the design process. Moreover, the optimization techniques give the direct control on performance parameters.

Aerodynamic shape optimization allows the designer to explore the design space to achieve a given objective where the automated aerodynamic design is accomplished by coupling CFD with numerical optimization methods (*T. Mengistu, W. Ghaly, 2003*). *R. M. Hicks et al.* (*1974*) first tackled airfoil design optimization problems. *R. M. Hicks and P. A. Henne* (*1978*) then used a three-dimensional CFD solver to optimize a wing with respect to 11 design variables representing both airfoil shape and the twist distribution. Since then, the approach has been widely used for many aerodynamic design problems including nozzle design (*O. Baysal, M. E. Eleshaky, 1992*), supersonic wing-body design (*J. J. Reuther, A. Jameson, 1995*) and more complex aircraft configurations (*J. J. Reuther et al., 1999*).

Regarding the structural optimization, increasing attention in recent years has been given to the contribution made to design optimization, especially in early stage of aircraft design (*S. A. Falco, A. Rocha de Faria, 2002*). Pioneer applications can be found in the aerospace industry where lightweight structural component are required. *S. Grihon* and *M. Mahé* (*1999*) presented a study where a simplified expression of the operating cost combining cruise drag and wing weight was minimized. Another approach breaks the optimization problem into structural optimization and aerodynamic optimization (*J. H. Garcelon*, *V. Balabanov,1999; J. H. Garcelon, V. Balabanov, J. Sobieski, 1999*).

In the following sections, the optimization techniques are introduced with a focus on gradient-based optimization. Moreover, aerodynamic and structural optimizations are discussed, with

particular attention to setting and results to be used for the later MDO procedure, introduced in Chapter 4.

## 3.1 Optimization Techniques

A range of optimization approaches have been developed, the selection of the most appropriate depends on the kind of physics, number and quality of the design variables, nature of the objectives and constraints. If only one objective needs to be minimized, the problem is called single-objective optimization. If more objectives need to be minimized at the same time, the term multi-objective optimization is used. In general, the optimization problem can be mathematically formulated as:

$$\textit{Minimize: } f(\vec{x}) \tag{3.1}$$

$$\textit{wrt: } \vec{x} \begin{cases} x_1 \\ \dots \\ x_n \end{cases} \tag{3.2}$$

$$\textit{Subject to: } g_i(\vec{x}) \leq 0 \quad j = 1..m \tag{3.3}$$

$$h_k(\vec{x}) = 0 \quad k = 1..l \tag{3.4}$$

$$x_i^l(\vec{x}) \leq x_i \leq x_i^u(\vec{x}) \quad i = 1..n \tag{3.5}$$

The vector $\vec{x}$ is referred to as the vector of design variables. It contains the parameters of the design that can be modified. The function $f(\vec{x})$ is called the objective function. Eq 3.3 and 3.4 are respectively inequality and equality constraints. Eq 3.5 represents the range of the design variables. The constrained optimization problem described by Eq. 3.1 – 3.2 is difficult to solve in a direct way due to the inequality constraints. The constrained formulation can be translated into an unconstrained optimization problem for which the pseudo-objective function $\tilde{f}(\vec{x})$ needs to be minimized (*T. Verstraete, 2014*):

$$\tilde{f}(\vec{x}) = f(\vec{x}) + R \cdot \sum_{j=1}^{m} \delta_j \cdot \left(g_j(\vec{x})\right)^2 \tag{3.6}$$

where $\delta_j = 0$ if $g_j(\vec{x}) \leq 0$, $\delta_j = 1$ if $g_j(\vec{x}) > 0$. A penalty is given to the objective function in case the constraints are not met. The value of $R$ define the weight given to satisfy the constraints.

Many different methods exist to solve the optimization problem and they can be subdivided depending on the order of derivatives of the objective function used. Zero order methods, also known as gradient-free methods, use only the function values in their search of the minimum, while first and second order methods use respectively the first and the second order derivatives of the objective function (*T. Verstraete, 2014*). In most optimization methods a new design iteration is based on a previous one (*G. N. Vanderplaats, 1984*):

$$\overrightarrow{x_{i+1}} = \overrightarrow{x_i} + \alpha_i \overrightarrow{S_i} \tag{3.7}$$

where at the *i*-th iteration $\overrightarrow{x_{i+1}}$ is a new guess of the optimum design based on a previous guess $\overrightarrow{x_i}$, $\overrightarrow{S_i}$ is the search direction and $\alpha_i$ is a scalar defining the amplitude of the change in the $\overrightarrow{S_i}$ direction. The differences between all passible methods consist in the way $\overrightarrow{S_i}$ and $\alpha_i$ are determined.

### 3.1.1 Gradient-free and gradient-based optimization

There are a large number of algorithms for numerical optimization, they can be divided into one of two main categories: zero order methods and gradient-based methods.

In the first category are included the methods that rely on any information other than the value of the objective function. The simplest approach to minimize the objective function is to select randomly a large number of candidate design variables vectors and evaluate the objective for each of them (global search). This is called R*andom Search* and *Random Walk* (*G. N. Vanderplaats, 1984*). Another approach is the *Simulated Annealing* algorithm (*P. J. M. Van Laarhoven, E. H. L. Aarts, 1987*) and it is based on the analogy of the simulation of the annealing of solids. In material science, annealing denotes a physical process in which a solid is heated up to a maximum temperature value at which all particles of the solid randomly move in the liquid phase, followed by a slow cooling of the heat bath. In this way, all particles arrange themselves in low energy ground state of the solid lattice. In optimization, a random perturbation is made to an existing design $\vec{x}$ (similar to the random walk) and this new design is evaluated. The probability that the next design replaces the previous one is based on a virtual temperature and a virtual energy. The virtual energy

is equal to the difference in performance between both designs, while the virtual temperature decreases with iteration steps and reduces the probability of accepting the worse design. Among the zero-order approaches, *Evolutionary Algorithms* are widely used and they are based on Darwinian evolution, whereby populations of individuals evolve over a search space and adapt to the environment by the use of different mechanisms such as mutation, crossover and selection. A design vector $\vec{x}$ is called an individual; the objective function is replaced by the fitness of an individual, which is the quality that needs to be optimized. They were originally developed by *J. H. Holland* (*1975*) and *I. Rechenberg* (*1973*). Many evolutionary strategies exist, the most popular one is the *Genetic Algorithm* (*D. Goldberg, 1989)* that is based on the mechanism of natural selection and uses the survival of the fittest to obtain the optimum. The population consists in a fixed number of individuals, and each individual is represented by a binary string, containing all the values of the parameters. The binary representation of an individual is a cornerstone, which allows to define reproduction mechanisms similar to those found in nature. Two different individuals can mate and generate two children. Another promising evolutionary method, named *Differential Evolution*, has been developed by *K. Price* and *N. Storn* (*1997*) and it does not require continuous objective function and it is noise tolerant. To conclude this brief overview of the zero order method for optimization, *Particle Swarm Optimization* is mentioned. This method was proposed by *J. Kennedy* and *R. Eberhart* (*1995*) and it is based on the movement of organism in a bird flock or fish shoal, adapted to model human social behaviour.

In the gradient based optimization category are present the methods which use not only the value of the objective function but also its gradient with respect to the design parameters. Gradient-based optimization algorithms interpret first and sometime second order sensitivity information to take steps in the design space that will lead to the optimum. The main advantage of gradient methods is that they typically converge to the optimum with significantly smaller number of function evaluations, and are usually being more efficient than zero order methods. Unfortunately, these methods only work well when the objective function varies smoothly and without discontinuity and noise within the space design. Moreover, they only guarantee convergence to a local optimum (*J. R. R. A. Martins, 2002; T. Verstraete, 2014*). The simplest and one of the least efficient first order method is the *Steepest Descent*. This method proposes a new design in the direction where the

objective function is decreasing the most. A very important method that estimates a feasible direction of descent from first order information of objective function and inequality constraints is the *Method of Feasible Direction* (*G. Zoutendijk, 1960; G. N. Vanderplaats, 1983; X. Chen, M. M. Kostreva, 2000*). A modified version of this method was used to solve the optimization problems during the present work. Other methods are based on the steepest descent method, but use information of previous iterations to accelerate the convergence. One of these is the *Conjugate Direction* method. *Newton* methods require second order sensitivity information in addition to the first derivatives and exhibit a much larger rate of convergence. *Quasi-Newton* methods approximate the second order sensitivity during the search. In most of these methods, $\alpha_i$ is determined by performing a 1D minimization of $f\left(\overrightarrow{x_i} + \alpha_i \overrightarrow{S_i}\right)$. Several algorithms exist for determining the minimum of a 1D problem, requiring additional evaluation of the objective function (*G. N. Vanderplaats, 1984; J. Nocedal, S. J. Wright, 2006*).

Both zero and first order classes of optimization algorithms have a role in solving engineering problems. In a problem with a limited number of design variables with multiple local minima of discontinuities, it is clear that a zero order method is more suitable. Conversely, many single-discipline aircraft design problems are characterized by having a large number of design variables and a smooth design space. These problems are amenable to the use of gradient-based optimization algorithms. In particular, gradient methods are used extensively for aerodynamic shape optimization problems because there are often parameterized with hundreds of design variable and usually require computationally expensive analyses. With a few exception (*S. Obayashi, D. Sasaki, 2002; D. Sasaki at al., 2001*), such requirements make the use of zero order methods infeasible for aerodynamic shape optimization problems (*J. R. R. A. Martins, 2005*).

*Z. Lyu et al.* (*2014*) compared several optimization algorithms. Figure 3.1 helps in visualizing the effect of increasing the dimension of the problem by plotting the number of function evaluations required to converge the optimization for an increasing number of design variables.

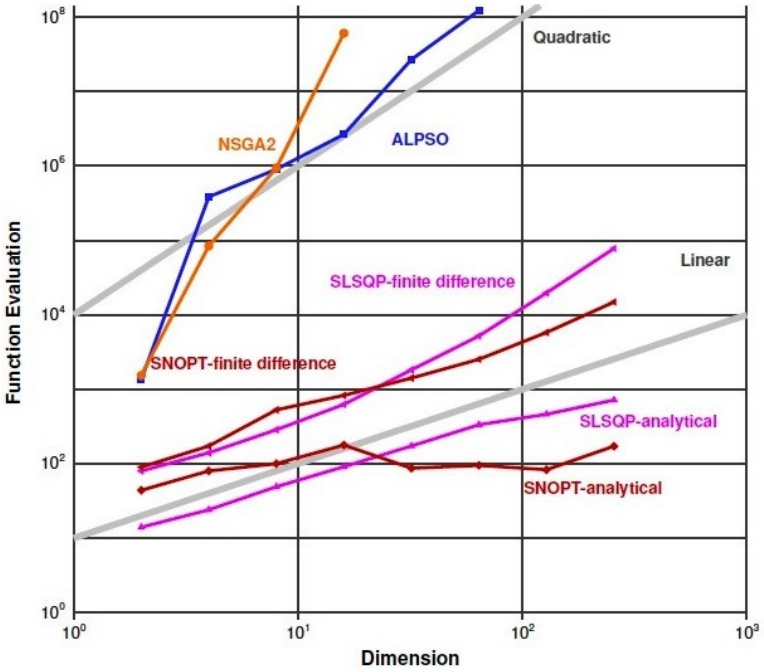


**Figure 3.1: Gradient-free methods require an excessive number of function evaluations for large number of variables (*Z. Lyu et al., 2014*)**

The gradient-free methods tend to have quadratic or cubic growth of function evaluations with increasing dimensionality, while the gradient-based methods follow a linear trend. In the study, the optimizers were compared using a multi-dimensional Rosenbrock function and it ended up with gradient-free methods that take 2 to 4 orders of magnitude more function evaluations to converge the optimization than most gradient-based methods (*Z. Lyu et al., 2014*). Conversely, the gradient-free methods have a higher probability of converging to a point near by the global optimum and they are generally simpler to implement. *D. W. Zingg et al.* (*2008*) performed a comparison of genetic algorithm and gradient method in aerodynamic airfoil optimization. Depending on the nature of the problem, the number of design variables, and the degree of convergence, the genetic algorithm requires from 5 to 200 times more function evaluations than gradient-based algorithm. *D. W. Zingg et al.* (*2008*) underline that since gradient-based and gradient-free optimization algorithms each have strengths and weaknesses, the choice is problem dependent. Actually, it was suggested genetic algorithm was more suited for preliminary design with low-fidelity models. Gradient-based optimizers may be more appropriate for detailed designs with high-fidelity models. The key disadvantages of gradient-based methods are the strengths of genetic algorithms. First, the development cost for the latter is minimal; second, the genetic algorithms are tolerant of noise in

the objective function. Furthermore, gradient-free methods possibly find the global optimum. The key disadvantage associate with genetic algorithms is that they can converge very slowly. *S. Obayashi* and *T. Tsukahara* (*1997*) compared a gradient-based method and a genetic algorithm on an airfoil lift maximization problem. The gradient-free method required the highest number of function evaluation, but it achieved the best design. An analogous comparison was conducted by *P. D. Frank* and *G. R. Shubin* (*1992*) and *N. F. Foster* and *G. S. Dulikravich* (*1997*).

A gradient-based approach was chosen to conduct the present work. Since the preliminary design phase is considered, the efficacy of the gradient-based methods in reaching the optimum was preferred to the capability of finding the global optimum of the gradient-free methods, even if multiple local optima are expected especially for aerodynamic optimisation. The modified method of feasible direction was chosen as search techniques, while the evaluation of the gradients was performed by using adjoint method (Sec. 3.1.22).

### 3.1.2 Sensitivity analysis: the adjoint method

In Sec. 3.1.1 was underlined the fact that gradient-based methods require much less function evaluations than gradient-free approach. It is important to observe that the efficacy of the gradient-based methods strongly depends on the way gradients are calculated. The gradient can be computed via *finite differences*, *complex-step method*, *algorithmic differentiation* and *adjoint method*. For a review of methods for computing sensitivity analysis, see *J. E. V. Peter* and *R. P. Dwight* (*2010*) and *J. R. R. A. Martins* and *J. T. Hwang* (*2013*). The simplest approach to compute the gradient in one design point is by evaluating the objective function with a small perturbation of each design variable. This method is the so-called *finite difference method* (*R. M. Hicks, P. A. Henne, 1978; J. C. Vassberg, A. Jameson, 2014*) and it is extremely easy to implement. The main disadvantage if it is that the number of objective function computations to estimate the gradient is proportional to the number of the design variable $(n + 1)$. Moreover, the amplitude of the perturbation has to be carefully chosen since it will affect the accuracy of the gradient approximation (*T. Verstraete, 2014*). The *complex-step method* (*S. Squire, G. Trapp, 1998; W. K. Anderson et al., 2001; J. R. R. A. Martins et al., 2003*) is a method to calculate sensitivity that maintains the simplicity of finite difference but is more accurate, even though it requires code to be able to handle complex

numbers. It uses imaginary perturbation of the objective function instead of a real one. *J. R. R. A. Martins et al.* (*2003*) evaluated that the computational expense of evaluating the gradient using finite difference of complex step methods is prohibitive for shape optimization with respect to hundreds of variables. *Algorithmic differentiation*, also named *automatic differentiation*, computes the gradient of the objective function by making use of the chain rule (*N. R. Gauger, 2008; L. L. Green et a., 1993; A. Griewank, 1989; C. Bischof et al., 1992*). The implementation is at the programming level, where for the computation of each value, also the derivative of that value is computed. By applying the chain rule to a formula that computes the output of a function based on a given input values, also the derivative of the function can be computed, provided that the derivatives of the input values are given. *T. Verstraete* (*2014*) underlines that the main advantage of this method is that the gradient can be computed with the greatest possible accuracy. The drawback is that the gradient computation speed is dependent on the number of design variables. Thus, the cost of computing gradient can still be prohibitive when optimizing a design parameterized with a large number of variables. Fortunately, there are other techniques for computing sensitivities whose cost is independent of the number of design variables. In particular, the *adjoint methods* allow the computation of sensitivities for an arbitrary number of design variables, at a cost that is similar to that of a single function evaluation, in case that the number of design variables is greater than the number of functions for which the sensitivity is sought (*J. R. R. A. Martins, 2005*). This method is the one used in this work for sensitivity analysis. *M. B. Giles* and *N. A. Pierce* (*1997, 2000*) clearly explain adjoint equations in CFD and they introduce the adjoint approach to design.

*J. R. R. A. Martins* (*2002*) investigated on the comparison of the adjoint methods with the finite difference and complex-step methods. Figure 3.2 shows the cost of calculating a gradient vector with respect to the number of design variables.

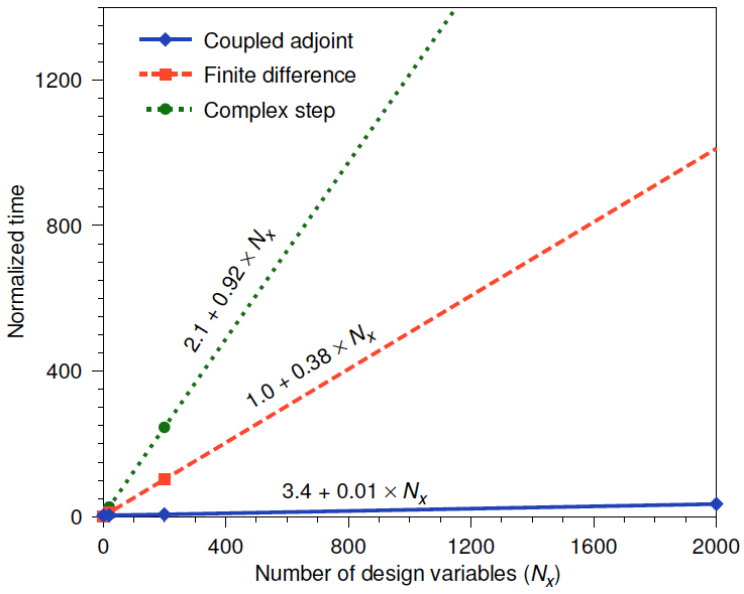


**Figure 3.2: Computational time vs. number of design variables for finite differencing, complex-stap and adjoint (*J. R. R. A. Martins, 2002*).**

The cost of a finite difference gradient evaluation increases linearly as long as the variables increase, and the cost of the complex-step method is, on average, 2.4 times higher than that of finite differencing. However, the author underlined that this cost penalty may be worthwhile since there is no need to find an acceptable step size *a priori*, as is the case for finite difference approximations (*J. R. R. A. Martins at al., 2000; J. R. R. A. Martins at al., 2001*). The cost of computing sensitivities using adjoint method is in theory independent of the number of variables. In the abovementioned case there is a small dependence due to the particular implementation of the presented adjoint method. The adjoint method requires a very good convergence of the simulation residuals, and that it is not always easy.

*O. Pironneau* (*1973*) pioneered the adjoint approach by deriving the adjoint of the Stoke equations and the incompressible Euler equations (*O. Pironeeau, 1974*) to optimize airfoil profiles. *A. Jameson* (*1988*) extended the adjoint method to handle inviscid compressible flows, making it suitable for transonic airfoils design. The adjoint implementation for the compressible Euler equations has been used by several researchers (*O. Baysal, M. E. Eleshaky, 1991; S. Ta'asan, G. Kuruvila, M. D. Salas, 1992*). *J. J. Reuther at al.* (*1996, 1999*), for instance, performed the aerodynamic shape optimization of complete aircraft, while *J.E. Hicken* and *D.W. Zingg* (*2010*) performed drag minimization of nonplanar geometries. The adjoint method has been then extended

to compressible Navier-Stokes equations with turbulence models. With that, *A. Jameson et al.* (*1998*) optimized a wing-body configuration, while *W. K. Anderson* and *D. L. Bonhaus* (*1999*) optimized airfoils by using the linearization of the Spalart-Allmaras turbulence model. *E. J. Nielsen* and *W. K. Anderson* (*1999*) further extended the approach to the 3D RANS equations and they optimized the ONERA M6 wing, while *R. P. Dwight and J. Brezillon* (*2009*) and *J. Brezillon* and *R. P. Dwight* (*2012*) optimized the DLR F6 wing.

Many optimization problems state as follows (*T. Verstraete, 2014*):

| | | | |
|---|---|---|---|
| *Minimize:* | $I(\boldsymbol{U}, \vec{\alpha})$ | Cost function | |
| *Subject to:* | $R(\boldsymbol{U}, \vec{\alpha}) = 0$ | State Equation | |
| *Where:* | $\boldsymbol{U}(\vec{\alpha})$ | State Vector | (3.8) |
| | $\vec{\alpha}\begin{cases}\alpha_1 \\ \cdots \\ \alpha_n\end{cases}$ | Control Variables | |

Essential in this formula is the appearance if the state vector, which needs to satisfy the state equation as an equality constraint. To compute the sensitivity of the cost function with respect to one control variable $\alpha$, the chain rule is used:

$$\frac{dI(U,\vec{\alpha})}{d\alpha} = \underbrace{\frac{\partial I}{\partial U}}_{\text{easy}} \cdot \underbrace{\frac{dU}{d\alpha}}_{\text{difficult}} + \underbrace{\frac{\partial I}{\partial \alpha}}_{\text{easy}} \tag{3.9}$$

The first and the third term of Eq. 3.9 are not complicated, as the cost function $I$ is expressed as an explicit function of the state variable $U$ and control variables $\alpha$. The computation of the second term $\frac{dU}{d\alpha}$ is more complicated. In order to compute it, the equation that govern the state variable has to be considered:

$$R(\boldsymbol{U}, \vec{\alpha}) = 0 \tag{3.10}$$

When differentiating the state equation, one obtains:

$$\frac{\partial R}{\partial U} \cdot \frac{dU}{d\alpha} + \frac{\partial R}{\partial \alpha} = 0 \tag{3.11}$$

and $\frac{dU}{d\alpha}$ can be found by solving linear system of equations:

$$\frac{\partial R}{\partial U}\cdot\frac{dU}{d\alpha}=-\frac{\partial R}{\partial \alpha} \tag{3.12}$$

Explicitly, with $N$ discrete state variables $u_i$, and $N$ non-linear equations $R_i(u_1,\dots,u_N,\alpha)$:

$$\begin{bmatrix}\frac{\partial R_1}{\partial u_1} & \cdots & \frac{\partial R_1}{\partial u_N}\\ \vdots & \ddots & \vdots\\ \frac{\partial R_N}{\partial u_1} & \cdots & \frac{\partial R_N}{\partial u_N}\end{bmatrix}\cdot\begin{bmatrix}\frac{du_1}{d\alpha}\\ \vdots\\ \frac{du_N}{d\alpha}\end{bmatrix}=-\begin{bmatrix}\frac{\partial R_1}{\partial \alpha}\\ \vdots\\ \frac{\partial R_N}{\partial \alpha}\end{bmatrix} \tag{3.13}$$

If many design variable $\alpha_j$ are considered instead of only one, many linear systems have to be solved:

$$\begin{aligned}\frac{\partial R}{\partial U}\cdot\frac{dU}{d\alpha_1}&=-\frac{\partial R}{\partial \alpha_1}\\ &\vdots\\ \frac{\partial R}{\partial U}\cdot\frac{dU}{d\alpha_n}&=-\frac{\partial R}{\partial \alpha_n}\end{aligned} \tag{3.14}$$

For each solution of the linear system, one next obtains the sensitivity of the cost function by applying Eq. 3.9. Since this method requires many linear systems to be solved, it is very ineffective. The adjoint method reduces this effort. Three different explanations can introduce the adjoint method; here, only one will be presented. Please, refer to (*T. Verstraete, 2014; M. B. Giles, N. A. Pierce, 1997 and 2000*) if the three explanations are needed.

Consider again only one control variable $\alpha$. The two linear equations to be considered are Eq. 3.9 and 3.12. By writing the Eq. 3.12 as follows:

$$\frac{dU}{d\alpha}=-\left(\frac{\partial R}{\partial U}\right)^{-1}\frac{\partial R}{\partial \alpha} \tag{3.15}$$

and plugging this equation into Eq. 3.9 and rearranging the terms, results in:

$$\frac{dI}{d\alpha}=-\frac{\partial I}{\partial U}\cdot\left[\left(\frac{\partial R}{\partial U}\right)^{-1}\cdot\frac{\partial R}{\partial \alpha}\right]+\frac{\partial I}{\partial \alpha} \tag{3.16}$$

$$\frac{dI}{d\alpha}=-\left[\frac{\partial I}{\partial U}\cdot\left(\frac{\partial R}{\partial U}\right)^{-1}\right]\cdot\frac{\partial R}{\partial \alpha}+\frac{\partial I}{\partial \alpha} \tag{3.17}$$

or:

$$\frac{dI}{d\alpha} = -V^T \cdot \frac{\partial R}{\partial \alpha} + \frac{\partial I}{\partial \alpha} \tag{3.18}$$

where $V$ is the solution of:

$$\left(\frac{\partial R}{\partial U}\right)^T \cdot V = -\left(\frac{\partial I}{\partial U}\right)^T \tag{3.19}$$

This means that the Eq. 3.19 has to be solved at first, then plug $V$ in Eq. 3.18. Eq. 3.19 is called *adjoint* equation. In case several control variables are considered, the solution of the Eq. 3.19 can be reused to compute the sensitivity of the cost function with respect to $\alpha_j$. Thus, the linear system 3.19 needs to be solved only once, and then the sensitivity $\frac{dI}{d\alpha}$ can be easily calculated for each design variables.

So far the so-called *discrete adjoint formulation* (*M. B. Giles, N. A. Pierce, 2000; G. B. Shubin, P. D. Frank, 1991; G. W. Burgreen, O, Baysal, 1996*) was considered, as the state equation is considered in its discrete form. A *continuous adjoint formulation* on the other hand, considers the state equation prior to discretization, and derives an adjoint equation, which then is discretized. Please, refer to (*M. B. Giles, N. A. Pierce, 2000; O. Pironneau, 1984; A. S. Zymaris et al., 2009; D. I. Papadimitriou, K. C. Giannakoglou, 2007*) for further information on the continuous adjoint method. To complete the overview of the adjont method, it is important to underline that a number of research groups have developed adjoint CFD codes for design optimization (*W. K. Anderson, V. Venkatakrishnan, 1997; H. Cabuk et al. 1991; J. R. R. A. Martins, 2005*). The discrete adjoint formulation is the one adopted in *elsA*, whose expression have been differentiated formally (*A. Dumont et al., 2011*).

## 3.2 Aerodynamic Optimization

In this section, Aerodynamic and Aero-elastic optimizations are presented. In particular, Sec. 3.2.1 describes optimization workflow and the procedures involved in it. Sec. 3.2.2 presents the wing optimization with an investigation on the design variable for efficient optimization procedure. The differences in results between considering a rigid or flexible wing are underlined in Sec. 3.2.3, as well as the comparison between experience-based design variable and vertex-morphing method.

As described in Chapter 2, in order to be compatible with the fast turn-around time required by preliminary design the Euler equations are solved to model the aerodynamic flow around the aircraft. While inviscid approach has been considered, it captures the non-linear aerodynamic effects occurring in transonic flows, which are essential in the aerodynamic design of a transport aircraft. Even if this work could be straightforwardly extended to RANS formulation, such model appears as a significant improvement over much simpler models used traditionally at preliminary design stage (semi-empirical, lifting line, …).

The author is aware of the importance of including viscous effects in aerodynamic shape optimization, as discussed by many other authors (*J. K. Elliot*, 1998; *L. M. Osusky, 2014; Z. Lyu et al., 2014*). While Euler-based optimizations can provide design insights, the resulting optimal Euler shape is significantly different from the one obtained by RANS. Euler-optimized shapes tend to exhibit a sharp pressure recovery near the trailing edge, which is non-physical because such conditions near the trailing edge would cause separation. For those reasons, in the present works only cruise conditions are considered during the aerodynamic optimization, in order to mitigate the possibility to end up in flow separation impossible to catch by Euler equations.

### 3.2.1 Optimization procedure

The optimization process is very similar for the aerodynamic and aero-elastic optimizations, and it is described in Figure 3.3.

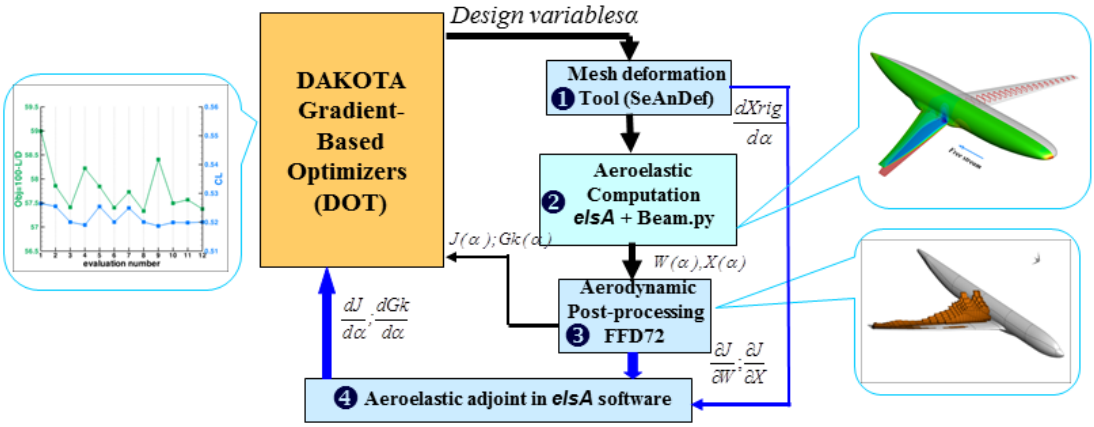


**Figure 3.3: Flowchart of the optimization procedure**

The two main components are the optimization library DAKOTA (*Dakota, date accessed*) which encapsulates different optimization algorithms and the simulation process. The method used for the present optimization is the gradient discrete adjoint-based method. The chosen optimization technique is the "method of feasible directions" (*J. R. R. A. Martins, 2005; M. B. Giles, 1997*). This method relies on a process to find the search directions which is based on a very practical engineering design sense. It must at each iteration try to follow two main goals: improving the objective function minimising it and at the same time satisfy the constraints imposed on the design space. Because of the presence of the constraints on the design space not all usable directions are possible without activating or violating one (or several) of the constraints. Hence, to find a successful search direction, a sub-problem of optimisation is addressed to find the so-called feasible direction for which the dot product of it with all the gradients of the constraints must be negative. For details refers to (*G. N. Vanderplaats, 1984*).

Beside the optimizer, the aerodynamic analyser (or aero-elastic one when fluid-structure interaction coupling is accounted) performs the computation of the aerodynamic coefficients and the sensitivity of the objective and constraint functions with respect to the design variables. The FFD72 drag extraction tool enabled to have sensitivities of the drag components (induced and wave drag). It is important to notice that the aero-elastic optimization does not take into consideration any sensitivity of the objective function with respect to the structural variables. An aerodynamic optimization was performed, letting the structure deforms under the aerodynamic load.

As described in Sec 3.1.2, due to the adjoint formulation the computation of the sensitivity is almost independent of the number of variables of the optimization problem. That is really important in preliminary design because it allows having as many variables as necessary in order to perform a wide exploration of the design space. With the relevant benefits the adjoint formulation brings, the freedom that characterizes the early stages of the aircraft design could be largely exploited. The analyser is composed of the following components (*A. Dumont et al., 2011)*:

- A mesh deformation tool, called SeAnDef (Sequential Analytic Deformation), which propagate in the computational grid the wing shape variation, with the body-fit techniques;
- The *elsA* CFD code (*elsa*-BAG in case of aero-elastic coupling);
- The aerodynamic post-processing tool FFD72;
- The aerodynamic and aero-elastic adjoint solver implemented in *elsA*.

The CFD code, the aero-elastic coupling and the post-processing tool FFD72 was introduced in Chapter 2.

### 3.2.2 Design variables for efficient optimization

An investigation of the relation between the design variables and the flow conditions in the context of aerodynamic wing optimization was carried out (*A. Viti et al., 2015*). For this study, the isolated wing geometry was considered. Two cruise conditions were chosen:

- shock free condition, $M = 0.75$ at $C_l = 0{,}5$, $h = 35000\ ft$;
- shocked flow condition, $M = 0.80$ at $C_l = 0{,}5$, $h = 35000\ ft$;

The global angle of attack as well as camber and twist at six control sections in spanwise direction were chosen as aerodynamic design variable. The set of parameters was chosen such that direct control over single flow-features is maintained whereas the overall number of variables is restricted to only a few effective ones. Hence the interpretation of the optimization results shall be facilitated. The control points along the wing are shown in Figure 3.4:

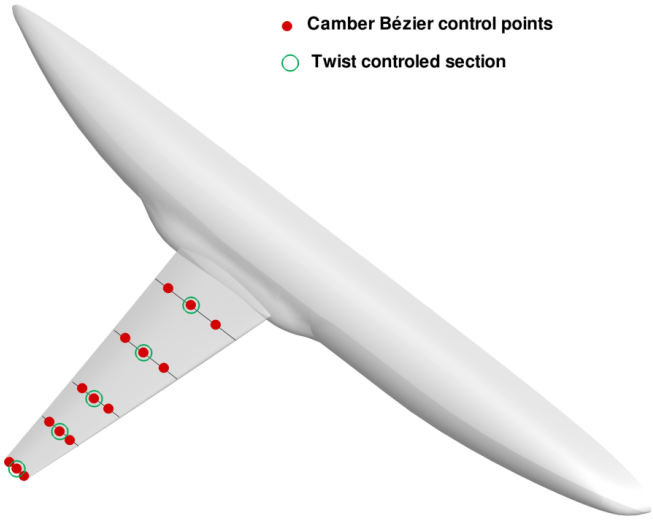


**Figure 3.4: Wing sections and Bézier points for camber definition**

For each cruise condition three different optimizations were run: the first set of variables included camber and twist for the control sections, while a second and third set included respectively inly camber or twist. The global angle of attack is ever present as variable. The camber is defined for each section by a chordwise Bézier curve controlled by 1, 3 or 5 control points at each selected position. Thus, a preliminary investigation to find the good number of Bézier points to define the camber was undertaken. It was seen that the god compromise between a good flow control and a fast optimization is 3 points, while 1 is not enough to cure shock problem and 5 points do not perform much better than the 3 points.

The optimization problem can be written as follows:

$$\begin{aligned} &\textit{min } J = C_{d_{ff}}(x_a) \\ &\textit{wrt } x_a \\ &\textit{e.c. } g = C_l - 0.5 = 0 \\ &R\,(U, x_a) = 0 \end{aligned} \tag{3.20}$$

Herein $C_{d_{ff}}$ represents the inviscid far-field drag coefficient, $x_a$ the aerodynamic design variables, $C_l$ the lift coefficient of the optimized design and $R(U, x_a)$ the Euler equations in residual form.

Figure 3.5 and 3.6 show the pressure distributions of the optimized wing and the pressure coefficient profiles at the root, 50% of the spanwise and tip. In particular, the line blue identifies the

baseline, the red line the optimum achieved by using camber as design variable, the green one is the optimum by using the twist as variable and the yellow line is for camber and twist together. Table 3.1 resumes the objective functions obtained.

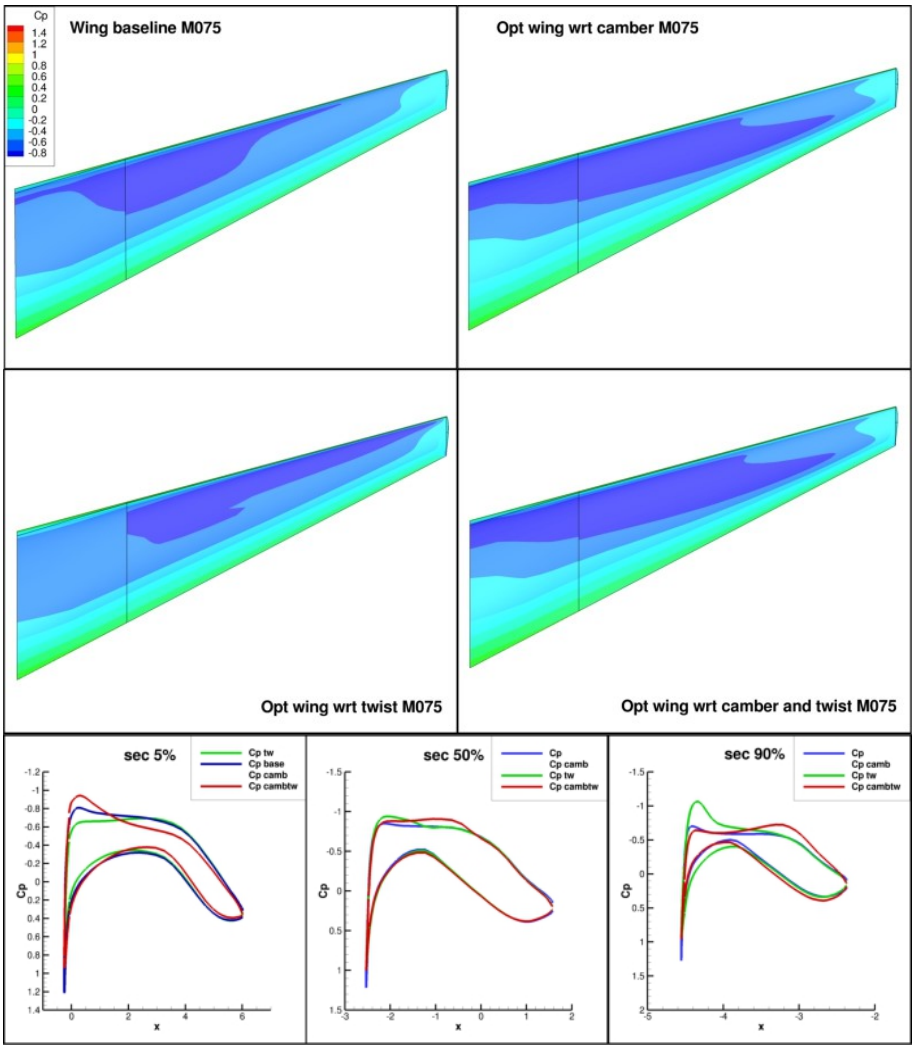


**Figure 3.5: Optimized isolated wing at M = 0.75 - Shock-free condition**

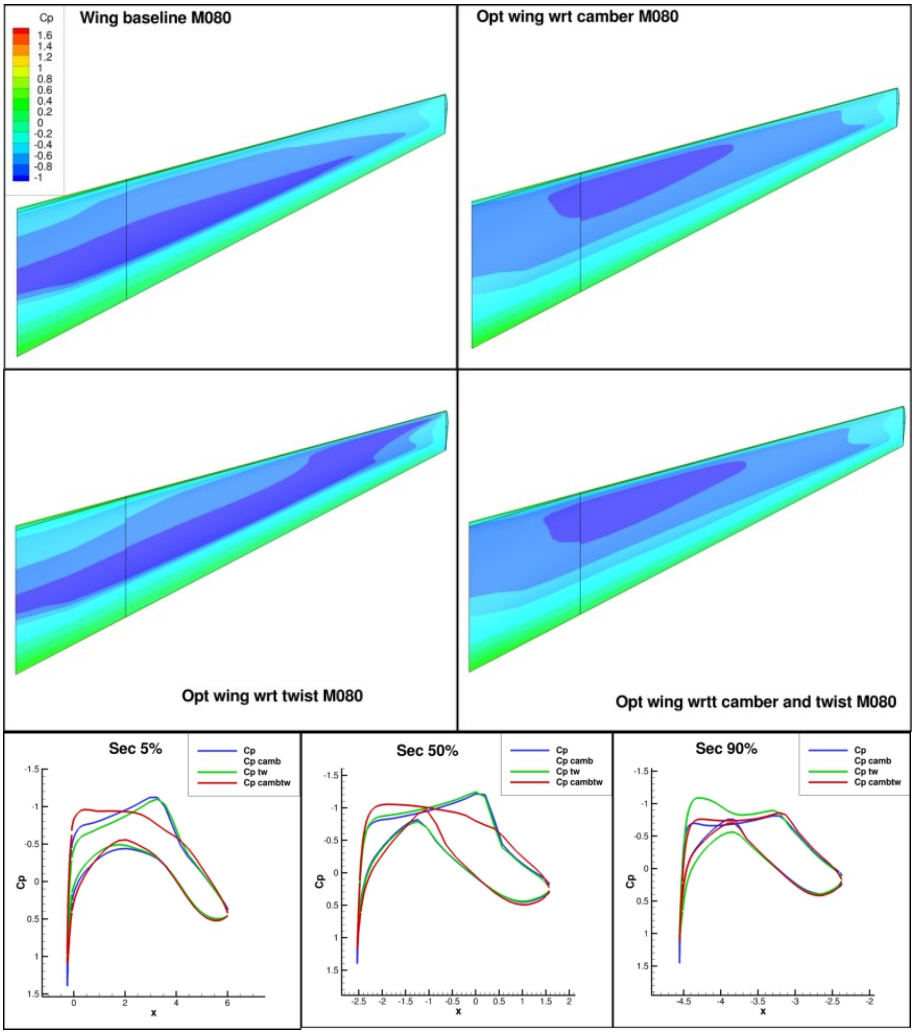


**Figure 3.6: Optimized isolated wing at M = 0.80 - Shocked condition**

| | Baseline | Camber | Twist | Camber & Twist |
|---|---|---|---|---|
| $\boldsymbol{M = 0.75}$ $\boldsymbol{L/D}$ | 50.48 | 54.33 | 54.31 | 54.36 |
| $\boldsymbol{M = 0.80}$ $\boldsymbol{L/D}$ | 33.06 | 46.40 | 36.62 | 46.52 |

**Table 3.1: Aerodynamic optimization results**

It is possible to see that in case of shock free condition, the three sets of design variables are able to get an optimum design close to each other. Camber alone and twist alone are able to achieve almost the same results in terms of lift-to-drag meaning that both are effective variables on which to base the aerodynamic optimization, showing a small difference in term of CPU-time demand. Same results are obtained when Camber and Twist are used together, showing that their

collaborations is not able to achieve any better than the two types of variables alone, while increasing the CPU-time for optimisation convergence. For the shocked condition the result is a bit different because is clear how much more important is the camber in comparison with the twist. In particular, twist is not able to alleviate the shock along the whole wing. The other two sets of design variable results to be similar in term of minimizing the objective function. However, the fewer variables are playing in the optimization the faster the optimization is.

Particular problems may occur during the optimisation process when one of the design variables has much more impact on the objective function than the others. For instance, the angle of attack significantly affects the drag of the configuration. It could happen that if the angle of attack at which the optimization starts is too far from the $C_l$ condition (the constraint of the optimization), the optimizer use with only this design variable, having not changed the others. For that reason, a wise choice of the starting point could bring into a better local minimum, thus into a better optimization result.

### 3.2.3 Aerodynamic and Aero-elastic optimization

The results of aerodynamic and aero-elastic optimization of the wing-body geometry were compared in order to understand the importance of considering structural displacement during preliminary design phase. As underlined in the section before, performing an aerodynamic optimization at the structural static equilibrium is of primary importance to have a reliable result, especially when an unconventional geometry is analysed. Moreover, the inconsistency of optimizing the flight shape will be underlined.

#### 3.2.3.1 Aerodynamic optimization investigation and importance of the aero-elastic optimization

The rigid aerodynamic optimization of the wing-body geometry was undertaken. The cruise conditions are: $M = 0.75$ at $C_l = 0.5$, $h = 35000\ ft$. The optimization problem is:

$$
\begin{aligned}
&\textit{min } J = C_{d_{ff}}(x_a) \\
&\textit{wrt } x_a \\
&\textit{e.c. } g = C_l - 0.5 = 0 \\
&R\,(U, x_a) = 0
\end{aligned}
\tag{3.21}
$$

Herein $C_{d_{ff}}$ represents the inviscid far-field drag coefficient, $x_a$ the aerodynamic design variables (global angle of attack, twist and camber of 6 control sections along the spanwise), $C_l$ the lift coefficient of the optimized design and $R(U, x_a)$ the Euler equations in residual form.

Regarding the control sections, there is an important issue for the wing-body configuration: the root of the wing (that is the intersection between the wing and the fuselage) cannot be used as control section, while for the isolated wing is taken. That happens because the mesh deformation tool (SeAnDef) is not able to handle this interface. For that reason, it is impossible to treat the root during the optimization in order to avoid the shock from appearing. A possible way to try to solve such problem has been investigated: the optimized shape of the isolated wing that corresponds to the cruise condition at $M = 0.80$ is taken as starting point for the wing-body aerodynamic optimization, then the aerodynamic optimization at $M = 0.75$ was performed ($C_l = 0.5$, $h = 35000\ ft$). The idea was to cure the shock at the intersection by using an already optimized wing shape for a very shocked cruise condition (see Sec. 3.2.2). The pressure distribution of the two aerodynamic optimizations for the wing-body configuration is shown in Figure 3.7, while the results are summarized in Table 3.2.

| $\boldsymbol{M = 0.75}$ | **Baseline wing Optimization** | **Pre-treated wing Optimization** |
|---|---|---|
| $\boldsymbol{L/D}$ | 52.8 | 54.1 |
| $\boldsymbol{C_{Di}}$ | $83.61 \cdot 10^{-4}$ | $79.23 \cdot 10^{-4}$ |
| $\boldsymbol{C_{Dw}}$ | $11.08 \cdot 10^{-4}$ | $12.60 \cdot 10^{-4}$ |

**Table 3.2: Results of baseline wing optimization and pre-treated wing optimization**

It is clear that the method does not work since the both the optimized wings performs inboard flow acceleration and the consequent shock. Moreover, the shock of the optimized pre-treated wing

results to be even stronger than the optimized baseline, underling that the treatment of the shock at the wing root is not easily solvable.

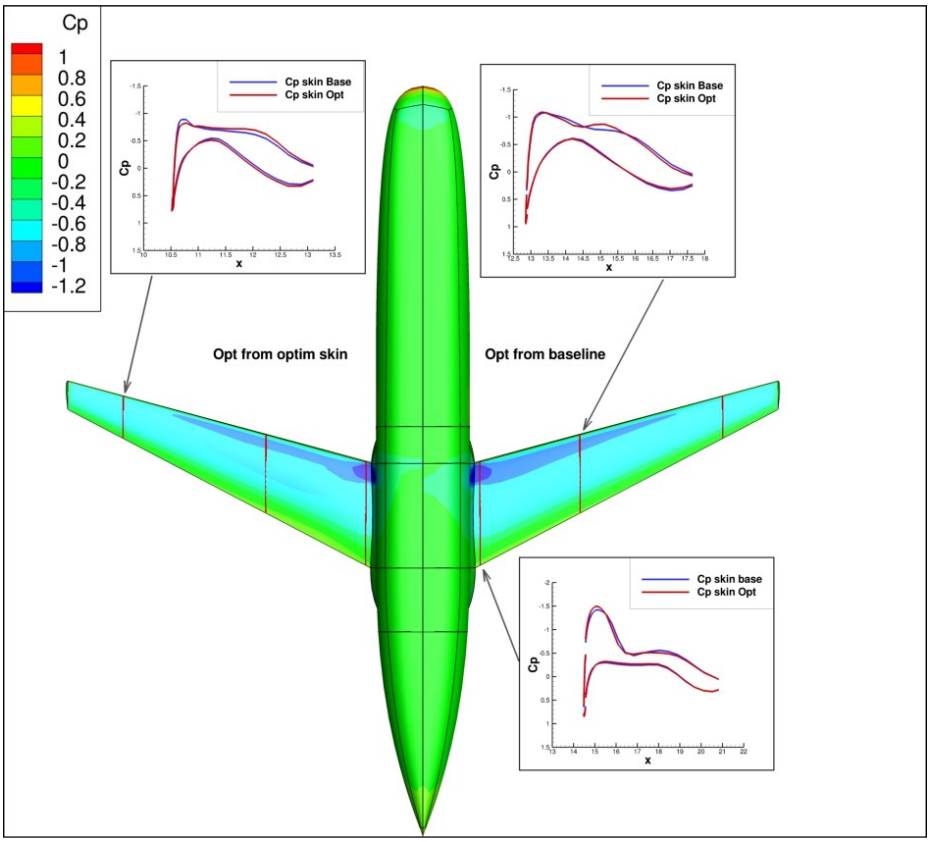


**Figure 3.7: Comparison between aerodynamic optimization results of the wing baseline (on the right, blue $C_p$) and the wing that is the result of the aerodynamic optimization of the isolated wing for shocked condition (on the left, red $C_p$).**

The aero-elastic optimization of the considered geometry was then carried out ($M = 0.75, C_l = 0.5,\ h = 35000\ ft$). The optimization problem is the same of the one before (rigid aerodynamic optimization), as well as the design variables (camber, twist and global angle of attack), while the structure is free to deform under the aerodynamic load. The aero-elastic optimum and the elastic polar are showed in Figure 3.8 and Figure 3.9 respectively. To clarify, the elastic polar is the polar for which each one of the points is in the aero-elastic equilibrium.

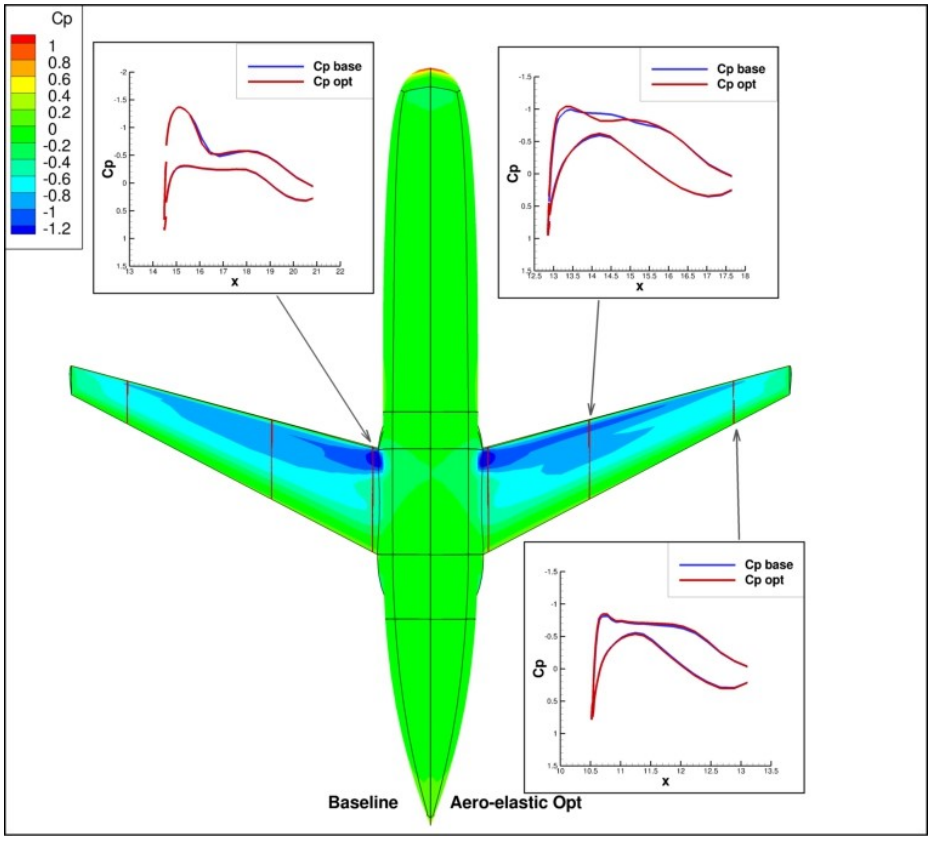


**Figure 3.8: Configuration baseline (on the left, blue $C_p$) and aero-elastic optimum (on the right, red $C_p$)**

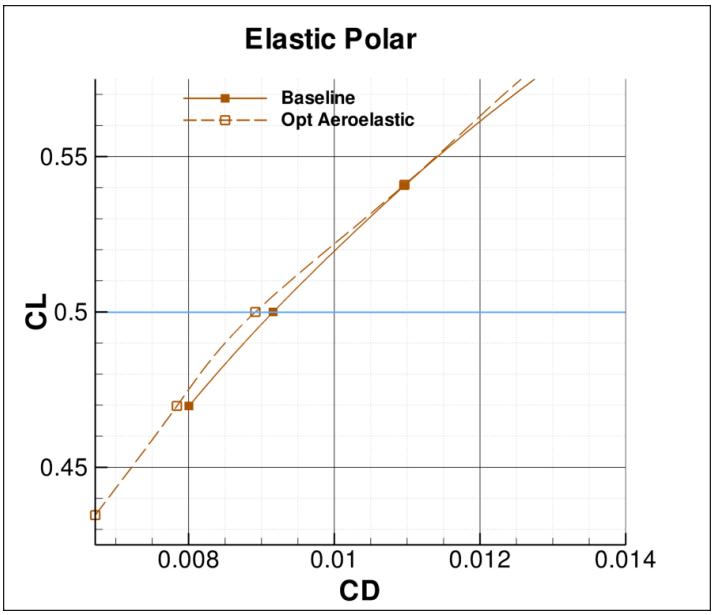


**Figure 3.9: Elastic polar of the configuration baseline and the aero-elastic optimum**

It is possible to see that the shock at the wing-body intersection cannot be solved. Thus, the optimizer can attempt to reduce the induced drag. That confirms once more the importance of

solving the problem due to wing-fuselage aerodynamic interaction. A study to solve this problem by using a new parameterization method is presented in Sec. 3.2.3.2.

In order to show the importance of the aero-elastic optimization in preliminary design phase already, a rigid aerodynamic optimization of the flight shape at the cruise condition listed before was performed. The optimization problem, the cruise conditions and the design variables are the same of the other two problems introduced so far. The structure is infinitely rigid, then it does not deform. This specific test case was chosen since it could be seen as an alternative optimization problem every time the aero-elastic optimization is not possible, since an FSI code has to be available. Figure 3.10 shows the result of the optimization.

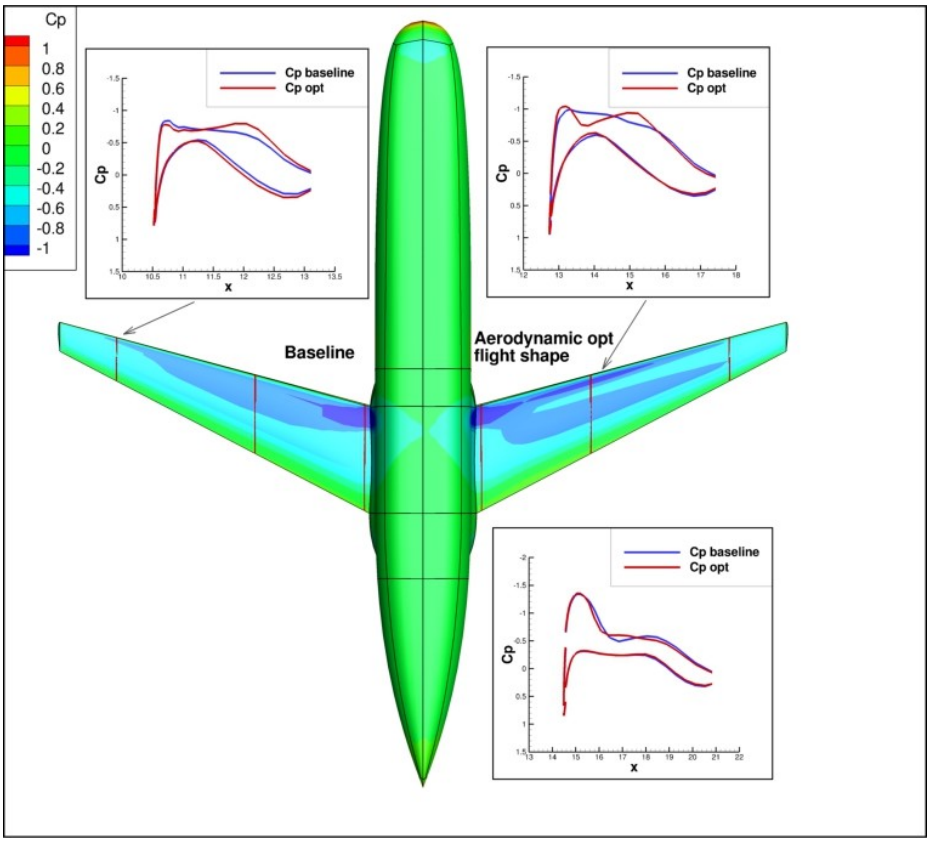


**Figure 3.10: Comparison between the flight shape of the baseline (on the left, blue $C_p$) and the rigid aerodynamic optimization of the flight shape (on the right, red $C_p$)**

Figure 3.11 shows the comparison among three elastic polar:

- the elastic polar of the wing-body baseline;

- the elastic polar of the wing shape having the value of the design variables as the optimum shape coming from the aerodynamic optimization of the flight shape;
- the elastic polar of the optimum reached by the aero-elastic optimization.

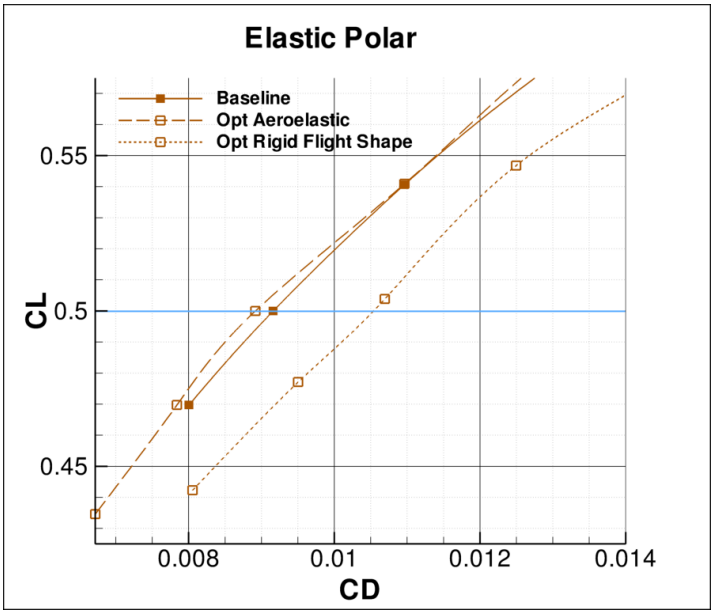


**Figure 3.11: Elastic polar of the baseline, the aero-elastic optimum and the rigid flight shape optimum**

These results clearly show that the aero-elastic effects can cancel and even degrade the performance achieved by optimization performed without accounting for these aero-elastic deformations. In fact, even if the aerodynamic optimization of the flight shape succeeds to give good result, the elastic polar shows the inconsistency of the alternative procedure. Since the aerodynamic optimization works on design parameters that also impact on the distribution of the wing load, the flight shape which is going to be optimized will be no more the real flight shape. Thus, this important inconsistency can generate an “optimum” shape that could be worse than the baseline.

#### 3.2.3.2 Comparison and combination of experience-based parameterization with vertex-morphing method

The previous aerodynamic optimization underlined the needs to investigate on a better shape parameterization for the wing-body intersection, since the so-called experience-based design variables are ineffective for this kind of problem.

Comparisons between experience-based design parameters and the vertex-morphing method in the context of the aerodynamic optimization of the forward-swept wing-body architecture is presented. Experience-based parameterization refers in this context to any shape control based on additional insight into the physical problem, like the wing twist, to maintain core design features. The vertex-morphing uses a node-based approach. Two different optimisation techniques are used: method of feasible direction and steepest descent method respectively for the experience-based variables and the vertex-morphing method. For complete details refers to (*D. Baumgärtner et al., 2016*).

Experience-based parameterization has the advantage of being able to incorporate designer knowledge into the optimization process, and then it helps avoid non-physical solution. Having only a few parameters may result in a very fast convergence of the optimizer. *G. Carrier et al.* (*2014*) investigated the impact of the specific geometry parameterization on the optimal solution for aerodynamic shape optimization. They underlined that with increasing number of parameters significant improvement can be obtained but also showed that an increasing design space results in convergence problems with the optimizer. One possible drawback of experience-based parameterization is that it could limits the design space making an exploration of alternative design solution difficult. An alternative approach is the node-based shape optimization also known as Vertex Assigned Morphing of Optimal Shape (*K.-U. Bletzinger, 2014; M. Hojjat et al., 2014; C. Othmer, 2014*). This method does not include any physically motivated parameterization but it sets on high design freedom with good optimization potential. Consequently, the method suffers from mesh dependency.

The first comparison of the two parameterization methods to evaluate benefits and drawbacks with respect to computational costs, design space exploration and quality of the optimal solution was carried out on the geometry of the wing. The optimization problem reads:

$$\begin{aligned} &\textit{min } J = C_{d_{ff}}(x_a) \\ &\textit{wrt } x_a \\ &\textit{e.c. } g = C_l - 0.635 = 0 \\ &R\,(U, x_a) = 0 \end{aligned} \tag{3.22}$$

Herein $C_{d_{ff}}$ represents the inviscid far-field drag coefficient, $C_l$ the lift coefficient of the optimized design and $R(U, x_a)$ the Euler equations in residual form. $x_a$ represents the aerodynamic design variables defined through an experience-based parameterization (already well defined for the previous optimizations) or the vertex-morphing method. The optimization is done at the following cruise condition: $M = 0.75,\ h = 35000\,ft$. Figure 3.12 depicts the corresponding convergence history of the objective function (far-field drag) as well as the lift coefficient compared to the specified constraint for the optimization based on experience-based parameterization. From the figure it is possible to see that the final design is reached after 43 optimization iterations comprising 43 primal CFD evaluations and 7 adjoint CFD computations. Both the objective and the constraint functions are converging. For the lift coefficient the converged value remains slightly off the target value, which is a consequence of a specified tolerance. The optimization results are summarized in Table 3.3.

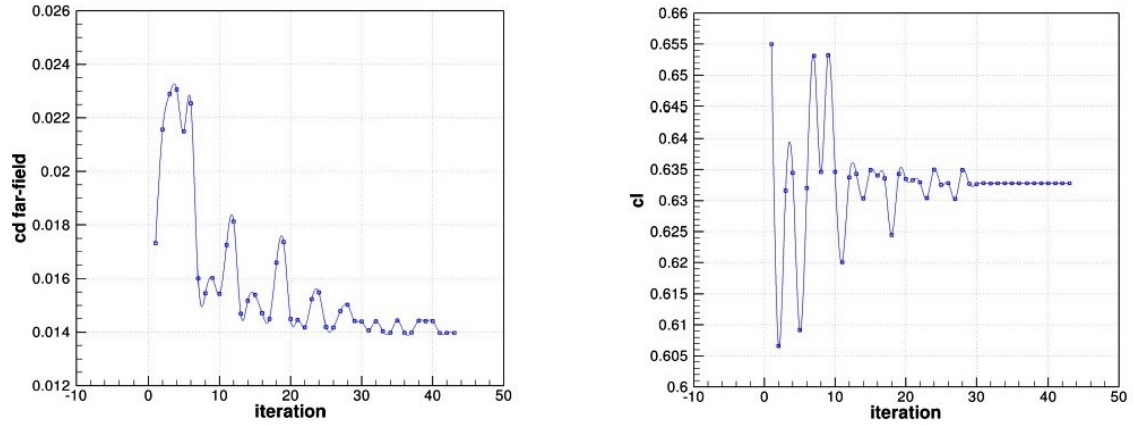


(a) Improvement of far-field drag coefficient (b) History of lift coefficient

**Figure 3.12: Convergence history of the wing shape optimization using an experience-based parameterization**

| | $C_{D\_ff}$ | $C_{D\_w}$ | $C_{D\_i}$ | $C_L$ | Iterations |
|---|---|---|---|---|---|
| **Baseline** | $157.91 \cdot 10^{-4}$ | $30.40 \cdot 10^{-4}$ | $127.51 \cdot 10^{-4}$ | 0.635 | - |
| **Optimized** | $139.72 \cdot 10^{-4}$ | $14.93 \cdot 10^{-4}$ | $124.79 \cdot 10^{-4}$ | 0.633 | 43 primal<br>7 adjoint |
| **Change [%]** | -11.57 | -50.89 | -2.14 | -0.34 | - |

**Table 3.3: Aerodynamic coefficients of the baseline and the optimum of the wing by using experience-based parameterization**

It can be seen that most of the drag improvement was gained through a reduction of the wave drag. Figure 3.13 show that the optimized wing results in alleviating the shock front around the wing centre in spanwise direction. In contrast to that, for the inboard section the optimization is not able to attenuate the strong shock zone around the wing root close to the leading edge. Since the wing root shock is strongly dependent to the wing-fuselage intersection, it is clear that the experience-based parameterization is not sufficient to control the shape towards a significant improvement of the inboard shock zone.

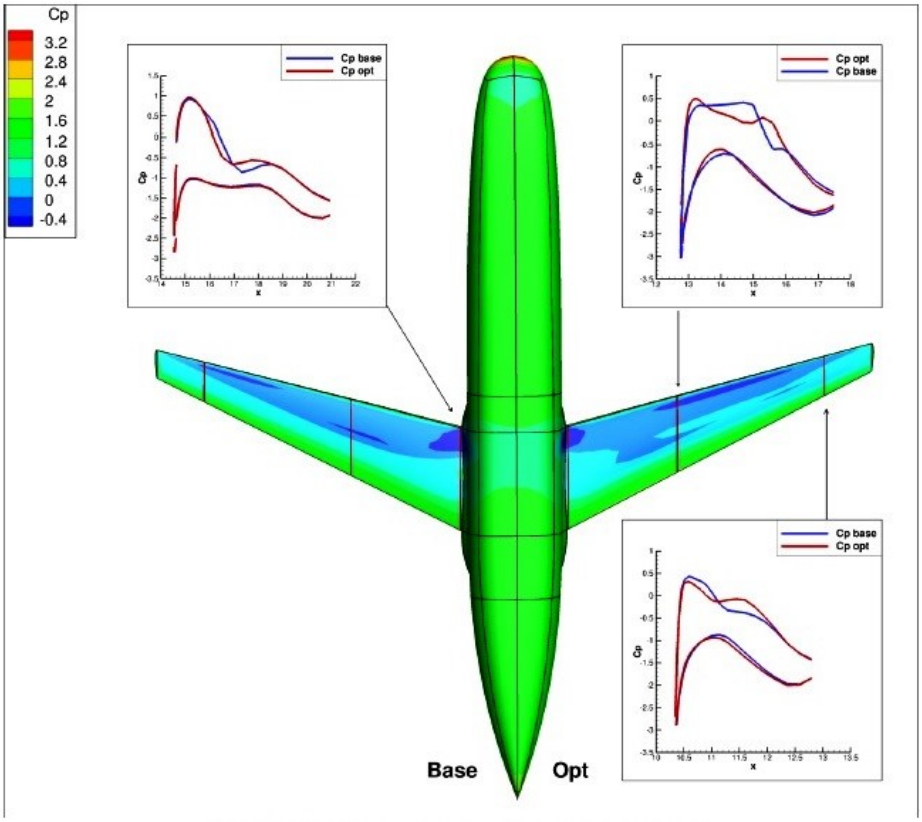


**Figure 3.13: Pressure distribution after optimization using experience-based parameterization**

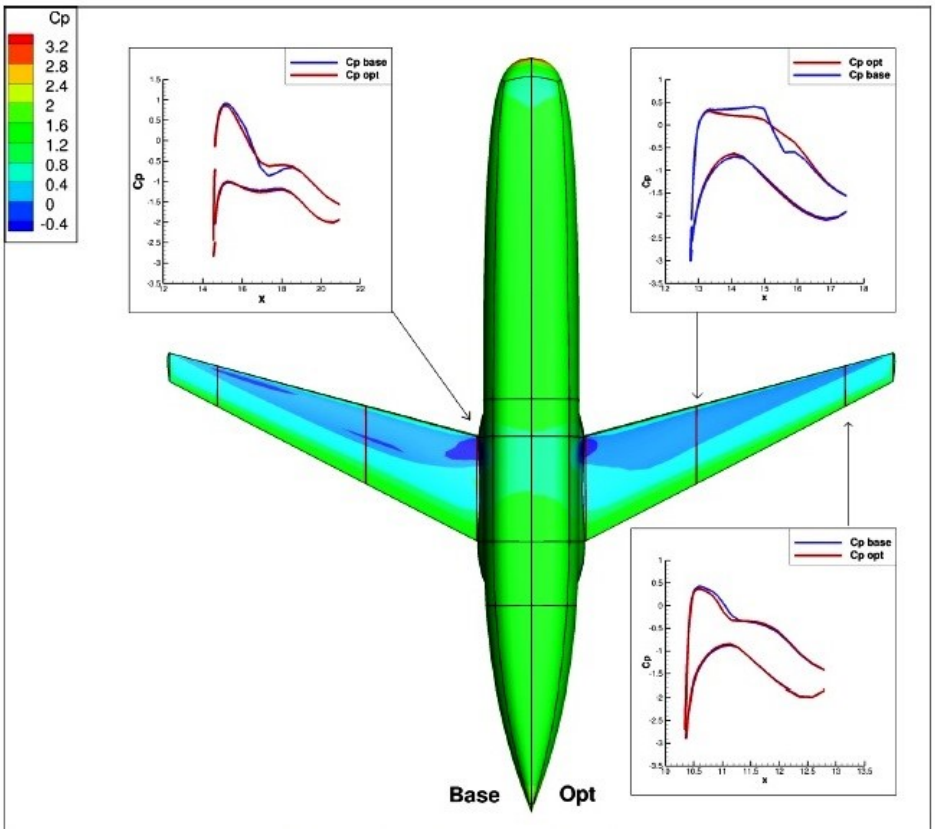


**Figure 3.14: Pressure distribution after optimization using vertex-morphing**

Figure 3.15 shows the convergence history for the present optimization problem using the vertex-morphing method. All the surface nodes on the wing ware used as design variables. Table 3.4 collects the corresponding results.

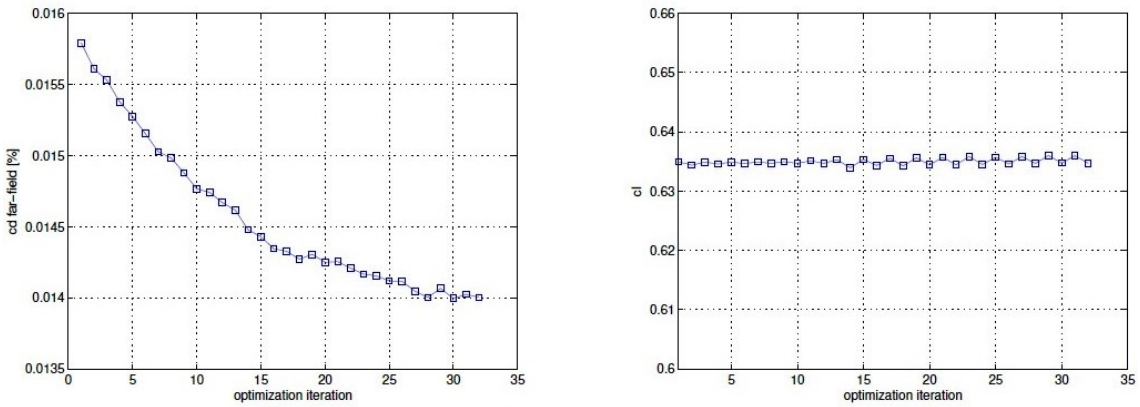


(a) Improvement of far-field drag coefficient (b) History of lift coefficient

**Figure 3.15: Convergence history of the wing shape optimization using vertex-morphing**

| | $C_{D\_ff}$ | $C_{D\_w}$ | $C_{D\_i}$ | $C_L$ | Iterations |
|---|---|---|---|---|---|
| **Baseline** | $157.91 \cdot 10^{-4}$ | $30.40 \cdot 10^{-4}$ | $127.51 \cdot 10^{-4}$ | 0.635 | - |
| **Optimized** | $140.02 \cdot 10^{-4}$ | $11.59 \cdot 10^{-4}$ | $128.43 \cdot 10^{-4}$ | 0.634 | 32 primal<br>32 adjoint |
| **Change [%]** | -11.20 | -61.85 | -0.72 | -0.04 | - |

**Table 3.4: Aerodynamic coefficients of the baseline and the optimum of the wing by using vertex-morphing**

It is seen that the final design was reached after 32 optimization iterations comprising 32 primal CFD evaluations and 32 adjoint CFD computations. Although this case needs fewer primal CFD iteration than the previous one (43 primal CFD iteration if experience-based parameterization is used), it needs much more adjont CFD computations, which usually are much more time-demanding than primal CFD computation. Concerning the optimization results, the total improvement of the objective function in both cases is almost the same. The reasons of this improvement are, however, different. In the second case the entire improvement is due to a decrease on wave drag which is stronger that in the first case. In fact, the experience-based parameters have a very global impact according to their definition, while vertex-morphing method focuses on local adjustment of the wing surface considering a global continuity (Figure 3.14). On the contrary, experience-based parameterization affects the induced drag much more than the local variation approach. It is important to realize that both approaches lead to true alternative designs.

The second investigation concerns the possibility to combine the two parameterization methods toward a more effective overall shape optimization process. In that way, the advantages of both approaches are utilized. The optimization problem remains unchanged. The only change concerns the set of parameters for the shape control of the vertex-morphing method. Actually, the inboard section including part of the wing and the fuselage showed in Figure 3.16 is considered.

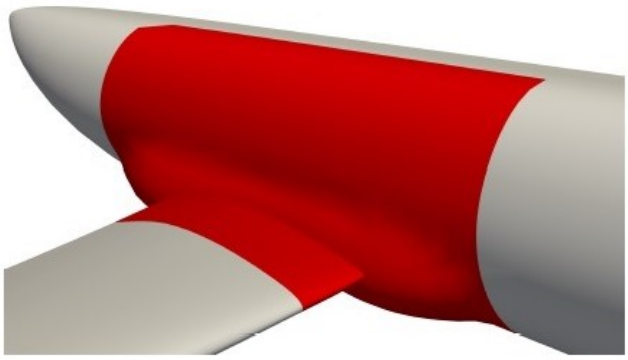

**Figure 3.16: Fuselage and inboard wing to be optimized using vertex-morphing**

Since both parameterization approaches performs differently, a sequential optimization approach is chosen rather than a monolithic process. The cruise condition, as well as the objective function and the constrain function do not change from the previous optimization problem. The optimization of the inboard wing-fuselage section by means of vertex-morphing method is run at first, and then the whole wing is optimized using the experience-based parameters. For this second optimization, the same set of design variables of the previous optimizations is used (global angle of attack, twist and camber at six different control sections along the spanwise).

The results of the sequential optimization are summarized in Table 3.5.

| | $C_{D\_ff}$ | $C_{D\_w}$ | $C_{D\_i}$ | $C_L$ | **Iterations** |
|---|---|---|---|---|---|
| **Baseline** | $157.91 \cdot 10^{-4}$ | $30.40 \cdot 10^{-4}$ | $127.51 \cdot 10^{-4}$ | 0.635 | - |
| **Inboard opt.** | $146.02 \cdot 10^{-4}$ | $18.15 \cdot 10^{-4}$ | $127.87 \cdot 10^{-4}$ | 0.634 | 31 primal<br>31 adjoint |
| **Wing opt.** | $131.92 \cdot 10^{-4}$ | $7.06 \cdot 10^{-4}$ | $124.86 \cdot 10^{-4}$ | 0.633 | 44 primal<br>7 adjoint |
| **Change [%]** | -16.46 | -76.77 | -2.08 | -0.43 | - |

**Table 3.5: Optimization results of sequential shape optimization using combined parameterization**

It is possible to see that the far-field drag in total decreases by 16.46%, which is around 5% more than in the previous optimizations, where only the wing was considered. Note that after the optimization of only the inboard the objective function was already improved by around 8%, underling the importance of this area. Apart from the big quantitative changes in the optimized

design, a very different surface pressure was also observed. Figure 3.17 shows the comparison of the surface pressure distribution between the optimized design of Figure 3.13 and the final design.

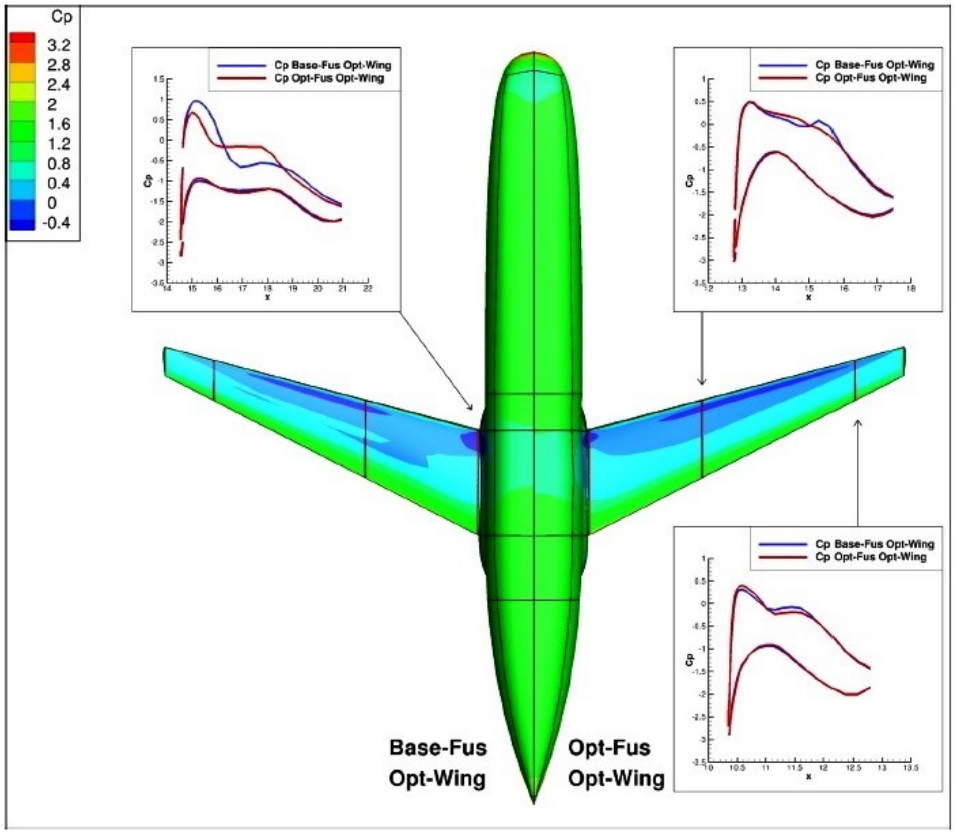


**Figure 3.17: Pressure distribution after sequential optimization in comparison to the baseline**

The first characteristic of the optimized design is the alleviated shock regions. Specifically, on the wing-fuselage intersection the shock is reduced in favour of a plateau of pressure values. Then, a clear improvement of the inboard flow behaviour is obtained. An improvement in the lift distribution is also obtained, showing the ability of this sequential approach to get advantages from both parameterization methods.

The last investigation that was undertaken concerning the vertex-morphing method was the optimization of the entire wing-fuselage configuration. The optimization problem remains the same as the one before, while changing the nodes that are used as design parameters. The results of this investigation are shows in Table 3.6.

| | $C_{D\_ff}$ | $C_{D\_w}$ | $C_{D\_i}$ | $C_L$ | Iterations |
|---|---|---|---|---|---|
| **Baseline** | $157.91 \cdot 10^{-4}$ | $30.40 \cdot 10^{-4}$ | $127.51 \cdot 10^{-4}$ | 0.635 | - |
| **Optimized** | $123.63 \cdot 10^{-4}$ | $4.07 \cdot 10^{-4}$ | $119.56 \cdot 10^{-4}$ | 0.635 | 172 primal<br>172 adjoint |
| **Change [%]** | -21.71 | -86.61 | -6.24 | 0.06 | - |

**Table 3.6: Optimization results of simultaneous shape optimization of entire aircraft using vertex-morphing**

An overall improvement of the far-field drag coefficient of 21.71% was reached. The improvement is due to both decrease of the induced drag and decrease of the wave drag. However, it has to be underline that the number of iterations needed for the optimization is very high (172 primal and adjoint CFD computations). It results in having a very high performing aerodynamic optimization on term of objective function reduction, but an unfeasible time-cost for preliminary design phase. Figure 3.18 shows the resulting surface pressure distribution of the baseline design (Figure 3.18(a)) and of the optimized designs introduced so far.

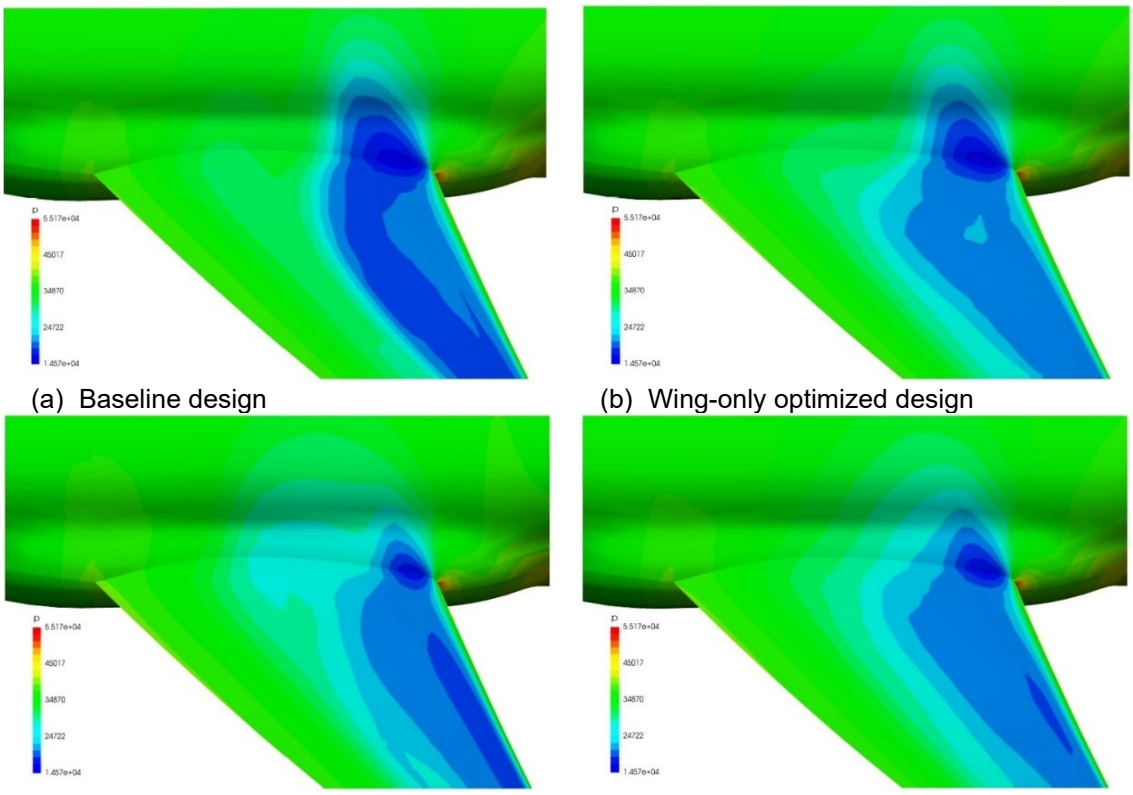

(a) Baseline design (b) Wing-only optimized design

(c) Sequential approach optimized design (d) Wing-body geometry optimized design

**Figure 3.18: Surface pressure for baseline and different optimized designs**

The reduction in the far-field drag in the last optimized case is a result of the very smooth pressure distribution as well as the alleviated shock regions. Particularly interesting is the single performance improvement from the wing-only optimization (Figure 3.18(b)) over the sequential approach (Figure 3.18(c)) to the shape optimization considering the entire wing-body geometry (Figure 3.18(d)).

#### 3.2.3.3 Aero-elastic multipoint optimization

An alternative approach is to consider a series of important design points and optimize a design for each of those in parallel. Multipoint objective functions are often employed within aerodynamic optimizations to prevent a reduction in off-design performance. This technique is popular throughout the literature where there are numerous examples of its application. *M. Nemec et al. (2004*) presented the aerodynamic shape optimization of single and multi-element airfoil configurations. *J. Szmelter* (*2001*) optimized a transonic wing for a combination of minimum drag and deviation from a target pressure at three different lift coefficients. *B. Epstein and S. Peigin* considered the multipoint optimization of an airfoil (*2004*), and *S. Peigin and B. Epstein* a business jet wing (*2007*) and a blended wing body aircraft (*2006*). *S Cliff et al.* (*2001*) considered single-point and multipoint shape optimization of a high-speed civil transport.

While effective at preventing off-design performance degradation, the utilization of a multipoint design strategy has some limitations. With each additional design condition considered the total number of simulations required for each geometry increases. Thus, typically only gradient-based optimization and response surface methods are practical (*D. J. J. Toal, A. J. Keane, 2011*). Moreover, if adjoint-based methods are chosen the adjoint calculation has to be done as much time as the number of points considered for the multipoint optimization.

For this work and for the MDO investigation introduced in Chapter 4, a three points optimization problem was defined. The objective function to be maximized is the algebraic sum of the lift over drag ratio at 3 $C_{L_i}$ conditions. The mathematical problem can be expressed as follows:

$$max\ J = {C_{L_1}}/{C_{d_{ff_1}}}(x_a) + {C_{L_2}}/{C_{d_{ff_2}}}(x_a) + {C_{L_3}}/{C_{d_{ff_3}}}(x_a)$$

$$wrt\ x_a$$

$$e.c.\ g = C_L - C_{L_i} = 0 \qquad (3.23)$$

$$R(U, x_a) = 0$$

Herein $C_{d_{ff_i}}$ represent the inviscid far-field drag coefficient and $R(U, x_a)$ the Euler equations in residual form. $x_a$ collets the aerodynamic design variable (global angle of attack, twist and camber at 6 control sections). The optimization workflow is shown in Figure 3.19.

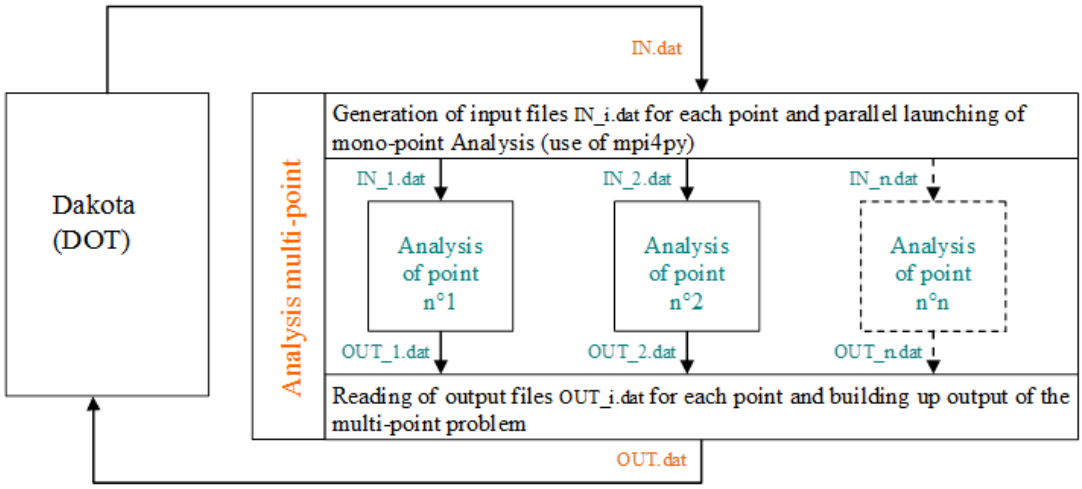


**Figure 3.19: Multipoint aero-elastic optimization workflow**

It has to be seen that the way the aero-elastic optimization problem has been expressed does not ensure a lift over drag ration maximization for every one of the analysis points, but it ensures only a global improvement.

## 3.3 Structural Optimization

The main aim addressed by the structural optimization was the primary structure weight reduction. As described in Chapter 2, Sec. 2.2.2, the in-house code InAirSsi (*I. Ghazlane, 2012*) has the capabilities to calculate the weight of the wing structure, perform sensitivity analysis and gradient-based optimization. The structural elements thickness was used as design variables to achieve weight minimization. Referring to Figure 2.26, the optimization parameters are 6 for each

control sections, with *n* control sections defined along the wing spanwise. Then, the structural variables $x_s$ for the structural optimization are 6**n* in total.

Formally, the structural optimization is expressed as follow:

$$\begin{aligned} &min\ J = W(x_s) \\ &wrt\ x_s \\ &i.c.\ KS < 0 \end{aligned} \tag{3.24}$$

A multiple of 2.5 time the cruise condition loads were taken as sizing load for the structural optimization performed during this work. A 2.5g manoeuvre load case should be assumed to be the sizing load for the wing structure. Unfortunately, the convergence of the aero-elastic evaluation that will estimate the aerodynamic load cannot be addressed, since the aforementioned manoeuvre load is obtained at a high angle of attack, which cannot be handled by the Euler solver. Nevertheless, the sizing load assumption does not affect the efficiency of the process that will be introduced later in this thesis.

The stresses of the structural elements are constrained so that the yield stress of the material is not exceeded. There are typically a lot of structural variables and it can become computationally very costly to treat these constraints separately. The problem is that there is no efficient method for computing sensitivities of many functions with respect to many design variables (*J. R. R. A. Martins, J. J. Alonso, 2002*). For this reason, the individual element stresses have been lumped using Kreisselmeier-Steinhauser (KS) function. Suppose that the constraint of each element is expressed as follow:

$$g_m = \frac{\sigma_m}{\sigma_y} - 1 < 0 \tag{3.25}$$

where $\sigma_m$ is the Von Mises stress and $\sigma_y$ is the yield stress of the material. The KS function is defined as:

$$KS(g_m) = \frac{1}{\rho}\ln\left(\sum_m e^{\rho g_m}\right) \tag{3.26}$$

This function represents a lower bound envelope of all the constraint inequalities (Eq. 3.25) and $\rho$ is a positive parameter that expresses how close this bound is to the actual minimum of the constraints. This constraint lumping method is conservative and may not achieve the same optimum that a problem treating the constraints separately would. However, the use of the KS function has been demonstrated and it constitutes a possible alternative in case of optimization problem with several constraints (*M. A. Akgün et al., 1999; N. M. K. Poon, J. R. R. A. Martins, 2005*).

InAirSsi was used to compute the sensitivities of the structural weight and the KS function with respect to the structural design variables. The sensitivities are computed analytically. The validation of the sensitivities is presented in (*I. Ghazlane, 2012*).

### 3.3.1 Impact of number and position of the control sections

An investigation on the impact of the number of the control sections and the relative spanwise positions on the optimum weight and on the number of iterations needed for the optimization process was undertaken. For this study, the structure was subjected to a constant bending load. Table 3.7 summarizes the investigation results.

| Beam nodes | Initial Weight [kg] | Optimum Weight [kg] | Optimizer Iterations |
|---|---|---|---|
| *3 equidistant control sections* | | | |
| 14 | 6459.6 | 5186.8 | 18 |
| 50 | 6459.6 | 5191.1 | 21 |
| *6 equidistant control sections* | | | |
| 14 | 6459.6 | 5068.8 | 18 |
| 50 | 6459.6 | 5071.9 | 25 |
| *11 equidistant control sections* | | | |
| 14 | 6459.6 | 5029.4 | 140 |
| 50 | 6459.6 | 5036.4 | 154 |
| *6 control sections, more discretization toward the wing tip (less-loaded wing side)* | | | |
| 14 | 6459.6 | 5352.2 | 23 |
| *6 control sections, more discretization toward the wing root (more-loaded wing side)* | | | |
| 14 | 6459.6 | 5030.2 | 16 |

**Table 3.7: Results of the investigation on number and position of the control sections for structural optimization**

As explained in Chapter 2, Sec. 2.3.1.1, the beam nodes are the points where the aerodynamic loads are transferred to the structure and they represent the structural discretization. The more the beam nodes are the more accurate the stress calculation is. Moreover, the more control sections are defined, the more structural variables are present, wider the design space is for the structural optimization. It is possible to see that as long as the control sections increase in number; the optimum weight decreases. This is true independently of the beam nodes. For 3 and 6 control sections, the number of evaluations needed to obtain the optimum is almost the same, while for 11 control sections it is one order of magnitude bigger. This result is in line with what *G. Carrier et al.* (*2014*) discussed, that is that with increasing number of parameters significant improvement can be obtained but also showed that an increasing design space results in convergence problems with the optimizer. It has to be underline that the more beam nodes are set the higher the time-cost of the structural stress and sensitivity evaluation is. Then, 14 beam nodes were chosen to discretize

the structure. Concerning the control section position, it is evident that while the number of evaluations is of the same order, the optimum weight results to be much better in case that the sections are closer to the wing root than to the wing tip. Moreover, in the first case the optimum weight is almost the same of the one obtained by using 11 equidistant control sections, but the number of evaluations is much lower. Thus, this discretization was adopted for the following studies. Actually, the control section positions were chosen in such a way that the distance between the section $i$ and the section $i+1$, from the wing root to the wing tip, is 1.5 time the distance between the section $i-1$ and the section $i$.

### 3.3.2 Consistent structural optimization

In order to have the structural optimization consistent with the change of the aerodynamic load while the stiffness of the wing structure is hanging (due to weight minimization), an iterative procedure has been put in place (*A. Viti et al., 2016*). In Figure 3.20, the iterative procedure for a consistent structural optimization is shown.

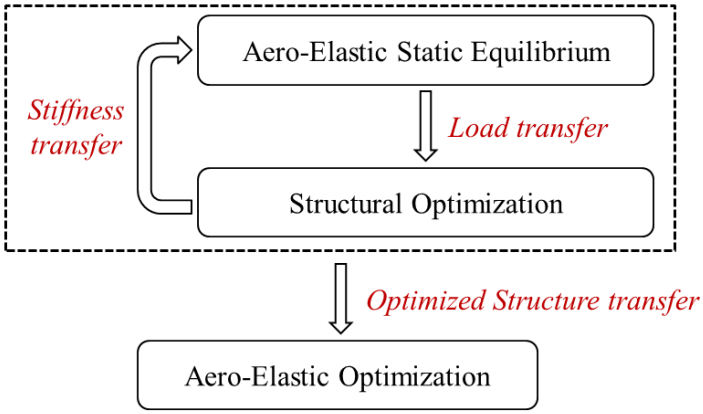


**Figure 3.20: Iterative procedure for a consistent structural optimization**

The process starts with a initial guess of wing structural element sizes from which the structural stiffness is evaluated. Using this information, a first aero-elastic evaluation at the above-mentioned cruise conditions has been run and the aerodynamic load has been used for the first structural optimization. Once the optimum is reached, the new wing stiffness is used for a new aero-elastic evaluation from which the new consistent aerodynamic load is gotten by the next weight reduction. The iterative procedure continues as long as the optimum weight of two consecutive structural

optimizations differs by a certain error. Figure 3.21 and Figure 3.22 represent the trend of the weight evolution during the consistent structural optimization of the BSW and FSW configuration respectively. Starting from a first element thicknesses guess (first red point, first weight evaluation, iteration number 1), the load distribution is computed and it will be constant during the first structural optimization which ends up to the second red point (second weight evaluation, iteration number 2). There, the new optimized structure is used in order to compute the new load distribution for the second structural optimization. Thus, the third red point is found and the procedure continues still the convergence is reached.

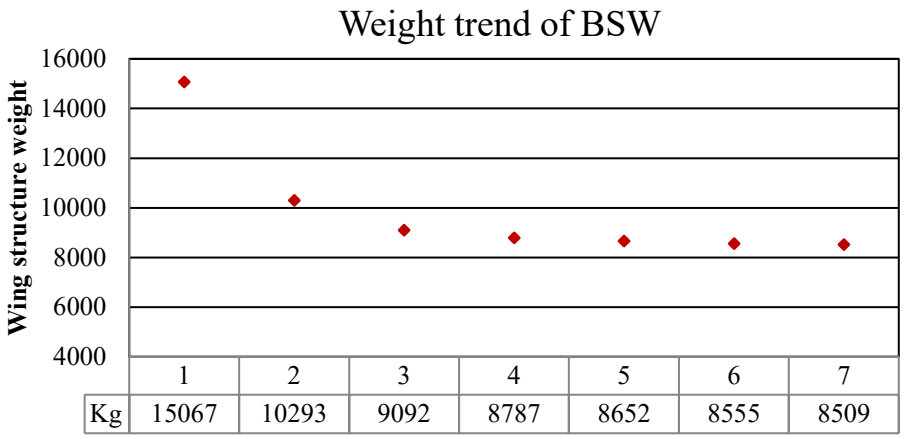


**Figure 3.21: BSW weight evolution during the consistent structural optimization process**

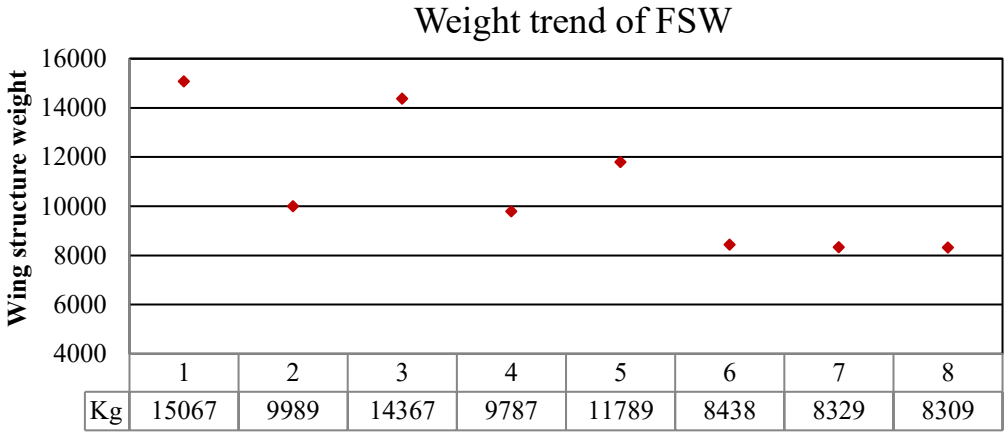


**Figure 3.22: FSW weight evolution during the consistent structural optimization process**

It is possible to notice that the two trends are very different since the one of the BSW monotonically decreases while the trend of the FSW weight oscillates until convergence. It is due to the fact that

the lighter (and then less stiff) the structure is the bigger the local twist is. For the two considered configurations the twists are opposite in sign since the BSW is characterized by a decreasing of the local angle of attack while an increasing for the FSW. In that way, the center of the pressure tends to move inboard for the BSW and then unload the structure, while the opposite for the FSW. Once the first aero-elastic evaluation is performed, the load distribution is kept constant during the first structural optimization and the stress constraints are calculated by considering this load. The new lighter structure will be less stiff than the previous one, and then the twist deformation will be bigger. In particular, during the second aero-elastic evaluation the BSW is characterized by an unloading of the structure due to the decreasing geometric angle of attack, while the FSW experiences an increasing of the local angle of attack and then a structural loading. This new aerodynamic load is kept constant during the second structural optimization and the new stress levels are evaluated on that. The starting point of this new structural optimization is the result of the previous structural optimization that was performed over the previous aerodynamic load. At the beginning of the second structural optimization the structural stiffness is the one of the previous optimization but the load and the stress level are different. In particular, the stress level of the BSW is smaller than the one of the previous structural optimization, while the stress level of the FSW is bigger. Then, for the BSW configuration the stress constrain is not violated, while for the FSW one results to be violated. Once the second structural optimization starts, the optimizer can decrease structural weight and then structural stiffness for the BSW case, while it has to add material and then structural stiffness for the FSW one. It ends up in a monotone weigh decreasing for the classical configuration and an oscillating weight behaviour for the unconventional architecture. Both optimizations reach the convergence but the FSW typically needs 1-2 iterations more.

This approach, together with the aero-elastic multipoint optimization approach, was used in the MDO approach introduced in Chapter 4, where aero-elastic and structural optimizations supported and enriched the overall aircraft design procedure of Airbus.

# Chapter 4

# Multidisciplinary Design Optimization: the Overall Aircraft Design

*This Chapter describes a preliminary aircraft design procedure in a multidisciplinary context for new aircraft configurations. In addition to the aero-elastic and structural optimization introduced in Chapter 3, the Overall Aircraft Design optimization was adopted in order to consider Direct Operative Cost reduction. Top level variables that directly impact both aerodynamics and structure were optimized in the above level, reducing the amount of information that the previous disciplines have to exchange. In fact, a new approach different from the classical aero-structural fully coupled system optimization is presented. Benefits and drawback of the methodology are underlined.*

## Contents

## Introduction

This study arises from the need to obtain a wide exploration of the design space during the initial aircraft design phases, and to use reliable physical results to provide valuable guideline to the more detailed design phases. The preliminary design is the phase in which the largest design freedom is present. It is characterized by a limited number of constraints, rapid and cheap evaluations but could be argued as the most critical part of the design process. Any decision taken in preliminary design has a significant impact in the following design process, leading to eventual modification which can typically be extremely expensive (*E. Torenbeek, 1982*).

Economic efficiency is the guideline for the new generation aircraft. Major airline companies aim at providing faster and cheaper connection to the rest of the world and their previsions are built up on new aircraft efficiency. Thus, the cost is the top level variable around which future development are designed. In the chapter an investigation of direct operative cost reduction is described, coupled with the aero-elastic and structural optimization process.

In this work the Overall Aircraft Design (OAD) analysis and optimization is part of a bi-level optimization strategy building on the aero-elastic and structural optimization procedure so that the top level variables (wing planform parameters) are optimized for cost reduction, and not for aero-structural needs alone. The OAD optimization targets the main wing variables that will be used as input for the further optimizations which will give back the sensitivity analysis of the aero-elastic and structural objective functions with respect to the OAD variables. At that point, cost reduction will be addressed again, and the process repeated until cost convergence is reached. This new procedure is introduced in Sec. 4.1.2.

Sec. 4.1 introduces the MDO approach, the current Airbus preliminary design procedure and the new optimization process that was developed in order to address design inconsistency when unconventional aircraft are considered. In Sec. 4.2 the application of the designed process on backward-swept wing (BSW) and forward-swept wing (FSW) configurations are shown, with particular interest on sensitivity analysis and optimization process convergence.

## 4.1 Multidisciplinary design optimization

Aircraft design involves a lot of different disciplines and one of the biggest difficulties is to integrate all these disciplines and the corresponding various requirements. It is most of the time a question of trades since requirements of a disciplines can be constraints for another, and this integration is the key part of the design. Figure 4.1 is a caricature that represents the ideal aircraft through each disciplines view.

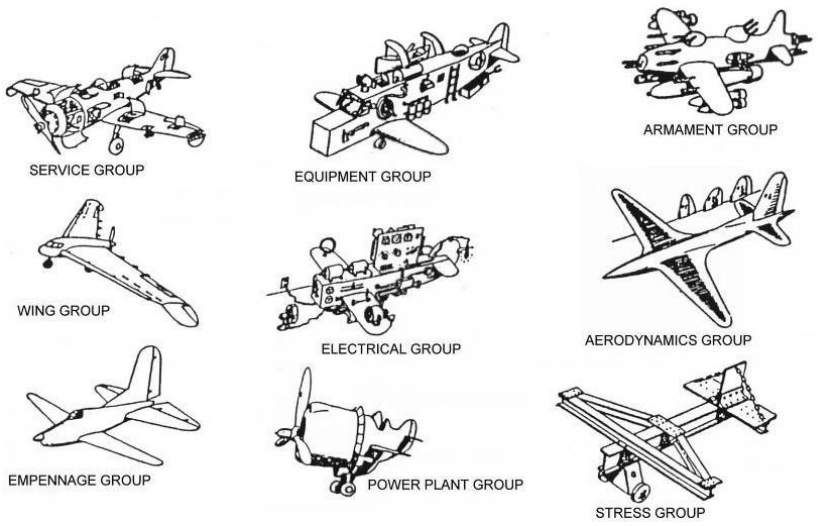


**Figure 4.1: Caricature of aircraft design depending on disciplines views *(S. Prigent et al., 2015)***

Multidisciplinary Design Optimization (MDO) can be defined as “a methodology for design of systems in which strong interaction between disciplines motivated designers to simultaneously manipulate variables in several disciplines (*J. Sobieszczanski-Sobieski, R. T. Haftka, 1997*). This statement undergoes the fact that independent optimization of individual disciplines considering local goals does not guarantee an optimum overall design, which requires the consideration of the synergies between each contributing analysis method (*S. Kodiyalam, J. Sobieszczanski-Sobieski, 2001*). *D. Neufeld* (*2010*) underlines how MDO provided methodology that can enhance the speed of the aircraft conceptual and preliminary design process, rapidly identifying the optimum design based on the simplified analysis methods typically used at the conceptual and preliminary level (*N. E. Antoine, 2004; D. Aronstein and K. Schueler, 2005; A. Striz, B. Kennedy, Z. Siddique, H. Neeman, 2006; A. Giunta, O. Golividov, D. Knill, B. Grossman, W. Mason, R. Haftka, 1997*).

In the literature, several papers describe industrial needs in Multidisciplinary Design Optimization, denoted as MDO, particularly concerning aerospace design. *J. P. Giesing* and J.-F. *Barthelemy* (*1998*) presents a summary of ten papers dealing with industry design processes, experiences and needs, with emphasis on the needs of industry in the area of MDO. Similarly, the paper of *S. Wakayama* and *I. Kroo* (*1998*) describes the optimization of a detailed design of a flying wing, and illustrates the numerous challenges to MDO use in industry. *T. A. Zang* and *L. L. Green* (*1999*) provided an overview of the MDO technology field from a fluid dynamics perspective, giving an emphasis to suggestions of specific applications of MDO approach that can enhance fluid dynamics research from basic flow physics to full configuration aerodynamics. The area of Multidisciplinary Design Optimization has growth to the point of gaining near universal recognition in its ability to lead to "better" design. Three definition of MDO are given by the *AIAA MDO Technical Committee* (*MDO Technical Committee, 2007*):

1. A methodology for the design of complex engineering systems and subsystems that coherently exploits the synergism of mutually interacting phenomena;
2. Optimal design of complex engineering systems which requires analysis that accounts for interacting amongst the disciplines (or part of the systems) and which seeks to synergistically exploit these interactions;
3. How to decide what to change, and to what extent to change it, when everything influences everything else.

Multidisciplinary optimization is often applied sequentially, with a certain parameters set by one discipline, and others assigned by the next discipline (*I. Kroo, 1995*). Generally, this approach does not lead to the optimal design of the complex system. According to *I. Kroo* (*1995*), Prandtl solved a problem of wing design using a coupled MDO procedure that treated structural sizing and aerodynamics concurrently. His solution yields 11% less drag at any selected structural weight than could be achieved using the sequential procedure (*L. Prandtl, 1933*). In support of that, *I. R. Chittick* and *J. R. R. A. Martins* (*2008*) and *J. R. R. A. Martins* (*2011*) show how coupled MDO is able to reach the optimum of a complex system, rather than sequential optimization (Figure 4.2).

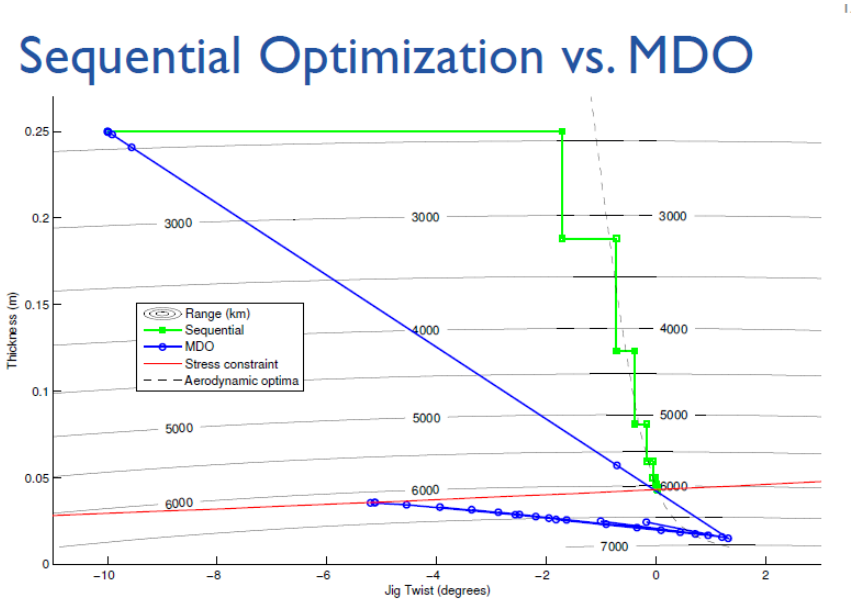


**Figure 4.2: Sequential multidisciplinary optimization vs coupled multidisciplinary optimization (*I. R. Chittick, J. R. R. A. Martins, 2008*)**

Several authors (*J. R. R. A. Martins, J. J. Reuther, 2002; G. K. W. Kenway, J. R. R. A. Martins, 2014; J. J. Alonso, I. M. Kroo, 2002; J. R. R. A. Martins, J. J. Alonso, 2001 and 2002; F. Flager, J. Haymaker, 2007; P. Piperni, M. Abdo, F. Kafyeke, 2007; A. DeBois, M. Abdo, 2010; P. Piperni, A. DeBlois, R. Henderson, 2013*) showed the efficiency and reliability of coupled aero-structural optimization, ending up with results never explored if uncoupled methods are put in place. Their approach is extremely powerful and high-fidelity if aerodynamic and structural needs have to be addressed, but it could be very complex for preliminary design purposes. Actually, some top level variables used in the coupled aero-structural optimization are strictly correlated to the direct operative cost of an aircraft, but adding those evaluations and optimization to the aero-structural approach could be very expensive. For that reason, the approach presented in this chapter was designed to be less coupled but more flexible in term of preliminary design applicability.

### 4.1.1 MDO process in Future Project Office: The Overall Aircraft Design

The design specification of a commercial transport aircraft is a complex process (*M. Pacull, 1990; E. Torenbeek, 1982*) because of industrial aspects, of the increasing number of involved partners in a current engineering process, or because safety constraints. This section is devoted to the representation of the models and processes of aircraft preliminary design of Airbus Future Project Office. A complete description of the model can be found in (*J. Birman, 2013; C. Badufle,*

*2007; S. Prigent et al., 2015*). Preliminary aircraft design is the first step in the passenger transport aircraft design process. The objective for engineers is to find, among all the possible aircraft configurations, the “best” one that fulfils the requirements while optimizing the selected criteria – essentially, maximizing/minimizing an object subject to constraints – .

The goal is to choose, among several concepts, the one which would be relevant according to a well define objective (cost, fuel consumption or environmental impact). For each concept, the main aircraft parameters have to be assessed consistently according to a common set of requirements. Figure 4.3 represents, in a simple way, the process which leads to this “best” aircraft configuration.

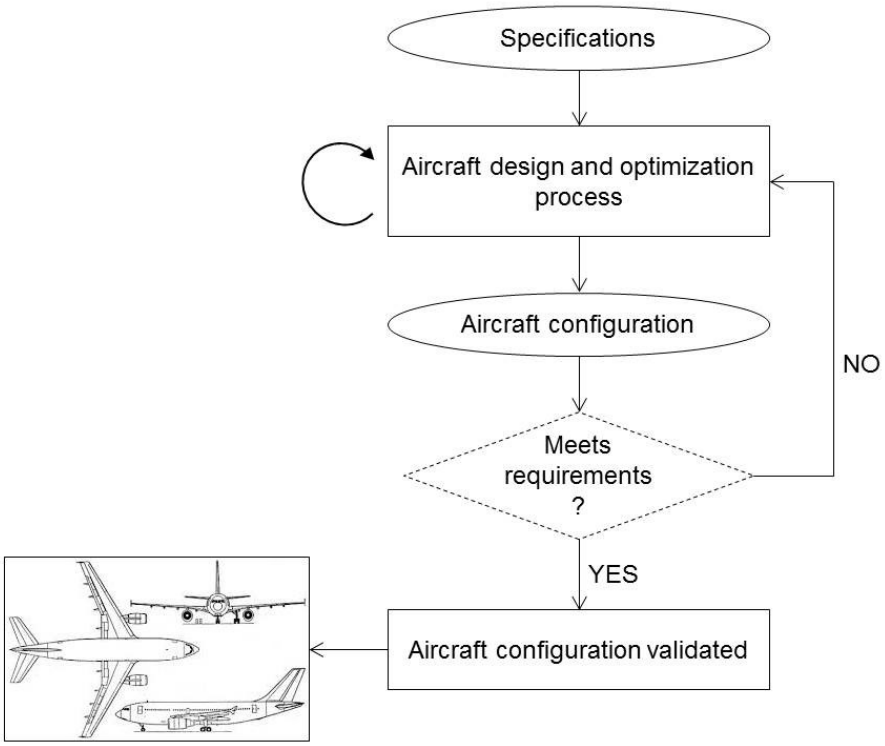


**Figure 4.3: Process for future project conception (*J. Birman, 2013*)**

#### 4.1.1.1 Specifications

Top Level Aircraft Requirements (TLARs) are supposed to be the fundamental requirements that will give shape to the future aircraft. They form the specifications and are the input of the design process. A wrong set of TLARs may drive to an unfeasible aircraft or economically not viable. The OAD role is to select those TLARs by considering the requirements coming from three entities:

environment, airline and manufacturer. A focus on that can be found in (*C. Badufle, 2007*). The set of requirements retained for this study are shown in Table 4.1.

| | | |
|---|---|---|
| Design Range | [NM] | 3000 |
| Total number of Passengers | [-] | 270 |
| Cruise Mach Number | [M] | 0.75 |
| Initial Cruise Altitude | [ft] | 35000 |
| Number of Engines | [-] | 2 |
| Take-Off Field Length | [m] | 2180 |
| Climbing Speed | [ft/min] | 500 |
| Time to Climb | [min] | 20 |
| Landing Speed | [kt] | 134.5 |
| Approach Speed | [ft/min] | 300 |

**Table 4.1: Top Level Aircraft Requirements (TLARs)**

When defining a new aircraft, the designers want it to be the least expensive, the fastest, the most comfortable and also the simplest, the lightest, having the best aerodynamic design. But one cannot make everything best at once, so that the best overall airplane is always a compromise. The compromise is made in a rational way, provided the right measure of the aircraft quality is used. Maximum Take-Off Weight (MTOW) has always been a significant parameter used to represent the aircraft quality because it has a direct impact on costs. But with the increase of fuel price, MTOW is not as relevant as it used to be. Currently, Direct Operating Cost (DOC) provides a more accurate representation of the aircraft quality because it integrates in the same variables the impact of fuel cost, maintenance, crew, taxes, etc (*C. Badufle, 2007*). The DOC is the parameter chosen for this work in order to optimize the overall aircraft design (Sec. 4.2.3).

#### 4.1.1.2 Aircraft design and optimization process

In general, designing and defining an initial topology of an economical and physical system is a five steps process:

i. Defining fundamental variables modelling the essential behaviour of the system;
ii. Building a model accurate enough to allow a reliable representation of the variables influence on the overall system;
iii. Defining a mean to measure the quality of the system which depends on these variables;
iv. Translating TLARs into operational constraints, or into imposed values of the design parameters;
v. Chose variables values which correspond to an optimal behaviour of the system, while ensuring the system meets requirement constraints.

The *wing area* and the *engine thrust* are the most sensitive parameters acting on the aircraft performances (*S. Prigent et al., 2015*). But some other parameters are also of importance, such as the wing sweep angle or the wing span and can be degrees of freedom of the optimization. In this work, 7 top level variables were chosen to undertake the optimization, while the sensitivities of only 6 of them are used to increase the reliability of the OAD Airbus model, as explained in Sec.4.2.2. Each discipline that define the multidisciplinary aircraft design such as geometry, aerodynamics, structural weight, propulsion, is described by semi-empirical models built up from physical law and from a database of around 60 aircraft. A complete description of these models can be found in (*J. Birman, 2013; S. Prigent, 2015*). The models are organized into a multi-layered toolbox: the lower layer contains theoretical and semi-empirical models to design aircraft components such as fuselage, wing, etc, and the higher layer contains processes for the OAD optimization. The Airbus OAD optimization process is illustrated in Figure 4.4 (*S. Prigent, 2015*). Traditionally, the process is based on deterministic optimization and the aim is to look for the best coupling of *wing area* and *engine thrust* that minimize *MTOW* and satisfy operational requirements (Table 4.1). As mentioned before, in this work 7 design parameters were considered (Table 4.2, Sec. 4.1.2) and DOC was minimized. The process is clearly multidisciplinary and it is possible to distinguish at least five disciplines: geometry, propulsion, aerodynamics, weight and performances.

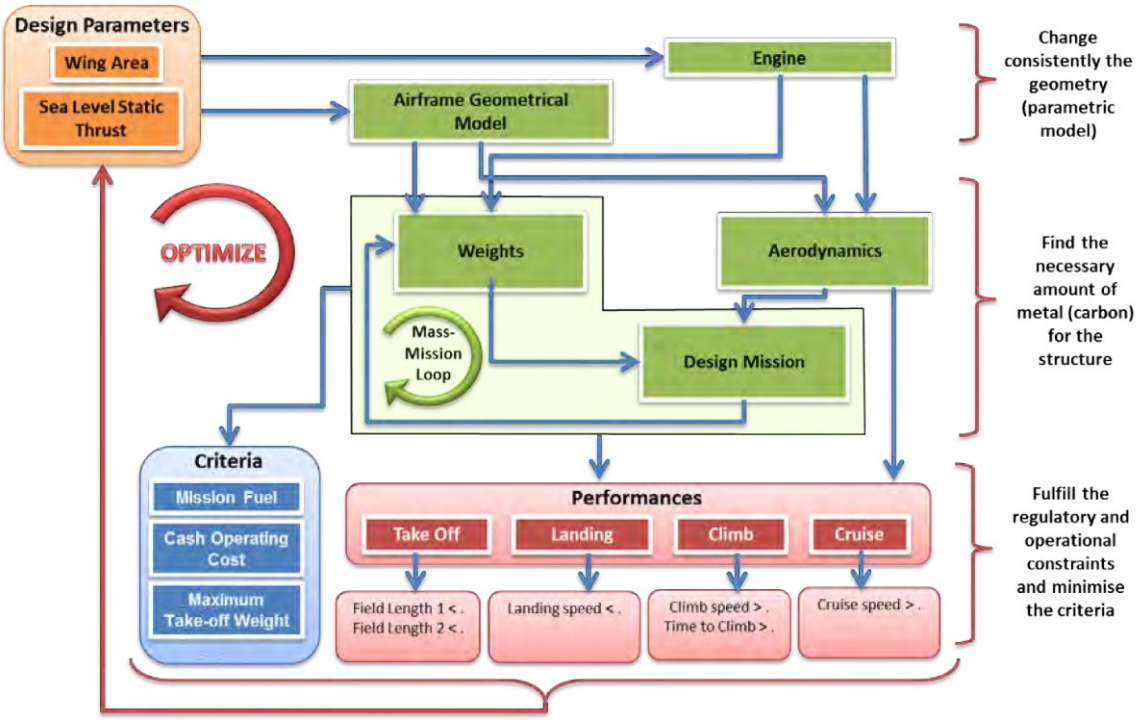


**Figure 4.4: Traditional Airbus OAD analysis and optimization process (*S. Prigent, 2015*)**

The first step of the process is the definition of the aircraft geometry. From the design parameters it is possible to drive the entire shape of the aircraft through parametric models. The models are based on similarity with other aircraft of the same family as the one described by the design parameters. During the process, in parallel with the geometry, the engine parameters are computed. The objective of the engine model is to compute the fuel consumption, the thrust and the mass of the engine as function of the flight conditions (Mach, altitude, air temperature, etc). Once the engine and geometry of the aircraft are considered, the next step of the process is the computation of the aerodynamics. There, the drag is computed as function of the required lift and of the flying conditions. The following step is to compute the weight and the mission by running the *mass-mission loop*. This process is iterative and the mission requires the weight to be computed, but the weight also requires the amount of fuel and so the mission. The mass-mission loop is the process used to compute the MTOW of an aircraft in accordance with the nominal payload and the nominal operational range. Starting with hypothetic weight it is possible to solve the mass-mission loop process to obtain what is called a converged aircraft, satisfying mission and structural weight requirements. Thus, MTOW calculation encompasses two aspects: fuel consumption aspect and

structural aspect. From the mission requirement point of view, the mission model is necessary to compute the fuel over a given mission. It yields the following equation:

$$OWE = MTOW - Payload_{nom} - Fuel_{nom} = f(MTOW) \quad (4.1)$$

Where OWE is called Operator Weight Empty and $Payload_{nom}$ and $Fuel_{nom}$ are the payload and fuel of the design mission. From a structural aspect and from the weight model, OWE can be only computed by knowing MTOW, then $OWE = g(MTOW)$ . To illustrate the mass-mission loop the two functions can be drawn in a graph (Figure 4.5):

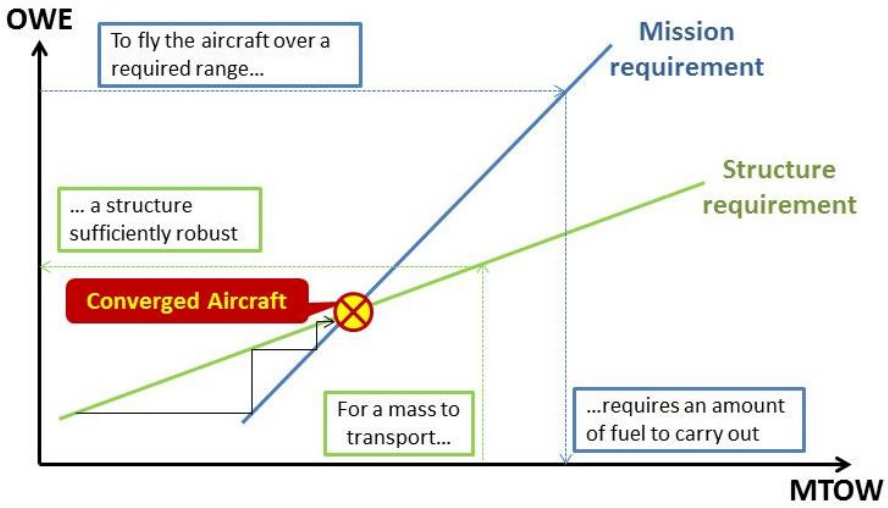


**Figure 4.5: Aircraft design Mass-Mission loop**

For a given OWE to fly over a given mission, the required MTOW can be read from the blue line. For a given MTOW, a strong enough structure leads to the OWE that can be read from the green line. At left of the intersection of the two lines, the LTOW is not sufficient to complete the mission and at the right the MTOW is exceeding the required one according the OWE: the aircraft is overweighted (*S. Prigent, 2015*). The last part of the OAD optimization process is the computation of the performances and criteria. The performances are the constraints that have to be satisfied during the optimization process, while the chosen criterion that identify the goodness of the design represents the objective function to be minimized. As mentioned before, the DOC is the criterion chosen during the following investigations.

### 4.1.2 New multidisciplinary design optimization procedure for unconventional aircraft

The Airbus OAD preliminary design procedure is then based on semi-empirical models extracted by regression of around 60 aircrafts. The procedure is very efficient for classical aircraft preliminary design, while results are likely to be less accurate for unconventional aircrafts are considered (*S. Prigent, 2015*). Since any simulation of the physics of the aircraft is undertaken, the Airbus OAD procedure is not able to consider any phenomena but the classical aircraft ones. For this reason, the new MDO-OAD process aims at introducing light multidisciplinary evaluations since the preliminary design phase, in order to allow to the OAD optimization to have more physical feedback from the studied aircraft configuration.

Two optimization levels are considered:

- Top level OAD optimization for economic efficiency, formally expressed as follows:

$$\begin{aligned} &\textit{min } J = DOC\,(x_{TLV}) \\ &\textit{wrt } x_{TLV} = Top\ Level\ Variables \\ &\textit{e.c. } Performances \end{aligned} \tag{4.2}$$

- Aero-elastic and structural optimization for drag and weight reduction, formally expressed as Eq. 3.23 and 3.24.

Those two optimisation levels exchange information in such a way that both are consistent with the each other geometry changes.

First of all, the top level variables (TVL) which guide the cost reduction have to be defined. Costs, such as Direct Operative Cost (DOC), are fully dependent on wing platform variables, and almost all of those directly impact on both aerodynamics and structure. Thus, the top level variables that are used by the OAD optimization for DOC reduction are shown in Table 4.2.

| | |
|---|---|
| Sea Level Static Thrust | $\boldsymbol{SLST}$ |
| Wing Surface | $\boldsymbol{S}$ |
| Aspect Ratio | $\boldsymbol{AR}\ \left(= {\boldsymbol{b^2}}/{\boldsymbol{S}}\right)$ |
| Taper Ratio | $\boldsymbol{TR}\left(= {\boldsymbol{C_{tip}}}/{\boldsymbol{C_{root}}}\right)$ |
| Sweep Angle | $\boldsymbol{\varphi_{25\%}}$ |
| Relative thickness at 40% of the span | $\boldsymbol{t/c}\big\vert_{\boldsymbol{40\%}}$ |
| Relative thickness at the tip | $\boldsymbol{t/c}\big\vert_{\boldsymbol{tip}}$ |

**Table 4.2: Top level variable for the OAD optimization**

Apart from the first variable that describes the engine size, it can be seen that the chosen top level variables are those for which there is a strong aero-structural coupling. This condition is the driver of the choice. If those variables will be used for single discipline optimization (aero-elastic or structural one) and no information from the other discipline is considered, the result will be optimal for one discipline but deleterious for the other. Then, such variables will be not considered during the single discipline optimization in order to reduce the error of not considering cross-sensitivity, but they will be optimized during the top level OAD optimization. Actually, they may be not the only variables to strong couple the two disciplines, and an investigation should be made to identify, by testing, further variables to increase the results quality. The proposed approach has the additional industrial implementation benefit where main disciplines belong to independent departments since the coupling variables are chosen at higher economical level. Following the suggested approach, the aero-structural problem will be led by OAD top level considerations which will guide the choice of top level wing geometrical parameters.

The proposed *OAD – Aero-elastic – Structural* optimization procedure is then organized in such way that each discipline is independent but requires information from the previous optimization level. After having generated the aircraft benchmark, and then the initial value of the top level variables, based on the top level aircraft requirements of Table 4.1 by using the nowadays Airbus OAD optimisation (Figure 4.4), the optimization workflow proceeds as follows (Figure 4.6):

*i.* Multipoint aero-elastic and structural optimizations of the aircraft described by the initial values of the top level variables (that are frozen during this phase), and sensitivity analysis of the objective functions (induced/wave drag and structural weight for the aero-elastic and the structural optimization respectively) with respect to the top level variables;

*ii.* Enrichment of the OAD aerodynamic and structural models by using the abovementioned sensitivity (Sec. 4.2.2) in order to perform a more reliable DOC minimization and to obtain a new optimized set of top level variables;

*iii.* New multipoint aero-elastic and structural optimizations of the new aircraft based on the new set of top level variables (that, again, are frozen during this phase), and sensitivity analysis;

*iv.* Further enrichment of the OAD aerodynamic and structural models, then new DOC minimization to obtain a new optimized set of top level variables, and again with aero-elastic and structural optimization until reaching the convergence of the DOC (top level optimisation objective function).

The stopping criteria of the MDO-OAD procedure is when two sequential DOC optimization differs from each other by a certain error $\varepsilon$.

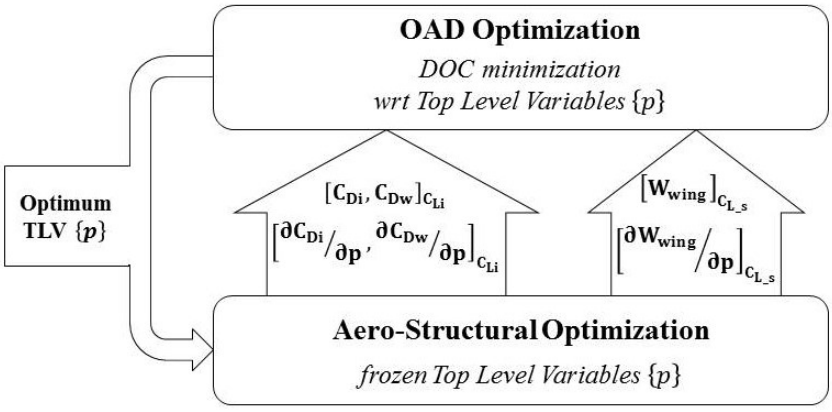


**Figure 4.6: MDO-OAD preliminary design procedure**

## 4.2 Application of the procedure to conventional and unconventional geometries

The MDO-OAD procedure was developed in order to have a more reliable preliminary design of unconventional aircraft. In order to understand benefits and drawbacks, the procedure was applied on the FSW configuration and on a classic BSW architecture. The BSW configuration was derived from the FSW one by keeping the same sweep angle module, but opposite sign. Figure 4.7 shows the considered geometries.

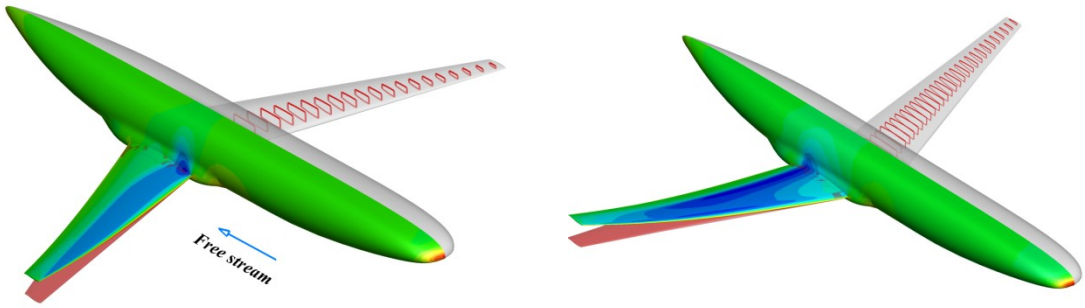


(a) FSW architecture (b) BSW architecture

**Figure 4.7: Studied aircraft configurations**

Following the procedure described in Sec.4.1.2, the new preliminary design approach is applied to the chosen test cases.

### 4.2.1 Geometry and benchmark identification

The identification of a common aircraft benchmark on which the benefits of the methodology are evaluated has been done by using the aircraft manufacturer's historical data. As described above, in order to describe typical civil aircraft architecture the BSW configuration was generated. In Figure 4.8 the configuration is shown.

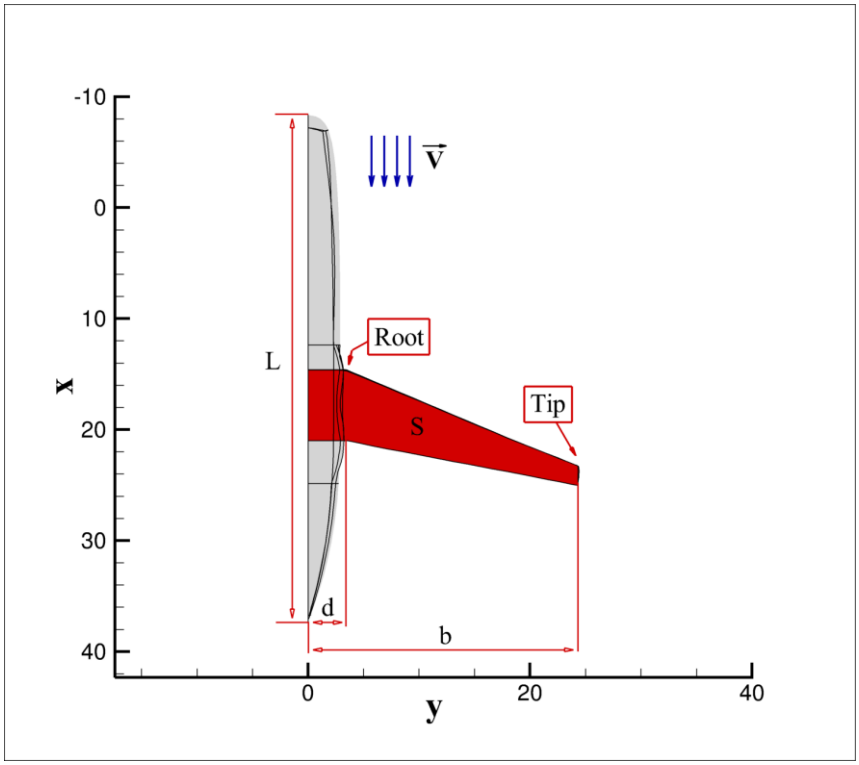


**Figure 4.8: Planform of the configuration**

The BSW geometry is the base for the benchmark definition. The benchmark should be related to the state-of-art of classical preliminary design approach, so a pure OAD design procedure was applied (without MDO physical enrichment). The values of 5 out of 7 top level variables were set in the preliminary design tool, while the range of the aircraft mission together with the cruise Mach number, the altitude and the payload were defined in accordance with same category aircraft. The wing surface was not fixed since it is an optimization variable for the original Airbus OAD procedure, together with the sea level static thrust (Sec.4.1.1, Figure 4.4). The resulting wing surface will be the benchmark wing surface and the resulting DOC will be compared with the one which will be obtained after the multidisciplinary procedure. The theoretical and semi-empirical models used by the OAD tool give a first definition of the physics of the system (the cruise condition $C_L$ is one of the outputs of this OAD optimization). Below, the value of the dimensions and the cruise conditions of the benchmark are summarized in the tables below.

| | |
|---|---|
| Fuselage length $\boldsymbol{L}$ [m] | 46.65 |
| Semi-span $\boldsymbol{b}$ [m] | 21.9 |
| Root position $\boldsymbol{d}$ [m] | 3.3 |
| Root chord $\boldsymbol{C_r}$ [m] | 6.225 |
| Tip chord $\boldsymbol{C_t}$ [m] | 1.772 |

**Table 4.3: Aircraft dimensions (ref. Figure 6.8)**

| | |
|---|---|
| Wing semi-surface $\boldsymbol{S}$ [m$^2$] | 97.503 |
| Sweep angle $\boldsymbol{\varphi_{25\%}}$ [°] | 18.15 |
| Aspect ratio $\boldsymbol{\lambda}$ [-] | 9.93 |
| Taper ratio $\boldsymbol{C_{tip}/C_{root}}$ [-] | 0.2697 |
| Relative thickness at 40% of the span $\boldsymbol{t/c}\big\vert_{\boldsymbol{40\%}}$ [-] | 0.14136 |
| Relative thickness at the tip $\boldsymbol{t/c}\big\vert_{\boldsymbol{tip}}$ [-] | 0.114087 |

**Table 4.4: Values of the 6 top level parameters**

| | |
|---|---|
| Lift coefficient $\boldsymbol{C_L}$ [-] | 0.635 |
| Mach $\boldsymbol{M}$ [-] | 0.75 |
| Altitude $\boldsymbol{h}$ [ft] | 35000 |
| Design range $\boldsymbol{R}$ [NM] | 3000 |
| Payload $\boldsymbol{PL}$ [Passengers] | 270 |
| Direct Operative Cost $\boldsymbol{DOC}$ [$/trip] | 16452 |
| Maximum Take-Off Weight $\boldsymbol{MTOW}$ [kg] | 122231 |

**Table 4.5: Cruise conditions and mission characteristics**

The *virtual* aircraft geometry of Figure 4.9 will be used later to evaluate the progresses the multidisciplinary approach can achieve.

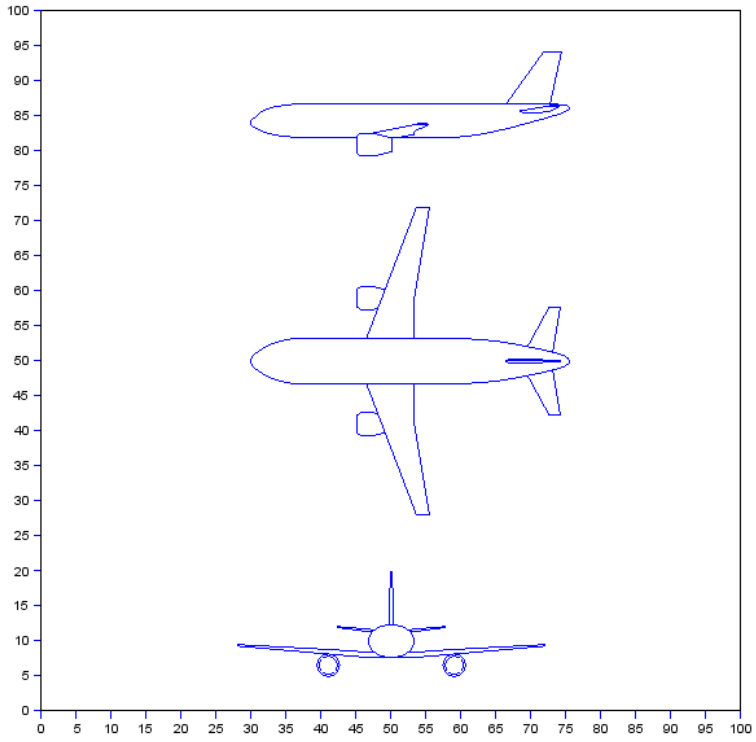


**Figure 4.9: 3 views sketch of the benchmark (units in *meter*)**

Since any enrichment of the models that describe the physics of the aircraft was done for the generation of the benchmark, the OAD procedure is sensitive only to the absolute value of the sweep angle. Then, if negative sweep angle is considered, dimensions and cruise condition of the FSW benchmark will not change (Table 4.3, 4.4, 4.5).

Using the Airbus OAD database a conventional aircraft was defined, and it is characterized by the same technological level of current aircraft families. The aero-structural optimization addressed efficiency needs and enriched the overall design procedure by adding physical information to the statistical model which Airbus has been using since long time. In particular, the multipoint aero-elastic optimization was used to increase the $C_L/C_D$ ratio in cruise conditions and in the off-design neighborhood. For that purpose, 3 points of the aircraft polar were chosen, respectively the lift coefficient in cruise conditions, +0.05 and -0.05 to it. The structural optimization was used to increase the structural efficiency of the primary wing structure subjected to cruise condition lift load.

### 4.2.2 Sensitivity analysis and OAD enrichment

After the benchmark definition, aero-elastic and structural optimization were performed in order to increase the aircraft aero-structural efficiency. Referring to Figure 4.10 (as detail of Figure 4.6):

i. the aero-structural optimization procedure started with the consistent structural optimization (Chapter 3, Sec. 3.3.2):
   - the benchmark gives the first set of top level variables that were fixed during this design step. The first sizing load was calculated by performing an aero-elastic simulation of the benchmark ($TLV_b$);
   - then, following the consistent structural optimization procedure, the optimum weight related to the first set of top level variables was obtained under the sizing load;

ii. the resulted optimized structure $x_{s\_opt}$ were then used to perform the forthcoming multipoint aero-elastic optimization (Chapter 3, Sec. 3.2.3.3). This optimization aims at increasing the aerodynamic efficiency at the cruise conditions and in its neighborhood. The objective function to be maximized is the algebraic sum of the $C_L/C_D$ ratio referred to 3 points of the aircraft polar, respectively the lift coefficient in cruise conditions, +0.05 and -0.05 to it. The $C_L$ in cruise condition is an output of the OAD optimization, then the first one used for the first multipoint aero-elastic optimization was the benchmark one;

iii. once the aero-structural optimization procedure (Figure 4.10) was completed, the sensitivity analysis and the OAD aerodynamic and structural model's enrichment took place and a new OAD optimization minimized the DOC while optimizing the top level variables (Figure 4.6);

iv. the sizing load to start the next consistent structural optimization was calculated by performing an aero-elastic simulation of the new aircraft corresponding to the new set of top level parameters. The new $C_L$ conditions were used as equality constraints for the next multipoint aero-elastic optimization.

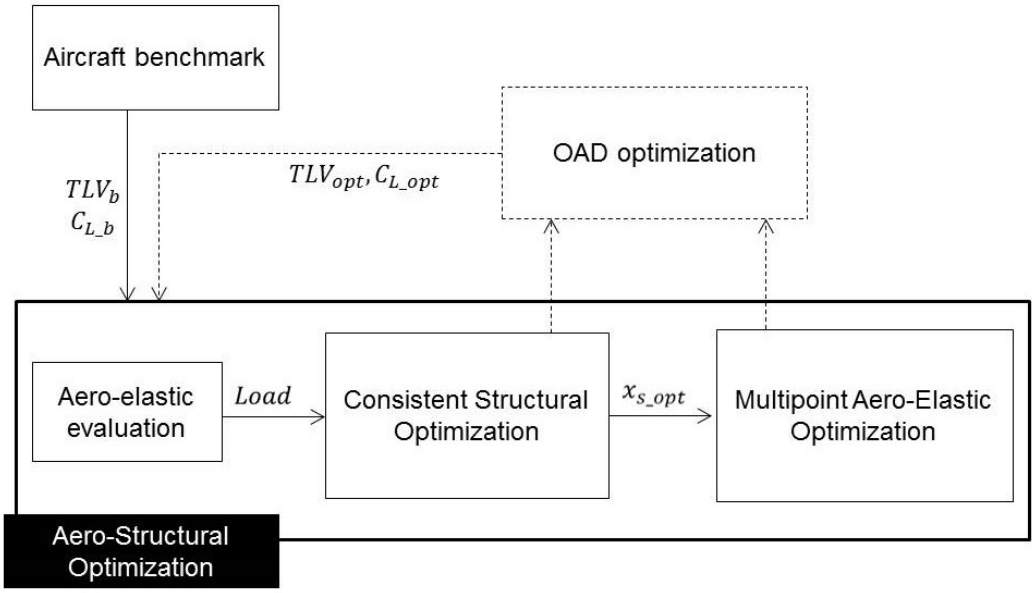


**Figure 4.10: Detail of the aero-structural procedure of Figure 4.6**

Values of the $\boldsymbol{C_{Di}}$ and $\boldsymbol{C_{Dw}}$ at the 3 different cruise conditions (coming from the multipoint aero-elastic optimization) and the value of the $\boldsymbol{W}$ (coming from the consistent structural optimization) of the optimized configuration are then used in the OAD optimization process. Those values, together with their sensitivity with respect to the top level variables, were used to estimate more reliable aerodynamic force and structural weight of the considered configuration. In particular, a new aircraft polar was generated by using a polynomial function to interpolate the drag at the 3 cruise conditions. Calling $\boldsymbol{p}$ the 6 top level variables that were used for the enrichment of the OAD models (Table 6.2, without the *SLST*) and $\boldsymbol{C_{L\_j}}$ the 3 lift conditions for which the multipoint aero-elastic optimization was performed, the following sensitivities were evaluated: $\boldsymbol{\partial W/\partial p}$, $\boldsymbol{\partial C_{Di}/\partial p}\big|_{C_{L\_j}}$, $\boldsymbol{\partial C_{Dw}/\partial p}$.

To better explain this procedure, consider the induced drag: $\boldsymbol{C_{Di}}$. The preliminary design tool calculates that using the lifting line theory of Prandtl:

$$C_{Di} = C_L^2/\pi AR \tag{4.3}$$

The enriching approach aims at improving the polar evaluation by using 3 points calculated in a more reliable way than lifting theory (Figure 4.11).

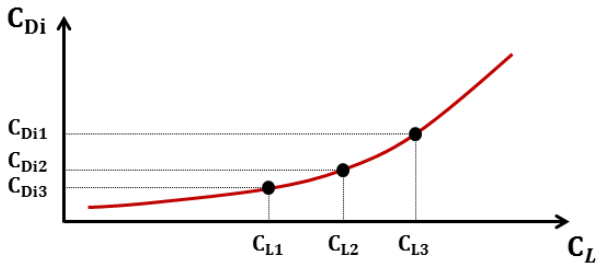


**Figure 4.11: Polar estimation over 3 points**

These points are evaluated by taking into consideration the induced drag of the optimized aircraft and its sensitivity with respect to the 6 top level OAD variables used for the enrichment. The polar will be a polynomial function that interpolates those 3 points. The 3 $C_{L\_j}$ conditions are the 3 conditions of the aero-elastic multipoint optimization. The final expression is the following:

$$C_{Di\_j} = C_{Di\_j}\big|_{opt} + \sum_{6} \frac{\partial C_{Di\_j}}{\partial p} \Delta p, \quad j = 1,2,3 \tag{4.4}$$

$$C_{Di} = pol.func\left(C_{L\_j}, \frac{\partial C_{Di\_j}}{\partial p}\right), \quad j = 1,2,3 \tag{4.5}$$

Eq. 4.4 represents the way of calculating the induced drag at specific $C_{L\_j}$ conditions by using information coming from the optimized configuration and the sensitivity analysis, while Eq. 4.5 represents the evaluation of the new aircraft polar. The same approach was used for the wave drag and for the primary wing structure weight. New response surfaces for aerodynamic and structural properties are then generated that substitute the semi-empirical ones of the original OAD models and then used for the top level OAD optimisation. In that way, the OAD evaluation was enriched by physical phenomena, ending up with a more reliable OAD optimization for DOC reduction.

#### 4.2.2.1 On the sensitivity analysis: correction of the objective function sensitivity with violated constraints.

One of the key points of this approach is the sensitivity calculation of the aerodynamic and structural objective functions with respect to the top level variables. To evaluate them, two ways are possible:

1. To perturb the variables and detect the variation of the objective function without considering the constraint sensitivity, and then considering the following expression:

$$\frac{dOF}{dp} \approx \frac{\partial OF}{\partial p}\Big|_{opt} \tag{4.6}$$

2. To consider the variation (and violation) of the constraint to correct the objective function sensitivity:

$$\frac{dOF}{dp} \approx \frac{\partial OF}{\partial p}\Big|_{opt} + \lambda_c \frac{\partial C}{\partial p}\Big|_{opt} \tag{4.7}$$

where $\lambda_c$ is a multiplier evaluated by projecting the objective function gradient in the constraint gradient space.

Table 4.6 shows the values of the structural sensitivity of the BSW configuration evaluated by using the abovementioned correction and not. $^{\partial KS}/_{\partial p}$ is the constraint sensitivity, $^{\partial W}/_{\partial p}$ is the objective function (weight) sensitivity without correction and $^{dW}/_{dp}$ is the corrected objective function sensitivity.

| ***Structure*** | **Sweep** | **Surface** | **AR** | **TR** | **Thick 40%** | **Thick Tip** |
|---|---|---|---|---|---|---|
| $^{\partial KS}/_{\partial p}$ | 0.0002 | -0.0080 | 0.0730 | 0.3736 | -6.9169 | -0.8921 |
| $^{\partial W}/_{\partial p}$ | -3.4408 | 47.861 | -291.46 | 433.38 | 27637.3 | 10419.9 |
| $^{dW}/_{dp}$ | -2.5698 | 12.713 | 29.153 | 2040.0 | -726.55 | 6502.7 |

**Table 4.6: Structural sensitivity of the BSW configuration**

It is possible to see that by considering the constraint sensitivity, the sensitivity of the objective function changes a lot. In order to evaluate such a difference, let's focus on the sensitivity with respect to the thickness at the 40% of the span. In general, as soon as the thickness of a wing section increases its inertia increases as well. Conversely, an increasing of weight is a consequence. The inertia of a section increases faster than its weight due to the thickness increases. As consequence, the structural stress level of the wing section decreases faster than the increasing weight. Thus, designing the structure while keeping the stress level constant implies that an increasing of wing section thickness ends up with a decreasing in weight. The weight sensitivity with respect to the thickness at 40% of the span results to be positive if the constraint

sensitivity is not considered, while it is negative when the correction is applied. In fact, it is possible to see that the constraint sensitivity is highly negative and that means that the stress level of the structure massively decreases while the thickness increases. By considering that, reliable weight sensitivity can be found. It is important to recognize that the corrected weight sensitivity calculated with respect to the tip thickness is still positive. That is due to the fact that the constraint sensitivity is not that negative since the tip of the wing is weakly loaded. The sensitivity correction is then chosen in order to have a more reliable sensitivity evaluation.

The sensitivity with respect to the top level parameters was performed by using the finite differences technique. This choice was led to the fact that the adjoint formulation of such sensitivity was not able to give reasonable results, potentially because of a particular behaviour of the mesh deformation tool that was used. It was also unnecessary due to the small number of design variables. A deep investigation was undertaken to define the right perturbation amplitude for the finite differences. Figure 6.12 shows the step length investigation to calculate the sensitivity of the aerodynamic coefficients with respect to the top level variables. It is possible to notice that, while is easy to find a *plateau* for induced drag sensitivity and then a range of usable step length, the wave drag sensitivity behaviour is much less smooth. The wave drag sensitivity is more sensible to the finite difference step length than the induced drag sensitivity and it is usually more difficult to predict the wave drag behaviour than the induced drag one. Thus, non-uniformities of the wave drag sensitivity over the step length change are difficult to judge as physical or unphysical ones. However, step length of $10^{-5}$ time the top level variable values was considered as proper value for the sensitivity analysis. The same investigation was undertaken for the structural weight sensitivity, which behaviour resulted to be very smooth and then easy identification of the *plateau*. $10^{-5}$ was considered a good value of the step length for structural sensitivity too.

Sensitivity of $C_{Dw}$ vs FD step lenght

Sensitivity of $C_{Di}$ vs FD step lenght

*Surface*

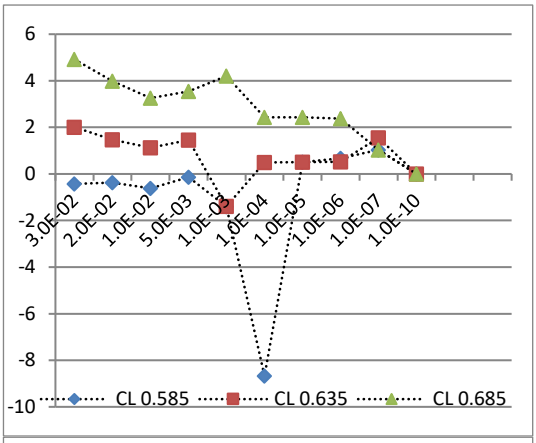


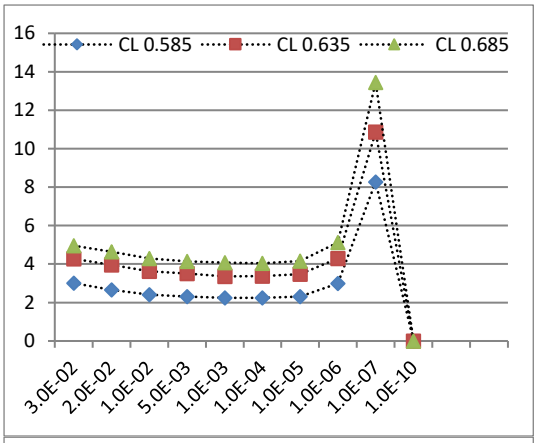


*Aspect Ratio*

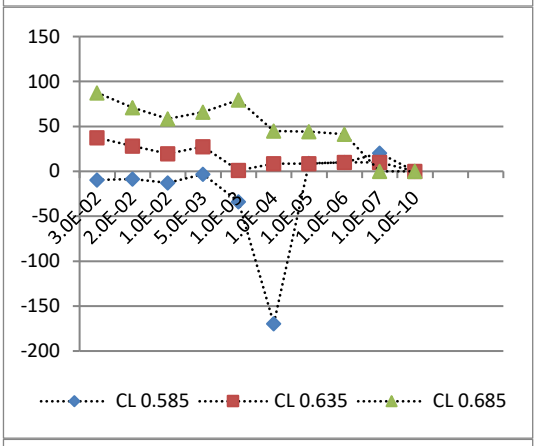


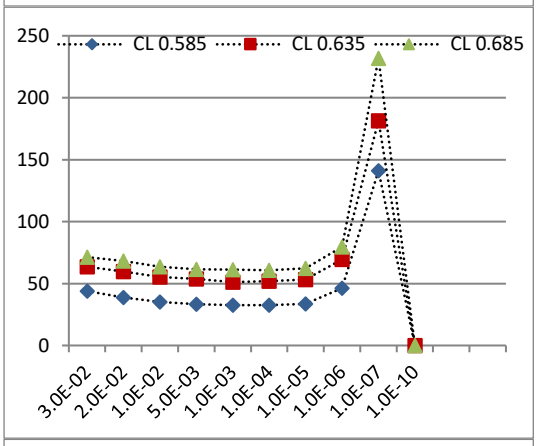


*Taper Ratio*

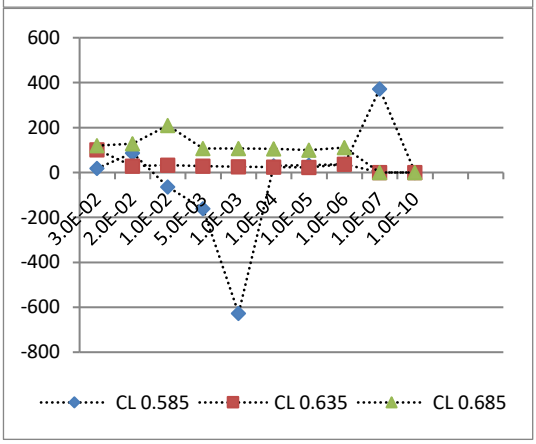


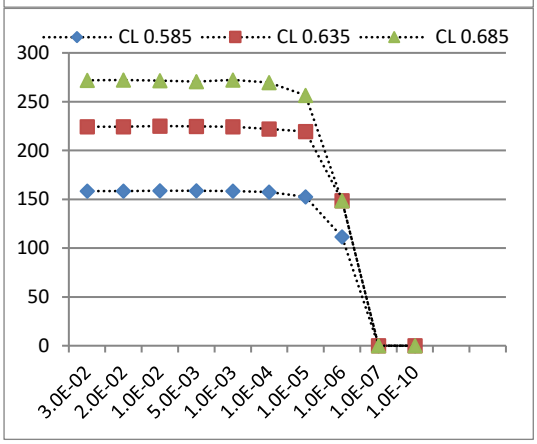

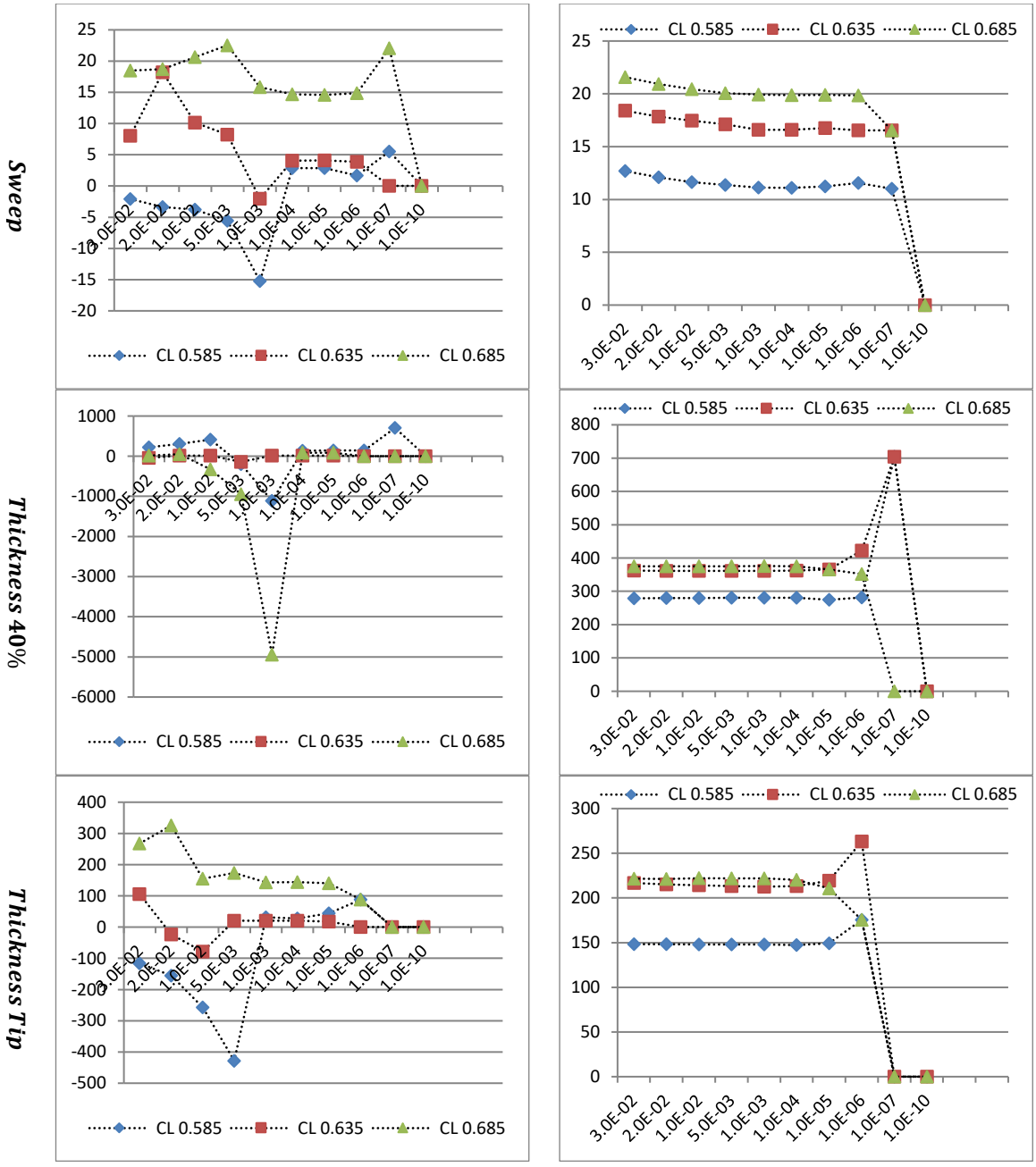


**Figure 4.12: Step length investigation for reliable finite difference sensitivity analysis**

A procedure to allow global geometrical perturbation of the wing, then of the top level variables, was developed starting from the SeAnDef mesh deformation tool. SeAnDef is used to perform aerodynamic and aero-elastic optimization and handles variables such as chord, thickness and position of certain wing control sections, but it is not able to handle global variable such us the 6 top level geometrical variables chosen for the MDO-OAD procedure. Then, the developed program obtains the top level variable values and the aircraft mesh as input and give the new deformed mesh as output. The core of the program is the deformation tool SeAnDef for which each single

local deformation capabilities were used to perform a global deformation of the wing geometry. The program was stressed by imposing huge deformation to the wing and it results in handling deformation way over physical expected deformation.

In the next section, it will be put in evidence how the aforementioned enrichment may lead to a different optimum than the one without considering higher fidelity evaluations.

### 4.2.3 MDO-OAD optimization results

The MDO-OAD approach was applied on the BSW and FSW benchmarks that reflect the current Airbus preliminary design capabilities, based on theoretical and semi-empirical models. Referring to Figure 4.6, sequential structural and aero-elastic optimizations increase the aircraft efficiency and give the components for the OAD enrichment. The top level OAD optimization performs DOC reduction optimizing 6 top level variables that define the wing. The new wing geometry is used for the new sequential structural and aero-elastic optimizations that will enrich the further OAD optimization, leading the DOC reduction. Table 4.7 and 4.8 show the results of the new preliminary design approach on BSW and FSW benchmark introduced in Sec. 4.2.1.

| **BSW** | | **Benchmark** | **OAD opt Not enriched** | **OAD opt Loop 1** | **OAD opt Loop 2** |
|---|---|---|---|---|---|
| $C_L$ | [-] | 0.635 | 0.631 | 0.558 | 0.544 |
| $\varphi_{25\%}$ | [°] | 18.15 | 18.06 | 19.26 | 19.09 |
| $S$ | [$m^2$] | 97.503 | 97.715 | 108.109 | 109.694 |
| $AR$ | [-] | 9.93 | 11 | 10.99 | 11 |
| $TR$ | [-] | 0.2697 | 0.2576 | 0.2392 | 0.2303 |
| $t/c\|_{40\%}$ | [-] | 0.14136 | 0.1499 | 0.1330 | 0.1257 |
| $t/c\|_{tip}$ | [-] | 0.1141 | 0.1195 | 0.1106 | 0.1136 |
| $DOC$ | [$/trip] | 16452 | 16418 | 15869 | 16047 |
| $MTOW$ | [kg] | 122231 | 121888 | 118996 | 120970 |

**Table 4.7: Results of the MDO-OAD procedure applied on the BSW configuration**

| FSW | | Benchmark | OAD opt Not enriched | OAD opt Loop 1 | OAD opt Loop 2 |
|---|---|---|---|---|---|
| $C_L$ | [-] | 0.635 | 0.633 | 0.592 | 0.598 |
| $\varphi_{25\%}$ | [°] | -18.15 | -17.80 | -19.00 | -19.53 |
| $S$ | [$m^2$] | 97.503 | 97.56 | 104.23 | 104.84 |
| $AR$ | [-] | 9.93 | 11 | 9.28 | 9.21 |
| $TR$ | [-] | 0.2697 | 0.2353 | 0.2843 | 0.2783 |
| $t/c\|_{40\%}$ | [-] | 0.14136 | 0.1450 | 0.1424 | 0.1439 |
| $t/c\|_{tip}$ | [-] | 0.1141 | 0.1048 | 0.1073 | 0.1058 |
| $DOC$ | [$/ trip] | 16452 | 16410 | 16155 | 16553 |
| $MTOW$ | [kg] | 122231 | 121881 | 121770 | 123737 |

**Table 4.8: Results of the MDO-OAD procedure applied on the FSW configuration**

The *benchmark* column refers to the aircraft baseline, while the *OAD opt not enriched* shows the results of the Airbus current OAD optimization process with respect to the 7 top-level variables, without physical enrichment by the aero-structural procedure. The two columns of *OAD opt Loop 1* and *OAD opt Loop 2* represent the OAD optimization considering the sensitivity coming from respectively the first and the second aero-structural optimization iteration. By comparing the results of the OAD optimization without sensitivity indication and one with sensitivity enrichment, it is possible to notice how the physics leads the optimizer toward a different solution. This implies that this particular approach based on model enrichment is effective for conventional and unconventional aircraft. Particularly interesting is the aspect ratio trend for the FSW configuration. It is clear that, without physics enrichment, the optimizer tends to increase it to its limits, while by adding the enrichment the aspect ratio is limited. For FSW seems that the increasing of the aspect ratio does not give benefit as for the BSW does. Table 4.9 and Table 4.10 may help in understanding the results of Table 4.7 and 4.8. In there, the sensitivity analysis used for the OAD enrichment during loop 1 and 2 of the MDO-OAD procedure are listed. Focusing on the aspect ratio sensitivity of the loop 1 for instance, it is possible to see how predominant the negative sensitivities

are respect to the positive ones, explaining why the optimization resulted in an increment of the aspect ratio for the BSW geometry. Conversely, for the FSW geometry it is possible to see that positive sensitivities over the wave and induced drag for the 3 lift conditions are more important that the negative ones. Thus, an increment of the aspect ratio will result in an increment of the drag. Then the aspect ratio for the FSW architecture was decreased by the optimizer. Same discussion can be done for the other top level variables. The sensitivities of Table 4.8 and 4.9 resulted to be uniform over the different lift conditions, with the exception of few of them underlined in red. They were judged as *not in line* with their own trend over the lift conditions, but it is hard to state that they are incorrect. Since only few sensitivities may show inconsistency, the OAD enrichment was judged as reliable.

| BSW | Aero-elastic Sensitivity | | | | | | Structural Sensitivity |
|---|---|---|---|---|---|---|---|
| | $C_{L\_1}$ | | $C_{L\_2} = C_{L\_cruise}$ | | $C_{L\_3}$ | | $C_{L\_cruise}$ |
| | $C_{Di}$[10-4] | $C_{Dw}$[10-4] | $C_{Di}$[10-4] | $C_{Dw}$[10-4] | $C_{Di}$[10-4] | $C_{Dw}$[10-4] | $W$ [kg] |
| | **Loop 1** | | | | | | |
| $\partial/\partial S$ | -0.473 | -0.152 | -0.581 | -0.524 | -0.715 | -1.137 | 12.625 |
| $\partial/\partial AR$ | -9.429 | 0.347 | -11.451 | 0.999 | -12.971 | 0.845 | 170.260 |
| $\partial/\partial TR$ | -14.718 | 11.962 | -0.840 | 36.537 | -0.626 | 43.723 | 4083.986 |
| $\partial/\partial \varphi_{25\%}$ | -0.975 | -1.946 | -1.162 | -3.657 | -1.565 | -5.479 | -2.925 |
| $\partial/\partial {t/c}\|_{40\%}$ | 7.243 | 11.843 | 16.832 | 19.457 | 15.254 | 24.723 | -203.745 |
| $\partial/\partial {t/c}\|_{tip}$ | -29.305 | -44.786 | -54.433 | -57.521 | -49.291 | -73.420 | 9111.206 |
| | **Loop 2** | | | | | | |
| $\partial/\partial S$ | -0.196 | 0.015 | -0.267 | -0.053 | -0.312 | -0.243 | 11.257 |
| $\partial/\partial AR$ | -4.988 | 0.171 | -6.005 | 0.591 | -7.013 | 2.455 | 73.019 |
| $\partial/\partial TR$ | -12.079 | -0.081 | 5.748 | 11.843 | -11.478 | 26.797 | 2611.869 |
| $\partial/\partial \varphi_{25\%}$ | -1.963 | -0.568 | -2.554 | -1.349 | -3.624 | -4.309 | 23.006 |
| $\partial/\partial {t/c}\|_{40\%}$ | 18.179 | -9.220 | 18.289 | 5.656 | 18.845 | 5.707 | -528.202 |
| $\partial/\partial {t/c}\|_{tip}$ | -78.323 | 38.334 | -82.213 | -23.033 | -88.701 | -19.553 | 7177.308 |

**Table 4.9: Sensitivity analysis for OAD enrichment of the BSW architecture used for the first and second loop of the MDO-OAD procedure**

| FSW | Aero-elastic Sensitivity | | | | | | Structural Sensitivity |
|---|---|---|---|---|---|---|---|
| | $C_{L\_1}$ | | $C_{L\_2} = C_{L\_cruise}$ | | $C_{L\_3}$ | | $C_{L\_cruise}$ |
| | $C_{Di}$[10-4] | $C_{Dw}$[10-4] | $C_{Di}$[10-4] | $C_{Dw}$[10-4] | $C_{Di}$[10-4] | $C_{Dw}$[10-4] | $W$ [kg] |
| | **Loop 1** | | | | | | |
| $\partial/\partial S$ | -0.566 | -0.194 | 0.043 | 0.409 | 0.175 | 0.757 | 9.696 |
| $\partial/\partial AR$ | -9.202 | -2.534 | -0.937 | 8.257 | -1.397 | 20.153 | 146.896 |
| $\partial/\partial TR$ | -71.596 | -20.284 | 8.359 | 12.232 | 47.364 | -5.185 | 429.107 |
| $\partial/\partial \varphi_{25\%}$ | -1.319 | -0.113 | 2.568 | 3.911 | 4.249 | 8.458 | -2.134 |
| $\partial/\partial {}^{t}/_{c}\big\vert_{40\%}$ | 21.477 | 20.828 | 21.994 | -33.264 | 15.198 | -81.329 | -550.034 |
| $\partial/\partial {}^{t}/_{c}\big\vert_{tip}$ | 5.177 | -16.396 | -26.017 | 31.541 | -29.703 | 86.798 | 2903.587 |
| | **Loop 2** | | | | | | |
| $\partial/\partial S$ | -0.221 | -0.171 | -0.284 | 0.343 | -0.632 | 0.723 | 7.232 |
| $\partial/\partial AR$ | -4.696 | 4.714 | -8.088 | 9.616 | -16.237 | 18.539 | 55.088 |
| $\partial/\partial TR$ | 34.826 | 4.614 | -52.877 | -18.180 | 92.679 | 44.166 | 3343.406 |
| $\partial/\partial \varphi_{25\%}$ | -0.015 | 1.956 | 0.466 | 3.753 | -0.059 | 7.052 | -2.681 |
| $\partial/\partial {}^{t}/_{c}\big\vert_{40\%}$ | 55.515 | -14.496 | 56.517 | -26.359 | 30.572 | -51.456 | -504.449 |
| $\partial/\partial {}^{t}/_{c}\big\vert_{tip}$ | -68.959 | 15.139 | -43.209 | 35.717 | -50.325 | 47.689 | 8349.764 |

**Table 4.10: Sensitivity analysis for OAD enrichment of the FSW architecture used for the first and second loop of the MDO-OAD procedure**

The results of the MDO-OAD procedure (Table 4.7 and 4.8) show how the top level variables and the DOC converge to a similar solution after only two iterations (loops). This approach seems to be very efficient. It is important to notice that the resulted optimized geometry does not necessarily have smaller DOC with respect to the benchmark or the configuration obtained by performing the unenriched OAD optimization, but a more reliable one. This is important to understand that the results of the new developed preliminary design optimization method have to be seen as more reliable that the ones achieved by the nowadays OAD method. The procedure

found the best compromise of top level variables to achieve DOC minimization by considering more reliable aerodynamic and structural data.

In Figure 4.13, the different BSW geometries over the procedure are shown. The geometry **I** is the benchmark, while the **II** and **III** are the optimized shape after the first and the second MDO-OAD loop respectively.

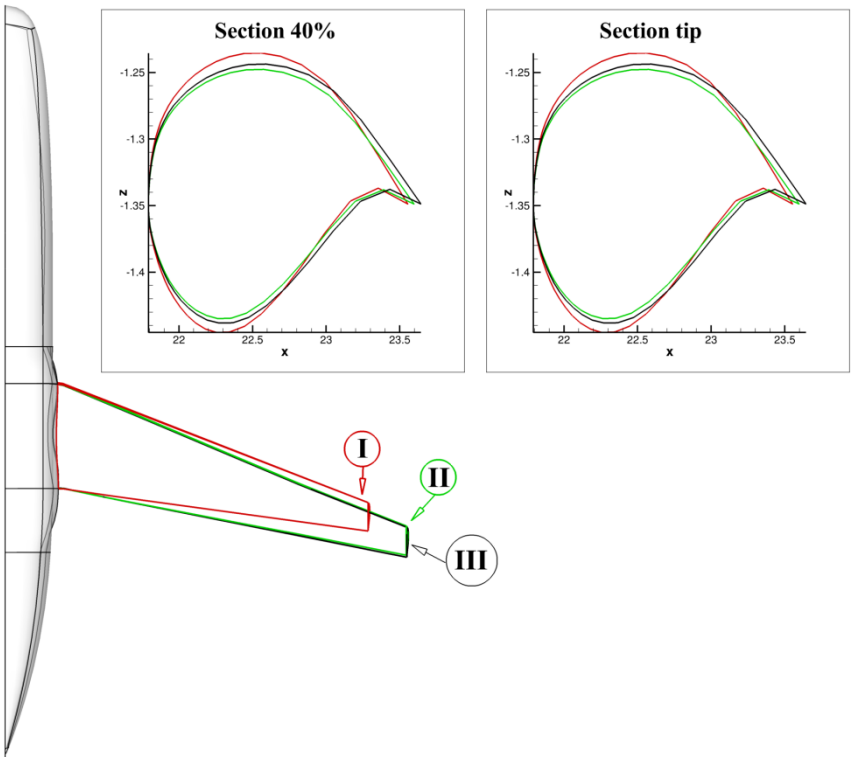


**Figure 4.13: Geometric evolution throughout the MDO-OAD innovative procedure**

# Chapter 5

# Conclusion et Future Development

## 5.1 Conclusion

The thesis demonstrates how a high fidelity aero-structural approach can be used in the preliminary aircraft design stage for novel configurations. This mitigates risk associated with unusual configurations and allows the designer to move away from conventional configurations, something which current regression models struggle to address. Nowadays, conceptual and preliminary design are based on theoretical and semi-empirical models built from historical data which allow very fast evaluation with acceptable reliability if conventional architectures are considered. Those methods are very robust within the domain where the data bases are collected, but for unconventional behaviour. Aerodynamic and structure estimations of the current overall aircraft design approach suffer this lack of experience. This study is focussed on a procedure for fast and reliable aero-structural design and optimization used to enrich the preliminary design semi-empirical models to be used to design unconventional aircraft.

This work begins with an introduction with the mathematical models used for the investigation with particular emphasis on the far-field drag extraction methods that enable reliable analysis and optimization while having very coarse mesh. The geometrical and mesh features of the test case configuration are also analysed. A good trade-off between low numerical errors (mesh quality for Euler model) and good convergence was found by having:

- Sharp trailing edge and rounded wing tip;

- Mesh cells perpendicular to the wing surface;
- Very smooth change in direction from adjacent cells.

The aerodynamic and aero-elastic investigation underlined the needs of considering the wing-body configuration for having a reliable representation of the airflow around the wing, especially at the wing inboard where wing-fuselage interactions are observed.

Wing shape optimization proved the importance of considering the wing deformation while optimizing the shape of the wing. The investigation described the inconsistency of the polar obtained upon the undeformed wing and presented the benefits of considering the deformed wing shape under the aerodynamics load. The points of the elastic polar represent the wing shape in equilibrium with its load. That condition is significant also during the structural optimization in order to obtain the right structural size for the right aerodynamic loads.

Concerning the parameterization methods to be used to undertake a shape optimization, important results were obtained by comparing experience-based parameters and vertex-morphing method. The study showed the importance of choosing the right design variables depending on which part of the aircraft is going to be optimise. In particular, the investigation presents the benefit of using experience-based design variables whenever the shape to optimize is easily described by geometrical parameters such as camber and twist for the wing. Conversely, if geometrical variables are not of easy identification, the vertex-morphing method may lead to valuable results. By combining those two parameterization techniques the best optimization of the whole aircraft was found: experience-based design variables were used for the wing, while the wing-fuselage intersection was handled by the vertex-morphing method that consider each mesh nodes as shape variables.

The last part of the work is dedicated to the new suggested MDO approach. This new approach enabled the preliminary design of unconventional aircraft otherwise very difficult since no data bases are available, and it is based on two optimization levels to be addressed iteratively:

- Top level OAD optimization for economic efficiency (cost reduction);

- Aero-elastic and structural optimizations for OAD models enrichment with physical information.

The innovation of the approach stated on two important things:

- the choice of the top level variables: they are those for which there is a strong coupling between aerodynamics and structure. Such variables were not considered during the single discipline optimization to reduce the error of not considering cross-sensitivity
- the use of the sensitivity analysis of the aerodynamic and structure objective functions with respect to the top level variables to correct the OAD preliminary design and optimization model.

This new methodology showed very fast convergence to the optimum (about 2-3 iterations maximum) and obtained higher-fidelity results since not only use semi-empirical models but fast aerodynamic and structural evaluations.

## 5.2 Future development

This research turns on the light on the enormous benefits the aircraft design may have if higher-fidelity information are used within the Overall Aircraft Design framework, especially if unconventional aircrafts are considered.

A very useful test could be to investigate the sensitivity of the result of the proposed optimization procedure with respect to the fidelity of the aerodynamic and structural models. In that way it could be possible to understand if an increasing of the evaluation time is worth it or not.

Another axis of improvement is the development of simplified models to consider aerodynamic and structural behaviour which usually demand a lot of computational time. For instance, several researchers are studying simple ways to analyse flow detachment and the structural vibration that follows which are very impactful on the overall result of the aircraft design. Following the same idea, to include preliminary composite behaviour could be very interesting for light and fatigue resistant structure.

# Bibliography


Abbott I.H., Von Doenhoff A.E. “Theory of Wing Sections”. Dover Edition, 1959.

Akgün M. A., Haftka R. T., Wu K. C., Walsh J. L. “Sensitivity of Lumped Constraint Using the Adjoint Method”. AIAA paper 99-1314, 1999.

Alonso J. J., Kroo I. M. “Advanced Algorithm for Design and Optimization of Quiet Supersonic Platform”. 40th AIAA Aerospace Science Meeting and Exibit, 2002.

Anderson J.D. “Computational Fluid Dynamics”. Mc Graw Hill Edition, 1995.

Anderson J.D. “Fundamental of Aerodynamics”. Mc Graw Hill Edition, 2011.

Anderson W. K., Bonhaus D. L. “Airfoils Design on Unstructured Grids for Turbulent Flows”. AIAA Journal, Vol. 37, No. 2, pp. 185-191, 1999.

Anderson W. K., Newman J. C., Withfield D. L., Nielsen E. J. “Sensitivity analysis for Navier-Stokes equations on unstructured meshes using complex variable”. AIAA journal, Vol. 39, No. 1, pp. 56-63, 2001.

Anderson W. K., Venkatakrishnan V. “Aerodynamic design optimization on unstructured grids with a continuous adjoint formulation”. AIAA paper 97-0643, 1997.

Antoine N. E. “Aircraft optimization for minimal environmental impact”. Ph.D. thesis at Stanford University, 2004.

Aronstein D., Schueler K. “Two supersonic business aircraft conceptual designs, with and without sonic boom constraint”. Journal of Aircraft, Vol. 42, No. 3, pp. 775-786, 2005.

Bach C., Jebari R., Viti A., Hewson R. “Composite stacking sequence optimization for aeroelastically tailored forward-swept wings”. Structural and Multidisciplinary Optimization, 2016.

Badufle C. “Conceptual aircraft design: towards multiobjective, robust and uncertain optimization”. PhD thesis, University of Toulouse III – Paul Sabatier, 2007.

Bauchau O.A, Craig J.I. “Structural Analysis, with Application to Aerospace Structures”. Springer Edition, 2009.

Baumgärtner D., Viti A., Dumont A., Carrier G., Bletzinger K.-U. “Comparison and combination of experience-based parameterization with vertex morphing in aerodynamic shape optimization of a forward-swept wing aircraft”. AIAA/ISSMO-MOA Conference, 2016.

Baysal O., Eleshaky M. E. “Aerodynamic sensitivity analysis methods for the compressible Euler equations”. Journal of Fluid Engineering, Vol. 113, pp. 681-688, 1991.

Baysal O., Eleshaky M. E. “Aerodynamic Design Optimization Using Sensitivity Analysis and Computational Fluid Dynamics”. AIAA Journal, Vol. 30, No. 3, pp. 718-725, 1992.

Bérard A., Rizzi A., Isikveren A.T. “CADac: A New Geometry Construction Tool for Aerospace Vehicle Pre-Design and Conceptual Design”. 26th AIAA Applied Aerodynamics Conference, 2008.

Birman J. “Uncertainty quantification and propagation in Conceptual Aircraft Design: from deterministic optimization to chance constrained optimization”. PhD thesis, University of Toulouse III – Paul Sabatier, 2013.

Bischof C., Carle A., Corliss G., Grienwank A., Hoveland P. “ADIFOR: Generating derivatives codes from fortran programs”. Scientific Programming, Vol. 1, No. 1, pp. 11-29, 1992.

Bisplinghoff R.L., Ashley H., Halfman R.L. “Aeroelasticity”. Dover Science Books, 1996.

Bisson F., Nadarajah S. “Adjoint-Based Shape Optimization for Induced Drag”. 32nd AIAA Applied Aerodynamics Conference, 2014.

Bletzinger K.-U. “A consistent frame for sensitivity filtering and the vertex assigned morphing of optimal shape”. Structural and Multidisciplinary Optimization, Vol. 49, No. 6, pp. 873-895, 2014.

Brezillon J., Dwight R. P. “Applications of a Discrete Viscous Adjoint Method for Aerodynamic Shape Optimization for 3D Configurations”. CEAS Aeronautical Journal, Vol. 3, No. 1., pp. 25-34, 2012.

Brunet V., Deck S., Molton P., Thiery M. “A complete Experimental an Numerical Study of the Buffet Phenomenon over the OAT15A Airfoil”. 40éme Colloque Aérodynamique Appliquée, 2005.

Buresti G. “Elements of Fluid Dynamics”. Fluid Mechanics, Vol.3, Imperial College Press, 2012.

Burgreen G. W., Baysal O. “Three-dimentional aerodynamic shape optimization using discrete sensitivity analysis”. AIAA Journal, Vol. 34, No. 9, pp. 1761-1770, 1996.

Cabuk H., Shung C. H., Modi V. “Adjoint operator approach to shape design for internal incompressible flow”. 3rd International Conference on Inverse Design and Optimization in Engineering Science, pp. 391-404, 1991.

Cambier L., Veuillot JP. “Status of the elsa cfd software for flow simulation and multidisciplinary applications”. *AIAA paper*, 664:2008, 2008.

Cambier L., Gazaix M. “*elsA*: an efficient object-oriented solution to CFD complexity”. 40th AIAA Aerospace Science Meeting and Exhibit, 2002

Carrera E., Giunta G., Petrolo M. “Beam Structures”. John Wiley & Son Edition, 2011.

Carrier G., Destarac D., Dumont A., Méheut M., Salah El DIn I., Peter J., Ben Khelil S., Brezillon J., Pestana M. “Gradient-Based Aerodynamic Optimization with *elsA* Software”. 52nd Aerospace Science Meeting, AIAA SciTech, 2014.

Chen X., Kostreva M. M. “Methods of Feasible Direction: A Review”. Progress in Optimization, Applied Optimization book series, Vol. 39, pp. 205-219, 2000.

Chittick I. R., Martins J. R. R. A. “Aero-structural optimization using adjoint coupled post-optimality sensitivity”. Structural and Multidisciplinary Optimization, Vol. 36, No. 1, pp. 59-70, 2008.

Christodoulou D., Miao S. “Compressible Flow and Euler’s Equations”. Survey of Modern Mathematics, Vol. 9, International Press of Boston, 2014.

Cliff S., Reuther J., Saunders D., Hicks R. “Single-Point and Multipoint Aerodynamic Shape Optimization of High-Speed Civil Transport”. Journal of Aircraft, Vol. 38, No.6, pp. 997-1005, 2001.

Dakota: Design Analysis Kit for Optimization and Terascale Applications. Developed by Sadia National Laboratories, Albuquerque, New Mexico. http://endo.sadia.gov/DAKOTA/software.html

DeBlois A., Abdo M. “Multi-fidelity Multidisciplinary Design Optimization of Metallic and Composite Regional and Business Jets”. AIAA/ISSMO Multidisciplinary Analysis Optimization Conference, 2010.

Debrabandere F., Tartinville B., Hirsch C. “A staggered method using a modal approach for fluid-structure interaction computation”. IFASD, 2011.

Destarac D. “Drag Extraction from Numerical Simulations to the Equations of Fluid Dynamics: the Far-field Philosophy”. 43ème Colloque d’Aérodynamique Appliquée de l’Association Aéronautique Astronautique de France, 2008.

Destarac D. “Investigation Negative Drag in Grid Convergence for Two-Dimensional Euler Solution”. Journal of Aircraft, Vol. 48, No.4, pp. 1468-1470, 2011.

Destarac D. “Far-field Drag in Transonic Potential Flow : Analysis and Optimisation”. Proceedings of the 1993 European Forum, Recent Developments and Applications in Aeronautical CFD, The Royal Aeronautical Society, 1993.

Destarac D. “Far_field / Near-field Drag Balance and Applications of Drag Extraction in CFD”. Lecture Series: CFD-based aircraft drag prediction and reduction, Von Karman Institute for Fluid Dynamics, 2003.

Destarac D., Van der Vooren J. “Drag / Thrust Analysis of Jet-propeller Transonic Transport Aircraft: Definition of Physical Drag Component”. Aerospace Science & Technology, Vol. 8, No. 6, pp. 545-556, 2004.

Dumont A., Ghazlane I., Marcelet M., Carrier C., and Salah El Din I. “Overview of recent development of aeroelastic adjoint method for civil aircraft wing optimization”. In *ONERA DLR Aerospace Symposium*, 2011.

Dumont A., Le Pape A., Peter J., Huberson S. “Aerodynamic Shape Optimisation of Hovering Rotors Using a Discrete Adjoint of the Reynolds-Averaged Navier-Stokes Equations”. Journal of the American Helicopter Society, Vol. 56, 2011.

Dwight R. P., Brezillon J. “Efficient and Robust Algorithms for Solution of the Adjoint Compressible Navier-Stokes Equations with Applications”. International Journal for Numerical Methods in Fluids, Vol. 60, pp. 365-389, 2009.

Elliot J. K. “Aerodynamic optimization based on the Euler and Navier-Stokes equations using unstructured grid”. Ph.D. thesis, Massachussets Institute of Technology, 1998.

Epstein B., Peigin S. “Robust Hybrid Approach to Multiobjective Constrained Optimization in Aerodynamics”. AIAA journal, Vol. 42, No. 8, pp. 1572-1581, 2004.

Esquieu S. “Reliable Drag Extraction from Numerical Solution: Elimination of Spurious Drag”. Computational Uncertainty in Military Vehicles Design, RTO-MP-AVT-147, Paper 42, pp. 1-16, 2007.

Falco S. A., Rocha de Faria A. “Optimization of a simple aircraft wing”. Worldwide Aerospace Conference and Technology Showcase, 2002.

Farhat C., Lesoinne M., LeTallec P. “A conservative algorithm for exchanging aerodynamic and elastodynamic data in aeroelastic system”. 36th AIAA Aerospace Sciences Meeting and Exhibit, 1997.

Farhat C., Lesoinne M., LeTallec P. “Load and motion transfer algorithm for fluid/structure interaction problems with non-matching discrete interfaces: Momentum and Energy conservation, optimal discretization and application to aeroelasticity”. Computer Methods in Applied Mechanics and Engineering, 1998.

Flager F., Haymaker J. “A Comparison on Multidisciplinary Design Analysis and Optimization Process in the Building Construction and Aerospace Industries”. Department of Civil and Environmental Engineering, 2007.

Foster N. F., Dulikravich G. S. “Theree-Dimensional Aerodynamic Shape Optimization using Genetic and Gradient Search Algorithms”. Journal of Spacecraft and Rockets, Vol. 34, No. 1, pp. 36-42, 1997.

Frank P. D., Shubin G. R. “A Comparison of Optimization-Based Approaches for Model Computational Aerodynamics Design Problem”. Journal of Computational Physics, Vol. 98, No. 1, pp.74-89, 1992.

Frota J. “Novel Concept of Aircraft Component Technologies: the NACRE European Integrated Project”. 5th ICAS Congress, 2006.

Garcelon J. H., Balabanov V. “Integrating VisualDOC and GENESIS for Multidisciplinary Optimization of a Transport Aircraft Wing”. 3rd World Congress of Structural and Multidisciplinary Optimization, 1999.

Garcelon J. H., Balabanov V., Sobieski J. “Multidisciplinary Optimization of a Transport Aircraft Wing using VisualDOC”. Optimization in Industry-II, 1999.

Gariépy M., Trépanier J-Y., Masson C. “Improvements in Accuracy and Efficiency for a Far-Field Drag Prediction and Decomposition Method”. 28th AIAA Applied Aerodynamics Conference, 2010.

Gauger N. R. “Efficient Deterministic Approaches for Aerodynamic Shape Optimization”. Optimization and Computation Fluid Dynamics, Springer-Verlag, pp. 111-145, 2008.

Ghazlane I. “Adjoint-based Aerostructural Sensitivity Analysis for Wing Design”. PhD thesis at ONERA, The French Aerospace Lab, 2012.

Giesing J. P., Barthelemy J.-F. “A summary of industry MDO applications and needs”. 7th AIAA/USAF/NASA/ISSMO Symposium on Multidisciplinary Analysis and Optimization, AIAA Paper No. 98-4737, 1998.

Giles M. B., Pierce N. A. “Adjoint equations in CFD: duality, boundary conditions and solution behavior”. 13th Computational Fluid Dynamic Conference, 1997.

Giles M. B., Pierce N. A. “An Introduction to the Adjoint Approach to Design”. Flow, Turbulence and Combustion, Vol. 65, Issue 3-4, pp.393-415, 2000.

Giunta A., Golividov O., Knill D., Grossman B., Mason W., Watson L., Haftka R. “Multidisciplinary design optimization of advanced aircraft configurations”. 15th International Conference on Numerical Methods in Fluid Dynamics, pp. 14-34, 1997.

Goldberg D. “Genetic Algorithms in Search, Optimization and Machine Learning”. Addison-Wesley, 1989.

Green L. L., Newman P. A., Haigler K. J. “Sensitivity Derivatives for Advanced CFD Algorithm and Viscous Modeling Parameters via Automatic Differentiation”. 11th AIAA Computational Fluid Dynamics Conference, 1993.

Griewank A. “On Automatic Differentiation”. Mathematical Programming: Recent Development and Applications, Kluwer Academic Publisher, pp. 83-108, 1989.

Grihon S., Mahé M. “Structural and multidisciplinary optimization Applied to Aircraft Design”. 3rd Worls Congress of Structural and Multidisciplinary Optimization, 1999.

Hepperle M. “MDO of Forward Swept Wings”. KATnet II Workshop, 2008.

Hicken J. E., Zingg D. W. “Induced-Drag Minimization of Nonplanar Geometries Based on Euler Equations”. AIAA Journal, Vol. 48, No. 11, pp. 2564-2575, 2010.

Hicks R. M., Henne P. A. “Wing Design by Numerical Optimization”. Journal of Aircraft, Vol. 15, pp. 407-412, 1978.

Hicks R. M., Murman E. M., Vanderplaats G. N. “An Assessment of Airfoil Design by Numerical Optimization”. Tech. Rep. NASA-TM-X-3092, 1974.

Hirsch C. “Numerical computation of external and internal flows – the fundamentals of computation fluid dynamics”. Second edition, *Elsevier* editor, 2007.

Hojjat M., Stavropoulou E., Bletzinger K.-U. “the Vertex Morphing method for node-based shape optimization”. Computer Methods in Applied Mechanics and Engineering, Vol. 268, pp. 494-513, 2014.

Holland J. H. “Adaption in Natural and Artificial Systems”. University of Michigan Press, 1975.

Hue D. “Fifth Drag Prediction Workshop: Computational Fluid Dynamics Studies Carried Out at ONERA”. Journal of Aircraft, Vol. 51, No. 4, 2014.

Hue D., Esquieu S. “Computational Drag Prediction of the DPW4 Configuration Using the Far-Field Approach”. Journal of Aircraft, Vol. 48, No. 5, 2011.

Jaquin L., Molton P., Deck S., Soulevant D. “Experimental Study of Shock Oscillation over a Transonic Supercritical Profile”. AIAA Journal; Vol. 47, No. 9, 2005.

Jameson A. “Aerodynamic design via control theory”. Journal of Scientific Computing, Vol.3, pp. 233-260, 1988.

Jameson A. “Optimum aerodynamic design using CFD and control theory”. AIAA paper, 95-1729-CP, 1995.

Jameson A., Martinelli L., Pierce N. “Optimum Aerodynamic Design using the Navier-Stokes Equations”. Theoretical and Computational Fluid Dynamics, Vol. 10. No. 1-4, pp. 213-237, 1998.

Jameson A., Schmidt W., Turkel E. “Numerical Solution of the Euler Equations by Finite Volume Methods Using Runge-Kutta Time-Stepping Scheme”. 14th AIAA Fluid and Plasma Dynamics Conference, AIAA Paper 81-1259, 1981.

Karalliu X. “Numerical Dissipation in the Solution of Euler Equations, its Impact on Aeroelasticity”. PhD thesis at Politecnico di Milano, 2018.

Kennedy J., Eberhart R. “Particle Swarm Optimization”. IEEE International Conference on Neural Networks, 1995.

Kenway G. K. W., Martins J. R. R. A. “Multi-points High-fidelity Aerostructural Optimization of a Transport Aircraft Configuration”. Journal of Aircraft, Vol. 51, No. 1, pp. 144-160, 2014.

Kodiyalam S., Sobieszczanski-Sobieski J. “Multidisciplinary design optimization-some formal methods, framework requirement, and application to vehicle design”. International Journal of Vehicles Design, Vol. 25, No. 1, pp. 3-22, 2001.

Kroo I. “MDO for Large-Scale Design”. Multidisciplinary Design Optimizatio, State of art – ICASE/NASA Longley Workshop on Multidisciplinary Design Optimization, pp. 22-44, 1995.

Larosterna Engineering Dynamics Lab, Aircraft Modeling & Mesh Generation, http://www.larosterna.com/sumo.html

Li J., Tang H., Warnecke G., Zhang L. “Local Oscillation in Finite Difference Solutions of Hyperbolic Conservative Laws”. Mathematics of Computation, Vol. 78, No. 268, pp. 1997-2018, 2009.

Liepmann H. W., Roshko A. “Elements of Gasdynamics”. John Wiley & Sons, Inc., 1957.

Lock R.C. “Prediction of the Drag of Wings at Subsonic Speed by viscous / inviscid interaction techniques”. AGARD-R-723, Aircraft Drag Prediction and Reduction, 1985.

Lyu Z., Xu Z., Martins J. R. R. A. “Benchmarking Optimization Algorithms for Wing Aerodynamic Design Optimization”. The Eight International Conference on Computational Fluid Dynamics (ICCFD8), 2014.

Marcelet M. “Etude et mise en oeuvre d’une methode d’optimisation de forme couplant simulation numerique en aerodynamique et en calcul de structure”. PhD thesis at ONERA, The French Aerospace Lab, 2008.

Martins J. R. R. A. “A Coupled-Adjoint Method for High-Fidelity Aero-Structural Optimization”. PhD thesis at Stanford University, 2002.

Martins J. R. R. A. “A Coupled-Adjoint Sensitivity Analysis Method for High-Fidelity Aero-Structural Design”. Optimization and Engineering, Vol. 6, pp. 33 – 62, 2005.

Martins J. R. R. A. “Multidisciplinary Design Optimization”. 7th International Fab Lab Forum and Symposium on Digital Fabrication, 2011.

Martins J. R. R. A., Alonso J. J. “Aero-Structural Wing Design Optimization Using High-Fidelity Sensitivity Analysis”. CEAS Conference on Multidisciplinary Aircraft Design Optimization, 2001.

Martins J. R. R. A., Alonso J. J. “High-Fidelity Aero-Structural Design Optimization of a Supersonic Business Jet”. 43th AIAA/ASME/ASCE/AHS/ASC Structure, Structural Dynamics and Materials Conference, 2002.

Martins J. R. R. A., Hwang J. T. “Review and Unification of Methods for Computing Derivatives of Multidisciplinary Computational Models”. AIAA Journal, Vol. 51, No. 11, pp. 2582-2599, 2013.

Martins J. R. R. A., Kroo I. M., Alonso J. J. “An automated method for sensitivity analysis using complex variables”. AIAA paper 2000-0689, 2000.

Martins J. R. R. A., Reuther J. J. “Complete Configuration Aero-Structural Optimization Using a Coupled Sensitivity Analysis Method”. 9th AIAA/ISSMO Symposium on Multidisciplinary Analysis and Optimization, 2002.

Martins J. R. R. A., Sturdza P., Alonso J. J. “The connection between complex-step derivative approximation and algorithmic differentiation”. AIAA paper 2001-0921, 2001.

Martins J. R. R. A., Sturdza P., Alonso J. J. “The Complex-Step Derivative Approximation”. ACM Transaction on Mathematical Software, Vol. 29, No. 3, pp. 245-262, 2003.

Marvis D. N., DeLaurentis D. “Methodology for examining the simultaneous impact of requirements vehicle characteristics, and technologies on military aircraft design”. ICAS Congress, 2000.

Masson C., Veilleux C., Paraschivoiu I. “Airfoil Wave-Drag Prediction Using Euler Solutions of Transonic Flows”. Journal of Aircraft, Vol. 35, No. 5, 1998.

Méheut M., Bailly D. “Drag-Breakdown Methods from Wake Measurements”. AIAA Journal, Vol. 46, No. 4, 2008.

Mengistu T., Ghaly W. “Global Optimization Methods for the Aerodynamic Shape Design of Transonic Cascades”. 11th CFD Conference of the Canadian Society of CFD, Vol.1, pp. 238-243, 2003.

MDO Technical Committee. “Some popular definition for Multidisciplinary Design Optimization”. See also http://www.aiaa.org/portal/index.cfm?Getcomm=80. Copyright 2007 AIAA.

Nemec M., Zingg D. W., Pulliam T. H. “Multipoint and Multi-Objective Aerodynamic Shape Optimization”. AIAA Journal, Vol. 42, No. 6, 2004.

Neufeld D. “Multidisciplinary Aircraft Conceptual Design Optimization Considering Fidelity Uncertainties”. Ph.D. thesis at Ryerson University, 2010.

Nielsen E. J., Anderson W. K. “Aerodynamic Design Optimization on Unstructured Meshes Using the Navier-Stokes Equations”. AIAA Journal, Vol. 37, No. 11, pp. 1411-1419, 1999.

Nocedal J., Wright S. J. “Numerical Optimization”. Springer, 2006.

Obayashi S., Sasaki D. “Self-organizing map of pareto solutions obtained from multiobjective supersonic wing design”. AIAA paper 2002-0991, 2002.

Obayashi S., Tsukahara T. “Comparison of Optimization Algorithms for Aerodynamic Shape Design”. AIAA journal, Vol. 35, No. 8, 1997.

Osusky L. M. “A Numerical Methodology for Aerodynamic Shape Optimization in Turbulent Flow Enabling Large Geometric Variation”. Ph.D thesis, University of Toronto, 2014.

Othmer C. “Adjoint methods for car aerodynamics”. Journal of Mathematics in Industry, Vol. 4, No. 6, 2014.

Pacull M. “Conception avant-projet des avions de trasnport commerciaux”. Airbus internal document, 1990.

Papadimitriou D. I., Giannakoglou K. C. “A continuous adjoint method with objective function derivatives based on boundary integrals for inviscid and viscous flows”. Journal of Computers & Fluids, Vol. 36, No. 2, pp. 325-341, 2007.

Paparone L., Tognaccini R. “A Method for Drag Decomposition from CFD Calculations”. ICAS Congress, 2002.

Paparone L., Tognaccini R. “Computational Fluid Dynamics-Based Drag Prediction and Decomposition”. AIAA Journal, Vol. 41, No. 9, 2003.

Peery D.J. “Aircraft structures”. McGraw Hill Book Company Edition, 1950.

Peigin S., Epstein B. “Computational Fluid Dynamic Driven Optimization of Blended Wing Body Aircraft”. AIAA journal, Vol. 44, No. 11, pp. 2736-2745, 2006.

Peigin S., Epstein B. “Efficient Approach for Multipoint Aerodynamic Wing Design of Business Jet Aircraft”. AIAA journal, Vol. 45, No. 11, pp. 2612-2621, 2007.

Peter J. E. V., Dwight R. P. “Numerical Sensitivity Analysis for Aerodynamic Optimization: A Survey of Approaches”. Computers and Fluids, Vol. 39, pp.373-391, 2010.

Piperni P., DeBlois A., Henderson R. “Development of a Multilevel Multidisciplinary Optimization Capability for an Industrial Environment”, AIAA Journal, Vol. 51, No. 10, 2013.

Piperni P., Abdo M., Kafyeke F. “Preliminary Aerostructural Optimization of a Large Business Jet”. Journal of Aircraft, Vol. 44, No. 5, 2007.

Pironneau O. “On Optimum Profiles in Stokes Flow”. Journal of Fluid Mechanics, Vol. 59, No. 1, pp. 117-128, 1973.

Pironneau O. “On Optimum Design in Fluid Mechanics”. Journal of Fluid Mechanics, Vol. 64, pp. 97-110, 1974.

Pironneau O. “Optimal Shape Design for Elliptic Systems”. Springer-Verlag, 1984.

Poon N. M. K., Martins J. R. R. A. “Adaptive Constraint Aggregation for Structural Optimization Using Adjoint Sensitivities”. Canadian Aeronautics and Space Institute Annual General Meeting, Aircraft Design & Development Symposium, 2005.

Prandtl L. “Über Flüssigkeitsbewegung bei sehr kleiner Reibung, Verh”. III Int. Math. Kong., Heidelberg, Teubner, Leipzig, pp. 484-491. Translation available as: Motion of fluids with very little viscosity, NACA-TM-452, 1928.

Prandtl L. “Uber tragflugel des kleinsten induzierten widerstandes. Zeitschrift für Flugtechnik und motorluftshiffahrt”. 1993.

Prandtl L., Tietjens O.G. “Applied Hydro and Aerodynamics”. Dover Edition, 1957.

Price K., Storn N. “Differential Evolution”. Dr. Dobb’s Journal, pp. 18-24, 1997.

Prigent S. “Innovative and integrated approach for environmentally efficient aircraft design and operations”. PhD thesis, Institut Supérieur de l’Aéronautique et de l’Espace, 2015.

Prigent S., Maréchal P., Rondepierre A., Druot T., Belleville M. “A Robust Methodology for Preliminary Aircraft Design”. Journal of Engineering Optimization, Vol. 48, Issue 5, pp. 883-899, 2015.

Reuther J. J., Jameson A. “Supersonic wing and wing-body shape optimization using an adjoint formulation”. IMECE95, The Forum on CFD for Design and Optimization, 1995.

Reuther J. J., Jameson A., Alonso J. J., Rimlinger M. J., Saunders D. “Constrained Multipoint Aerodynamic Shape Optimization Using an Adjoint Formulation and Parallel Computers”. Part 1, Journal of Aircraft, Vol. 36, No. 1, pp. 51-60, 1999.

Reuther J. J., Jameson A., Farmer J., Martinelli L., Saunders D. “Aerodynamic shape optimization of complex aircraft configurations via an adjoint formulation”. AIAA paper 96-0094, 1996.

Reuther J. J., Jameson A., Alonso J. J., Rimlinger M. J., Saunders D. “Constrained Multipoint Aerodynamic Shape Optimization Using an Adjoint Formulation and Parallel Computers”. Part 2, Journal of Aircraft, Vol. 36, No. 2, pp. 61-74, 1999.

Rechenberg I. “Evolutionsstrategie – Optimierung technischer Systeme nach Prinzipien der biologischen Evolution”. Fommann-Holzboog, 1973.

Rizzi A. “Spurious Entropy Production and very Accurate Solutions to the Euler Equations”. The Aeronautical Journal, pp. 59-71, 1985.

Rizzi A., Opplstrup J., Zhang M., Tomac M. “Coupling Parametric Aircraft Lofting to CFD & CSM Grid Generation for Conceptual Design”. 49th AIAA Aerospace Science Meeting including the New Horizons Forum and Aerospace Exposition, 2011.

Roe P. L. “Approximate Riemann Solvers, Parameters Vectors and Difference Schemes”. Journal of Computation in Physics, Vol. 43, pp. 292–306, 1981.

Sasaki D., Obayashi S., Nakahashi K. “Navier-Stokes optimization of supersonic wings with four design objectives using evolutionary algorithm”. AIAA paper 2001-2531, 2001.

Shubin G. B., Frank P. D. “A comparison of the implicit gradient approach and the variational approach to aerodynamic design optimization”. Boeing Computer Services Report, AMS-TR-163, 1991.

Sibilli T., Savill M. “Computational Fluid Dynamics Drag Prediction and Decomposition for Propulsive System Integration”. ASME Turbo Expo, 2011.

Slooff J.W. “Computational Drag Analysis and Minimization: Mission Impossible?”. AGARD-R-723, Aircraft Drag Prediction and Reduction, 1985.

Slooff J.W. “Foreword and Conclusion to Technical Status Review on Drag Prediction and Analysis from Computational Fluid Dynamics: State of Art”. AGARD AR-256, 1989.

Sobieszczanski-Sobieski J., Haftka R. T. “Multidisciplinary aerospace design optimization: survey of recent developments”. Structural and Multidisciplinary Optimization, Vol. 14, No. 1, pp. 1-23, 1997.

Squire S., Trapp G. “Using Complex Variable to Estimate the Derivatives of Real Function”. SIAM, Vol. 40, No. 1, pp.100-102, 1998.

Steger J.L., Baldwin B.S. “Shock Waves and Drag in the Numerical Calculation of Isontropic Transonic Flow”. NASA TN D-6997, 1972.

Striz A., Kennedy B., Siddique Z., Neeman H. “A roadmap for moderate fidelity conceptual design with multilevel analysis and MDO”. Collection of Technical Papers – AIAA.SME/ASCE/AH/ASC Structure, Structure Dynamics and Materials Conference, Vol. 1, pp. 222-232, 2006.

Szmelter J. “Multipoint Aerodynamic Wing Optimization in Viscous Flow”. Journal of Aircraft, Vol. 38, No. 5, pp. 860-867, 2001.

Ta’asan S., Kuruvila G., Salas M. D. “Aerodynamic design and optimization in one shot”. AIAA paper 92-0025, 1992.

Tani I. “History of boundary layer theory”. Annual Review Fluid Mech., Vol. 9, pp. 87-111, 1977.

Toal D. J. J., Keane A. J. “Efficient Multipoint Aerodynamic Design Optimization Via Cokriging”. Jounal of Aircraft, Vol. 48, No. 5, pp. 1685-1695, 2011.

Tognaccini R. “Method for Drag Decomposition, Thrust-Drag Bookkeeping from CFD”. Calculation, VKI Lecture Series, CFD-based Aircraft Drag Prediction and Reduction, 2003.

Tognaccini R. “Drag Computation and Breakdown in Power-on Conditions”. Journal of Aircraft, Vol. 42, No.1, 2005.

Tomac M., Rizzi A., Oppelstrup J. “From Geometry to CFD Grids – An Automated Approach for Conceptual Design”. AIAA Atmospheric Glight Mechanics Conference, 2010.

Torenbeek E. “Synthesis of subsonic airplane design”. Delft University Press, Kluwer Academic Publisher, 1982.

Toubin H., Bailly D. “Development and Application of a New Unsteady Far-Field Drag Decomposition Method”. AIAA Journal, Vol. 53, No. 11, pp. 3414-3429, 2015.

Ueno M., Yamamoto K., Tanaka K., Murayama M., Tognaccini R. “Far-Field Drag Analysis of NASA Comon Research Model Simulations by JAXA”. 20th AIAA Computational Fluid Dynamics Conference, 2011.

Van Albada G. D., Van Leer B., Roberts W. “A Comparative Study of Computational Methods in Cosmic Gas Dynamics”. Astronomy and Astrophysics, Vol. 108, pp. 76–84, 1982.

Van Dam C.P. “Recent experience with different methods of drag prediction”. Progress in Aerospace Science, Vol. 35, Issue 8, pp. 751-798, 1999.

Vanderplaats G. N. “A robust Feasible Direction algorithm for design synthesis”. AIAA paper, 24th Structures, Structural Dynamics and Materials Conference, 1983.

Vanderplaats G. N. “Numerical Optimization Techniques for Engineering Design”. McGraw-Hill, New York, 1984.

Van der Vooren J., Slooff J.W. “CFD-based Drag Prediction: State-of-Art, Theory, Prospects”. Lecture Notes of AIAA Professional Studies Series, NLR TP 90247, 1990.

Van Laarhoven P. J. M, Aarts E. H. L. “Simulated Annealing: Theory an applications”. Kluwer Accademic Publishers, 1987.

Vassberg J.C., Jameson A. “In pursuit of Grid Convergence for Two-Dimensional Euler Solution”. Journal of Aircraft, Vol. 47, No. 4, pp. 1152-1166, 2010.

Vassberg J.C., Jameson A. “Theoretical Background for Aerodynamic Shape Optimization”. VKI lecture series on Introduction to Optimization and Multidisciplinary Design, 2014.

Versteeg H., Malalasekera W. “An Introduction to Computational Fluid Dynamics: The Finite Volume Method”. Prentice Hall Edition, 2007.

Verstraete T. “Introduction to Optimization and Multidisciplinary Design”. VKI lecture series on Introduction to Optimization and Multidisciplinary Design, 2014.

Viti A., Druot T., Dumont A. “Aero-structural approach coupled with direct operative cost optimization for new aircraft concept in preliminary design”. AIAA/ISSMO-MOA, 2016.

Viti A., Dumont A., Carrier G. “Innovative Arodynamic Design Procedure for a Forward-Swept Wing in Preliminary Design”. 50th 3AF International Conference on Applied Aerodynamics, 2015.

Wakayama S., Kroo I. “The challenge and promise of blended-wing-body optimization”. AIAA Papers No. 98-4736.

Yamazaki W. “Aerodynamic Design Optimization and Drag Visualization of Aircraft using a Drag Breakdown Approach”. Journal of the Visualization Society of Japan, Vol.35, No. 138, pp. 8-13, 2015.

Yamazaki W., Matsushima K., Nakahashi K. “Unstructured Drag Prediction Based on Drag Decomposition”. European Conference on Computational Fluid Dynamics, ECCOMAS CFD, 2006.

Yamazaki W., Matsushima K., Nakahashi K. “Aerodynamic Design Optimization Using the Drag-Decomposition Method”. AIAA Journal, Vol. 46, No. 5, pp. 1096-1106, 2008.

Zang T. A., Green L. L. “Multidisciplinary Design Optimization Techniques: Implications and Opportunities for Fluid Dynamics Research”. AIAA Paper, No. 99-3798, 1999.

Zhang M. “Application and Development of the CAESIOM-SUMO-EDGE Suite for Rapid AeroData Assessment of Aircraft Flying Qualities”. PhD Thesis, KTH Stockholm, 2011.

Zhang M., Rizzi A., Raymen D. “Enhancement of CEASIOM with Rapid-Mesh Tool for Aircraft Conceptual Design”. Aerotecnica Missili&Spazio, The journal of Aerospace Science, Technology and Systems, Vol. 91, No. 3/4, 2012.

Zhang M., Rizzi A., Raymen D. “Using CAESIOM-SUMO Rapid-Meshing in Computational Study of Asymmetric Aircraft Design”. EWADE European Workshop on Aircraft Design Education, 2011.

Zingg D. W., Nemec M., Pulliam T. H. “A Comparative Evaluation of Genetic and Gradient-Based Algorithms Applied to Aerodynamic Optimization”. European Journal of Computational Mechanics, Vol. 17, No. 1-2, pp. 103-126, 2008.

Zoutendijk G. “Method of feasible direction: a study in linear and nonlinear programming”. Elsevier Pub. Co., 1960.

Zymaris A. S., Papadimitriou D. I., Giannakoglou K. C., Othmer C. “Continuous Adjoint Approach to the Spalart-Allmaras turbulence model for incompressible flows”. Journal of Computers & Fluids, Vol. 38, No. 8, pp. 1528-1538, 2009.